

The Balmer lines emission of fast hydrogen atoms at the plasma-solid interface in a low density plasma: challenges and applications

Sven Oliver Dickheuer

Energie & Umwelt / Energy & Environment

Band / Volume 489

ISBN 978-3-95806-458-4

Forschungszentrum Jülich GmbH
Institut für Energie- und Klimaforschung
Plasmaphysik (IEK-4)

The Balmer lines emission of fast hydrogen atoms at the plasma-solid interface in a low density plasma: challenges and applications

Sven Oliver Dickheuer

Schriften des Forschungszentrums Jülich
Reihe Energie & Umwelt / Energy & Environment

Band / Volume 489

ISSN 1866-1793

ISBN 978-3-95806-458-4

Bibliografische Information der Deutschen Nationalbibliothek.
Die Deutsche Nationalbibliothek verzeichnet diese Publikation in der
Deutschen Nationalbibliografie; detaillierte Bibliografische Daten
sind im Internet über <http://dnb.d-nb.de> abrufbar.

Herausgeber und Vertrieb: Forschungszentrum Jülich GmbH
Zentralbibliothek, Verlag
52425 Jülich
Tel.: +49 2461 61-5368
Fax: +49 2461 61-6103
zb-publikation@fz-juelich.de
www.fz-juelich.de/zb

Umschlaggestaltung: Grafische Medien, Forschungszentrum Jülich GmbH

Druck: Grafische Medien, Forschungszentrum Jülich GmbH

Copyright: Forschungszentrum Jülich 2020

Schriften des Forschungszentrums Jülich
Reihe Energie & Umwelt / Energy & Environment, Band / Volume 489

D 294 (Diss. Bochum, Univ., 2019)

ISSN 1866-1793
ISBN 978-3-95806-458-4

Vollständig frei verfügbar über das Publikationsportal des Forschungszentrums Jülich (JuSER)
unter www.fz-juelich.de/zb/openaccess.



This is an Open Access publication distributed under the terms of the [Creative Commons Attribution License 4.0](https://creativecommons.org/licenses/by/4.0/), which permits unrestricted use, distribution, and reproduction in any medium, provided the original work is properly cited.

CONTENTS

Kurzfassung/Abstract

1	Introduction	1
2	Theoretical Aspects of Fast Atoms Emission and their Detection	4
2.1	Langmuir-Debye-Sheath as a Source of Fast Atoms	4
2.2	Distribution Functions of the Backscattered Atoms	5
2.3	The Doppler Effect	8
2.4	Line Radiation	10
2.5	Fine Structure of Hydrogen	11
2.6	Zeeman Effect	13
2.7	Broadening Mechanisms	16
2.7.1	Natural Broadening	16
2.7.2	Doppler Broadening	16
2.7.3	Stark Broadening	17
3	Experimental Setup	18
3.1	The PSI-2 Device	18
3.2	Manipulator at PSI-2	20
3.2.1	Radial Manipulator	20
3.2.2	Axial Manipulator	21
3.3	Diagnostics at PSI-2	22
3.3.1	High Resolution Echelle Spectrometer (HRES)	22
3.3.2	Calibration of the HRES and Analysis of the Spectrum	23
3.3.3	Passive Emission of Balmer Lines in PSI-2	24
4	Experimental Results of the Emission of Fast Atoms	27
4.1	Characterization of the H-Ar Plasma in PSI-2	27
4.2	Doppler-Shifted Emission of Fast Atoms as a Function of the Incident Ion Energy	29
4.3	Doppler-Shifted Emission of Fast Atoms as a Function of the Target Material	33
4.4	Development of the Doppler-Shifted Reflectance Measurements (DSRM) Diagnostic	36

4.4.1	Calculation of Reflectance	39
4.5	Determination of the Spectral Reflectance for Various Mirror Materials	43
4.6	Time Stability and Voltage Dependence of the Reflectance	44
4.7	Spectral Reflectance Measurements at H_{β}	47
4.8	Measurement of the Plasma Profile using the Emission of Fast Atoms	49
4.9	Polarization of Light by Reflectance at the Mirror Surface	50
4.10	Temperature Dependence of the Spectral Reflectance	54
4.11	Modeling of the Doppler-shifted Emission Profiles	60
4.12	Gas and Pressure Scan of Different Mixed Plasmas with Ar, Kr and Ne	64
5	Measurements of metastable Ar in PSI-2	69
5.1	Theoretical Aspects of Tunable Diode Laser Absorption Spectroscopy (TDLAS)	69
5.2	TDLAS Setup at PSI-2	71
5.3	Impact of the Magnetic Field on the Absorption Profile of the Metastable Density	75
5.4	Determination of the Metastable Density	78
5.5	Absorption Measurements in a H-Ar mixed Plasma	84
6	Conclusion and Outlook	88
	List of Figures	94
	List of Tables	103
	Bibliography	104
	List of Publications	I
	Acknowledgement	III

KURZFASSUNG

Die starke Verbreiterung von Lyman- und Balmerlinien in H oder H-Mischplasmen ist ein weitverbreitetes und vielfach untersuchtes Phänomen in vielen verschiedenen Plasmen, von stellaren bis hin zu Laborplasmen. In Laborplasmen werden sowohl die Quelle der schnellen H Atome vor der Oberfläche als auch der Ursprung der beobachteten Emission kontrovers diskutiert. *A. V. Phelps* schlägt ein "Schicht-Kollisions" Model vor, in dem H^+ , H_2^+ und H_3^+ Ionen in der Schicht beschleunigt und schnelle H Atome durch Ladungstransfer oder Dissoziation mit Gas oder der metallischen Oberfläche erzeugt werden. Es gibt eine Vielzahl von Experimenten, welche versuchen die Verbreiterung der Linien zu erklären. Die Community konnte sich bisher jedoch nur darauf einigen, dass die Verbreiterung auf den Doppler Effekt zurückzuführen ist. In diesem Bereich werden Experimente normalerweise bei hoher Dichte durchgeführt ($p \geq 1$ Pa). Dies macht es jedoch aus den folgenden Gründen sehr kompliziert die dopplerverschobene Emission zu analysieren. Erstens führt die hohe Dichte dazu, dass sowohl beschleunigte Ionen innerhalb der Schicht als auch zurück gestreute schnelle Atome emittieren. Daraus folgt, dass das gemessene Signal eine Superposition beider Effekte ist. Zweitens kommt es durch die Emission der Ionen innerhalb der Schicht zu einer Stark-Verbreiterung der emittierten Linien, was die Analyse der gemessenen Spektren noch schwieriger macht.

In dieser Arbeit werden zwei Hauptprobleme der dopplerverschobenen Emission von schnellen Atomen untersucht. Zum einen, die Quelle der Emission der schnellen Atome und ihre Eigenschaften und zum anderen die Anwendung der beobachteten blau- und rotverschobenen Emission in der Physik von Niedrigdruck- und Niedrigtemperaturplasmen. Die hier vorgestellten Experimente wurden in der PSI-2 Anlage in einem Niedrigdruckplasma ($p < 0.05$ Pa) durchgeführt. Die Messungen werden bei niedriger Dichte durchgeführt, um Emission in der Schicht im Allgemeinen und Emission von beschleunigten Ionen innerhalb der Schicht im Speziellen zu vermeiden. In einem reinem Niedrigdruck-Wasserstoffplasma wird im Gegensatz zu Experimenten in Hochdruckplasmen nahezu keine dopplerverschobene Emission beobachtet. Die Linienverbreiterung beginnt sich auszubilden, wenn Ar in das Plasma gemischt wird. Durch Variation des Oberflächenmaterials und der an der Oberfläche angelegten negativen Spannung konnten die Experimente beweisen, dass die Quelle der dopplerverschobenen Emission nur zurückgestreute oder reflektierte Atome sind. Diese Atome gehen aus der Ionen-Oberflächen Wechselwirkung hervor, was Emission durch Ladungsaustauschwechselwirkung in der Schicht ausschließt. Des Weiteren

konnten weitere Messungen in dieser Arbeit beweisen, dass die rotverschobene Emission, erzeugt durch die gleichen Atome, nur durch Licht- oder Photonreflektion an der Metalloberfläche hervorgerufen wird. Letztere Beobachtung hat zu der Entwicklung einer neuen **Doppler-Shifted Reflectance Measurement (DSRM)** Diagnostik geführt, mit welcher die spektrale Reflektion von Metalloberflächen während der Plasmaexposition *in situ* gemessen werden kann. Aber nicht nur die spektrale Reflektion, auch die Polarisation der Emission durch Lichtreflektion und die Verschlechterung der optischen Eigenschaften der Oberfläche werden das erste Mal während des Plasmabetriebs gemessen. Darüber hinaus werden erste Ergebnisse über die Reflektivität von Rh Spiegeln bei hohen Temperaturen präsentiert, welche helfen können eine **Charge Exchange Recombination Spectroscopy (CXRS)** Diagnostik an ITER aufzubauen. Die Untersuchung der Emission von schnellen Atomen in anderen Edelgasen wie He, Ne, Kr und Xe haben im Gegensatz zu bisherigen Annahmen und experimentell bestimmten Wechselwirkungsquerschnitten, eine viel schwächere Emission im Vergleich zu Ar gezeigt. Es wird bewiesen, dass die Anregungsquelle von H bei der Wechselwirkung mit Ar bei den genutzten Bedingungen auf nur zwei mögliche atomare Prozesse eingegrenzt werden kann: Grundzustandanregung oder Anregung über metastabile Zustände von Ar. Letzteres wird mit einer **Tunable Diode Laser Absorption Spectroscopy (TDLAS)** Diagnostik gemessen, welche an der PSI-2 Anlage während dieser Arbeit installiert und getestet wurde. Die experimentellen Ergebnisse, welche während dieser Arbeit erlangt worden sind, wie z.B. die absolute Konzentration und die räumliche Verteilung der metastabilen Atome oder die Gastemperatur entlang der Plasmasäule, unterstützen die These der H Anregung durch metastabiles Ar. Trotzdem sind noch weitere theoretische und experimentelle Untersuchungen notwendig, um eine Lösung für dieses Problem zu finden. Anwendungen der DSRM Diagnostik sind von der Quelle der Emission in Edelgasen jedoch nur geringfügig abhängig.

ABSTRACT

The wide broadening of Lyman and Balmer lines in H or H mixed plasmas is a widely observed and studied phenomena in many kinds of different plasmas, ranging from stellar to laboratory plasmas. The source of the fast H atoms in front of the surface as well as the origin of the observed emission in laboratory plasmas is under controversial discussion. *A. V. Phelps* proposes a "sheath-collision" model in which H^+ , H_2^+ and H_3^+ ions are accelerated in the sheath and create fast H atoms by charge transfer or dissociation interaction with gas or the metallic surface. There are a number of experiments trying to explain the broadening of the lines, but the community could only agree on the fact that the broadening is caused by the Doppler effect. Usually experiments in this field are performed in high pressure plasmas ($p \geq 1$ Pa), but this makes it very difficult to analyze the Doppler-shifted emission due to the following reasons. On the one hand, the high pressure leads to emission of accelerated ions and backscattered atoms which makes the detected signal a superposition of both effects. On the other hand, the emission of ions inside the Debye sheath leads to a Stark broadening of the emitted lines and makes the analysis of the emission spectra complicated.

In this thesis the two main problems of the Doppler-shifted emission of the fast atoms are investigated. First, the source of emission of the fast atoms and its properties and second, the application of the observed blue and red-shifted emission in physics of low density and low temperature plasmas. The experiments are performed in a low density plasma ($p < 0.05$ Pa) at the PSI-2 device. The low density is used to avoid emission by ions accelerated in the sheath and emission inside the sheath in general. In a low density pure H plasma practically no Doppler-shifted emission is observed in comparison to the high pressure experiments. The line broadening begins to arise when Ar is mixed into the plasma. By varying the surface material and the applied negative potential to the surface, the experiments have proven that the source of the Doppler-shifted emission are only backscattered or reflected atoms created as a result of ion-surface interaction which exclude emission caused by charge-exchange in the sheath. Further studies presented in this thesis prove that the red-shifted emission generated by the same atoms is only caused by light or photon reflection at the metallic surface. The latter observation stimulated a development of a new **Doppler-Shifted Reflectance Measurement (DSRM)** diagnostic which can measure the spectral reflectance of the metallic surface *in situ* during the plasma exposition. But not only the spectral reflectance, also the polarization by light reflection and

the degradation of the optical properties of the surface are measured for the first time during plasma exposition. Furthermore, the first results on the reflectance of a Rh mirror at high temperatures are presented, which can help to built-up a **C**harge **E**xchange **R**ecombination **S**pectroscopy (CXRS) diagnostic at ITER.

The study of emission of fast atoms in other noble gases such as He, Ne, Kr and Xe demonstrated in contrast to the previous assumptions and the experimental cross-sections a much weaker emission in comparison to Ar. It is shown that the excitation source of H by collisions with Ar at the used conditions could be limited to only two possible atomic processes: excitation by the ground state or excitation transfer from the metastable state. The latter is measured using a **T**unable **D**iode **L**aser **A**bsorption **S**pectroscopy (TDLAS) diagnostic installed and tested at the PSI-2 device during this thesis. The experimental results obtained in this thesis, e.g. the absolute concentration, the spatial distribution of the metastable atoms or the gas temperature along the plasma column, support the theory of excitation transfer by metastable Ar, though further theoretical and experimental studies are still required to give an answer on this unsolved problem. Nonetheless further applications of the DSRM diagnostic are weakly affected by the source of the observed emission in noble gases.

CHAPTER 1

INTRODUCTION

Fast hydrogen atoms are present in many kinds of different plasmas like stellar [CTW89] or planetary [AKA95] plasmas, radio frequency induced plasmas [BGC05], glow discharges [Ada03], low temperature hollow cathode plasmas [SMK05] or finally fusion plasmas [Hey96]. An extensive broadening of the Lyman or Balmer line series remains one of the most sensitive and robust techniques to detect them. So for instance, the measurements of the magnetic or electric field, electron density or the fraction of high energetic ions are derived using the spectra of Balmer series.

Special interest represents the observation of fast atoms in the plasma sheath of low temperature laboratory plasma. On the one hand, the emission of fast atoms is used to determine the electric field in the plasma measuring the Stark effect [VKK96; Rei17], but the fast atoms could also provide information on the plasma-surface interaction. In spite of the considerable amount of experimental data, performed mostly in the Grimm-type glow discharges [CKK05; COK09; COK11] at a pressure of 100 Pa and higher, only a general agreement on the source of blue and red-shifted signal exists, namely that the broadening of the emission is caused by the Doppler effect. The controversial discussion on the possible atomic interactions and a model describing the observed emission could be found in the literature [Phe05].

The “sheath-collisional” model of Phelps [Phe05] represents probably the most accurate description of the emission of fast atoms in high density discharges. Here the H^+ , H_2^+ and H_3^+ ions are accelerated in the sheath and produce fast H atoms in charge transfer/dissociation collisions with the background gas [Phe05]. The second source of fast backscattered or reflected atoms is generated at the surface by neutralization of ions or molecular ions. As a result, the observed emission is always a superposition of two kinds of signals generated by fast incident and backscattered or reflected atoms. In the case of observation perpendicular to the cathode the red-shifted component of the Doppler-shift could be explained by charge-exchange interaction of ions accelerated in the sheath towards the surface [Phe09; Phe11]. In contrast to that, the blue-shifted signal is explained by the emission of the backscattered ones. If the backscattered atoms emit inside the Debye sheath, the situation becomes even more complex, because for these atoms Stark splitting needs to be taken into account as well. Nevertheless, the number of observations could still not be explained in the frame of this theory. In contrast to the expectation of the “beam-like” distribution of “incident” atoms accelerated in the sheath the diffusive angular distribution or even

broader one provided the much better agreement with the modeling of the red-shifted signal. Until now the reason of such behavior could not be understood and thus more accurate kinetics models are required. In fact the fast “incident” atoms frequently demonstrate the broader angular distribution compared to the fast backscattered atoms. On the other hand, the measured position of the maxima of emission of Balmer lines in front of the surface or the spatial extension of emission could also not be explained for the high density glow discharges. It seems that the measurements of electric field in the sheath remains the only application of such observations even after many decades of research.

In contrast to this, the accurate measurements of the emission in low density gas discharges are quite seldom [BGC05]. According to the sheath-collisional model only a strong source from the backscattered atoms is predicted: “*Evidence for this behavior is that the predicted, but unmeasured, axial H_α spectral profile is highly asymmetric for cathode surfaces with a high efficiency of fast atom reflection*” [Phe11]. Such behavior, however, was not observed in a few spectra measured in rf plasma ($p = 10$ Pa) [BGC05]. Instead, the additional contribution of the light reflection at the surface to the red-shifted signal was suggested here [BGC05]. In the first studies with different cathode material this option was also seriously considered in high density gas discharges [AKK04]. In the forthcoming works the contribution of photon reflectance at the surface was considered of little [Ada03] or of no importance [COK11]. As a result, this effect did not play any role in the consequent modeling and reviews.

In gas discharges where the hydrogen is mixed with other noble gases the situation becomes even more unclear. One expects the increase of observed emission and at the same time a rapid transition between the ions and molecular ions. So for instance, according to [Ada03], the amount of Ar on the order of 5 – 10 % added to the H plasma results in dramatic decrease of concentration of hydrogen in favor of H_3^+ molecular ions. It is not clear if such a behavior is of relevance for low density gas discharges as well. Finally, Šišović *et al.* reported that the red-shifted emission can be changed by varying the electric field of the experimental setup [ŠMK05]. All the experiments mentioned above are carried out in high pressure plasmas ($p > 100$ Pa). Obviously, the source of the fast atom emission and especially of the red-shifted component caused by the Doppler broadening seems to be an open and unanswered question since there are different explanations of the observed emission. The need for new experimental data especially in low density plasmas are explained from different views. First of all, by suppressing the emission from incident atoms one has a much better insight into the physics of backscattered atoms. Second, one obtains an enhanced opportunity to test atomic models at the plasma edge neglecting the kinetics of ions and molecular ions. From the experimental point of view the principle distinction between the previous and present study of emission is based on the fact that the plasma discharge in our experiment is ignited independently on the kinetic energy of the ions accelerated in the sheath. One has a unique possibility to study the emission of fast atoms in the same plasma conditions for different kinetic energies of the ions in the sheath. Finally, one studies the emission of fast atoms in the energy range starting from a few eV till hundreds of eV covering the energy range not achievable in Grimm-type discharges.

In this thesis two principle problems are investigated:

- (a) What is the source of the emission of fast atoms and the broadening of the

Balmer lines and specially the origin of the red-shifted component in low density gas discharges?

- (b) Unique applications beside the measurement of the Stark effect based on the analysis of Balmer-lines emission and testing of kinetic and atomic models.

The emission by fast atoms is investigated using optical emission spectroscopy (OES) in the PSI-2 device [KF04; Kre15], which operates in a low pressure regime ($p < 0.1$ Pa). The low density gives rise to several advantages. First, no emission takes place inside the Debye sheath which avoids the Stark splitting of the lines. Second, the emission of incoming ions can be suppressed, thus the source of emission are only backscattered atoms which makes the analysis of the spectrum quite simple. For the measurements a H-Ar mixed plasma is used, since the presence of Ar in the plasma enhances the Doppler-shifted emission [Ada03; ŠMK07]. Beside these two main problems also the excitation process between H and Ar is addressed in this thesis and the difference in emission among other noble gases.

The thesis is structured as follows:

- In Ch. 2 theoretical aspects of the fast atom creation and the detection of these atoms are discussed. The topics are the Debye sheath at the plasma edge and the distribution function of backscattered fast atoms. The hydrogen atom and its radiation is covered as well.
- In Ch. 3 the PSI-2 device and the used target holders to expose the sample to the plasma are presented and details on the used high-resolution spectrometer are given.
- In Ch. 4 the experimental results on the plasma-surface interaction are given and different areas of applications are presented. First, the plasma composition is discussed to achieve a high Doppler-shifted signal, followed by the analysis of the obtained signal. The dependence of the measured signal on different values like the potential of the metallic surface and the material is shown. The time and temperature dependence of the Doppler-shifted signal are investigated as well. In the second part these measurements are used to present a completely new diagnostic, which measures the spectral reflectance of the surface and also polarization effects. Finally, a theoretical model is presented to describe not only the passive Balmer component, but also the Doppler-shifted components simultaneously.
- In Ch. 5 measurements of the TDLAS diagnostics are presented, which demonstrate that in addition to excitation by Ar atoms in the ground state the excited levels of H atoms could be excited by metastable Ar. The radial profile, temperature and density of the metastable Ar are measured and the results are shown in this chapter.
- In Ch. 6 a summary of the results obtained in this thesis and an outlook for further research are given.

CHAPTER 2

THEORETICAL ASPECTS OF FAST ATOMS EMISSION AND THEIR DETECTION

In this chapter theoretical aspects about the creation of fast atoms at metallic surfaces and their detection in the plasma are discussed. Sec. 2.1 focuses on the acceleration of ions in the Debye sheath as a source of fast neutral atoms. The distribution function of the backscattered atoms are discussed in Sec. 2.2 and how the Doppler effect can be used to detect the emission by fast atoms (Sec. 2.3). To understand the emission of the H atom in the plasma the line radiation principles (Sec. 2.4), the fine structure of hydrogen (Sec. 2.5) and the different broadening mechanisms in the plasma (Sec: 2.7) are explained.

2.1 Langmuir-Debye-Sheath as a Source of Fast Atoms

A natural source of fast atoms in a laboratory plasma are accelerated ions in the Debye sheath which are backscattered as fast neutral atoms at a metallic surface. The Debye sheath is established, between the plasma and its bounding surface, which could also be a mirror in the gas discharge and is schematically depicted in Fig. 2.1. Because the electrons are more flexible than the ions they are able to leave the plasma at the edge and produce a negative charge at the surface. Assuming that the electron flux is equal the ion flux $\Gamma_e = \Gamma_i$ and that the metallic surface is not grounded, the so-called floating potential U_{sf} can be calculated to [Sta00]:

$$U_{sf} = -\frac{k_B T_e}{e} \ln \left[\left(\frac{m_i}{2\pi m_e} \right) \left(1 + \frac{T_i}{T_e} \right) \right]^{1/2}, \quad (2.1)$$

where e is the elementary charge, k_B is the Boltzmann constant, T_e is the electron temperature, T_i is the ion temperature, m_e is the electron mass and m_i is the ion mass. The total potential, which accelerates the ions can be calculated to:

$$U_{tot} = U_s - U_p, \quad (2.2)$$

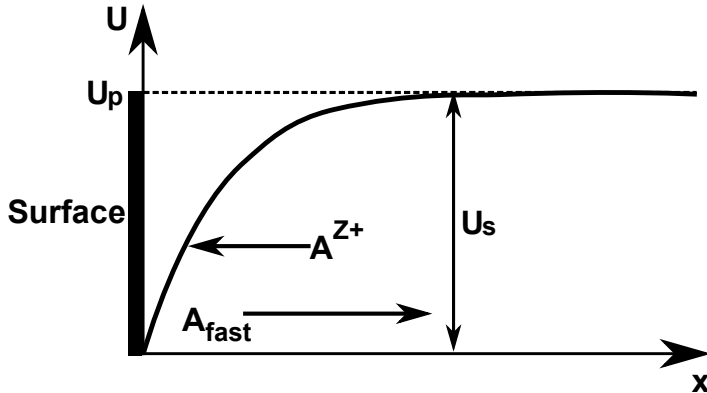


Fig. 2.1: Schematic of the potential drop in the Debye sheath. The plasma potential is denoted with U_p , the surface potential with U_s . In the sheath positive charged ions A^{Z+} are accelerated, neutralized at the surface and backscattered as fast atoms A_{fast} .

where U_p is the plasma potential and U_s is the surface potential. The total potential is negative ($|U_{sf}| > |U_p|$) so that electrons are slowed down and ions are accelerated in the sheath. If no external potential is applied to the surface, the surface potential is equal the floating potential $U_s = U_{sf}$. If a negative potential is applied, the shape of sheath changes and the thickness s can be expressed by the Child-Langmuir equation [Ben09]:

$$s = \frac{\sqrt{2}}{3} \lambda_D \left(\frac{2eU_T}{k_B T_e} \right)^{\frac{3}{4}}, \quad (2.3)$$

where U_T is the applied potential to the surface and $\lambda_D = \sqrt{\epsilon_0 k_B T_e / e^2 n_e}$ is the Debye length, where ϵ_0 is the dielectric constant and n_e is the electron density. The dependency between the sheath thickness and the applied potential to the surface (Eq. 2.3) can be used to change the energy of the ions, which are accelerated in the Debye sheath. Note that if more than one ion species is present in the plasma, the calculation of the sheath becomes much more complicated because each ion species has a different Bohm velocity and a different mobility in the plasma [LL05]. More information about the sheath and the interaction between plasma and surfaces can be found in the following books [Sta00; Hut02; LL05; Kau13].

2.2 Distribution Functions of the Backscattered Atoms

After the ions are accelerated in the direction of the surface they are interacting with the surface. This interaction is very important for different applications, e.g. in fusion plasmas [Doi18; MS79; BGC05] or plasma etching [Fra09]. One kind of interaction is the surface neutralization of ions at the surface. These reflected particles are the source of the fast H atoms in this thesis. In Fig. 2.2 the main channels for the fast atom production are shown. The H^+ , H_2^+ and H_3^+ ions are accelerated in the sheath towards the surface (as explained in the section before). At the surface the ions

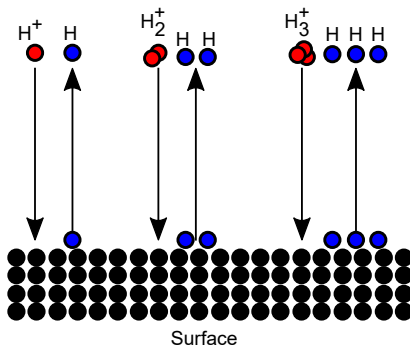


Fig. 2.2: Schematic of the different channels for fast H atom production at the surface with different types of accelerated ions.

are neutralized by Auger or resonance neutralization [Hag54] and scattered back as fast neutral atoms. The H_2^+ and H_3^+ ions are also neutralized by Auger or resonance neutralization at the surface, but afterwards they dissociate into single H atoms. However, the neutralization process is equal for all three kinds of H ions, but the energy of the reflected fast neutrals is different. The kinetic energy of H created out of H^+ can be calculated to $E_{kin,H^+} = eU_{tot} - E_{int}$, where E_{int} is the energy the ion loses because of the surface interaction (this will be discussed later). For H_2^+ it is $E_{kin,H_2^+} \lesssim \frac{1}{2}E_{kin,H^+}$ and $E_{kin,H_3^+} \lesssim \frac{1}{3}E_{kin,H^+}$, respectively. Note, that H^+ or H^- ions are created at the surface as well, but their contribution at energies around 100 eV is small and is therefore neglected [Ver75].

After the backscattering process the fast atoms have a certain angular and energy distribution which is already described in literature [EB85; Xia91; Phe09]. There are also codes available which can calculate the distribution functions for backscattered particles, e.g. by the Monte-Carlo code TRIM [Eck91]. In the TRIM code the following basic assumptions are made: The collisional process of ion and surface is described by a binary collision and the target surface is assumed to be an amorphous structure. For the interatomic potential the "krypton-carbon potential" is used, to be able to compare the data sets with older calculations [EB86]. This backscattering process is a totally inelastic process in the first approximation and can therefore be described as a binary collision between two masses [AFM07]:

$$\frac{E_m}{E_0} = \left[\frac{(M^2 - m^2 \sin^2(\theta_0))^{1/2} - m \cos(\theta_0)}{M + m} \right]^2, \quad (2.4)$$

where E_m is the maximal energy of the backscattered atom, E_0 is the energy of the incident ion, M is the mass of the sample, m is the mass of the incident ion and θ_0 is the angle of observation. For an incident energy of $E_0 = 100$ eV and an observation angle of $\theta_0 = 35^\circ$ the maximum energy E_m for the backscattered atoms will be e.g. $E_{m,W} = 98.03$ eV for $H \rightarrow W$, $E_{m,Fe} = 93.64$ eV for $H \rightarrow Fe$ and $E_{m,C} = 73.63$ eV for $H \rightarrow C$. The TRIM code is used to calculate the distribution function of backscattered particles for different particle and target combinations. Also the particle and energy reflection coefficient for different line-of-sights can be calculated. On the basis of the TRIM code and other codes Xia *et al* have developed

a universal formula to describe the energy distribution of reflected particles [Xia91]:

$$G(E) = A \left[\left(C + D \left(\frac{E}{E_0} \right)^2 \right) \left(B - \frac{E}{E_0} \right) + \exp \left(- \frac{\left(\frac{E}{E_0} - B \right)^2}{2\sigma^2} \right) \right], \quad (2.5)$$

where A, B, C, D and σ are fitting parameters, which are different for each projectile-target system, incident energies and angle of incidence, E is the energy of the backscattered particle and E_0 is the energy of the incoming ion. Solutions for different ion-target system like He-Cu, H-Cu or He-Ni can be found in [Xia91]. The angular distribution function is described by a power of cosine distribution function [EB83; EB85; Phe09]:

$$G(\theta) = \frac{1+b}{2\pi} \cos(\theta)^b, \quad (2.6)$$

where b is a positive value and θ is the azimuthal angle. Theoretical calculation for the angular distribution are available for the whole energy range from eV to keV. Beside the theoretical calculation of the distribution function of backscattered particles also experimental data are available, but in 1979 Eckstein summarizes that up to now "*Experimental data are available for energies above 1 keV only*" [EV79]. Indeed, only a few experiments measuring the energy distribution function of fast atoms for energies below 1 keV, e.g. [HST73] (600 eV) or [BGC05] (50 eV - 400 eV) using energy resolved mass spectroscopy. The difficulty at low energies are the lack of corresponding experimental methods and the fact that the distribution function crucially depends on the topography of the surface [HST73]. Thus, there is a need for experimental data for energies below 200 eV.

Beside ion neutralization at the sheath also other kinds of interaction between plasma and surface are possible, like scattering of neutral atoms [EMV76; EB85; Eck09], ions reflected back as ions [Her03], neutrals backscattered as ions [BEV80] and sputtering process [Tho68; Sig69; Eck02; Eck07]. Scattering of neutrals is not treated in this thesis, because the neutrals are not accelerated in the sheath and thus create no fast atoms in the plasma. Ions backscattered as ions are also neglected because the ions survival probability is usually very low ($< 1\%$ [Her03]). Sputtering process are of importance for the creation of fast atoms, because they can lead to a change of the surface morphology, which can affect the particle reflection coefficient [EV79; HST73]. In comparison to backscattered particles, for sputtered particles a closed analytical formula exists to describe their distribution function. For the energy distribution of sputtered particles the Thompson formula is used [Tho68; Sig69; DM08]:

$$f(E)dE \propto \frac{E}{(E + E_s)^3} dE, \quad (2.7)$$

where E is the energy of the incoming particle and E_s is the surface binding energy. In this thesis the assumption is made that energy and angular distribution function can be separated from each other $G(E, \theta) = G_1(\theta) * G_2(x = E/E_0)$. For the angular distribution a power cosine distribution is used (Eq. 2.6). For the energy distribution a more simpler function (Eq. 2.8) is used to approximate the TRIM data, because at the used experimental setup the ions are always incoming perpendicular to the surface.

$$f(x) = A \frac{1-x}{(2-x_0-x)^\beta}, \quad (2.8)$$

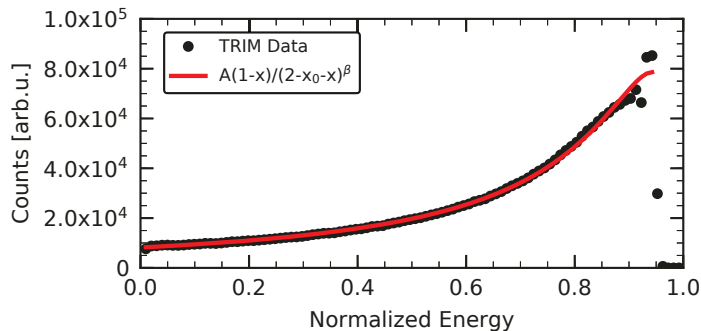


Fig. 2.3: TRIM calculations made by D. Reiter for H on W with an energy of $E_0 = 120$ eV. The data is fitted using the function $f(x) = A(1-x)/((2-x_0-x)^\beta)$, with $A = 1.02 \times 10^4$, $x_0 = 0.91$, $\beta = 2.57$ and $x = E/E_0$.

where $x = E/E_0 \leq 1$ is the normalized energy, β is the width and x_0 the maximal energy of the atoms. The energy $E_0 = E_0(E_i, m, M)$ is the maximal energy of the backscattered atoms with mass m_1 after the binary collision with the target mass m_2 . The energy $E_i \approx eU_i$ is the energy of the accelerated ions under the surface potential U_i . Eq. 2.8 approximates the TRIM calculations made by D. Reiter. In Fig. 2.3 TRIM calculations for H on W are shown. The incident energy of the H atoms was set to $E_i = 120$ eV. The x-axis of Fig. 2.3 is normalized to this incident energy. The TRIM code produces nonphysically values close to the incident energy, where the distribution of the particles drops down to zero. Therefore, these points are excluded for the fit of the TRIM data. For fitting the function Eq. 2.8 is used, but additionally multiplied with an amplitude factor A for matching the height of the distribution function. The result of the fit is $A = 1.02 \times 10^4$, $x_0 = 0.91$ and $\beta = 2.57$. As can be found in Fig. 2.3 the TRIM data is very well described by the used fitting function.

In Fig. 2.4 the total distribution function of the incoming ions and the backscattered atoms are shown schematically. Important to note is that the maximum energy of the incoming ions have to be higher than the maximum energy of the backscattered atoms due to the binary collision with the surface. In this thesis the distribution function of the backscattered atoms is used to model the experimental obtained emission spectra of the fast atoms.

2.3 The Doppler Effect

The Doppler effect was discovered by Christian Doppler in 1842 [Dop42]. The Doppler effect describes how the frequency or the wavelength of an observed wave is changing, if the velocity difference between observer and wave source is unequal to zero $\Delta v \neq 0$. If the observer is at rest and the wave source is moving in the observation direction each wave crest is emitted from a position closer to the observer. As a consequence, the wave is bunched together for the observer and the observed frequency increases and the wavelength decreases (blue-shift). If the wave source is moving away from

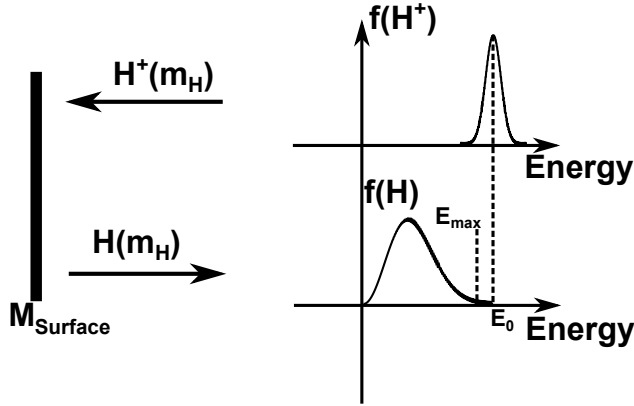


Fig. 2.4: The distribution functions of the incoming ions and the backscattered atoms are shown schematically. Note that both distribution functions differs from each other because of the backscattering process.

the observer, each wave crest is emitted from a position further away from the observer. The observed wave is extended, the measured frequency decreases and the wavelength increases (red-shifted). This can be expressed by Eq. 2.9:

$$\lambda_d = \lambda_0 \left(1 + \frac{\Delta v}{c} \right) \Leftrightarrow \frac{\Delta \lambda}{\lambda_0} = \frac{\Delta v}{c} , \quad (2.9)$$

where λ_d is the detected wavelength, λ_0 is the unshifted wavelength, Δv is the difference in velocity of observer and wave source, c is the speed of light and $\Delta \lambda = \lambda_d - \lambda_0$ is the difference between shifted and unshifted wavelength. Eq. 2.9 shows that the Doppler effect increases with increasing velocity difference Δv .

The Doppler effect can be used to distinguish between the emission of the fast atoms and the background emission, because the kinetic energy of the fast atoms is much higher compared to other particles in the plasma. In Fig. 2.5 a scheme of the expected emission profile of the fast H atoms is shown. The angle of observation θ_0 is measured from the surface normal. If an observation angle $\theta_0 = 90^\circ$ is considered, the line-of-sight (LOS) is parallel to the surface. In this case, the LOS looks symmetric through the hemisphere of scattered particles, therefore a symmetrical emission profile between blue and red-shifted emission is expected. If the LOS is at angles different from 90° an unsymmetrical emission profile is expected. This emission profile needs to be more tilted to smaller wavelength (blue-shifted component). Assuming photon reflection at the surface also a red-shifted emission profile should be observable, where the intensity of the emission profile is defined as:

$$I_r = R \cdot I_b , \quad (2.10)$$

where I_b is the intensity of the blue-shifted emission, R is the spectral reflectance of the target surface and I_r is the intensity of the red-shifted emission. To conclude, in case of a symmetrical emission profile, the integrated emission of the fast atoms is measured in case of an unsymmetrical emission profile one could potentially deduce optical properties of the surface.

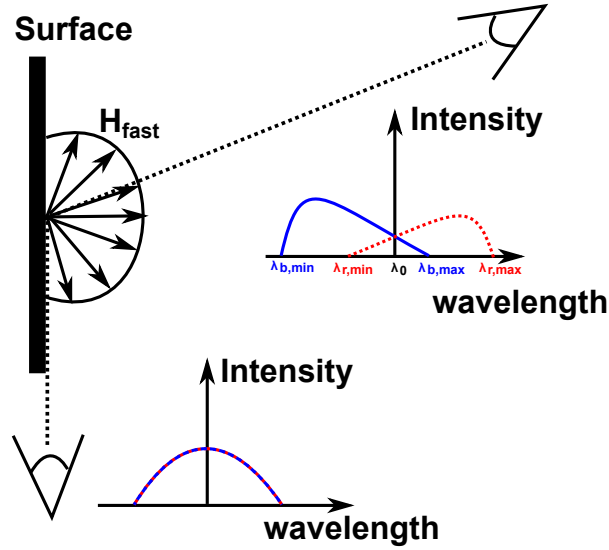


Fig. 2.5: The emission profiles for two exemplary line-of-sights are schematically shown. For a line-of-sight parallel to the surface a symmetrical emission profile is expected. For every other angle the emission profile is expected to be unsymmetrical with regard to the unshifted wavelength.

2.4 Line Radiation

Line radiation is usually detected by optical emission spectroscopy (OES). In general OES is a very powerful tool in plasma physics, because plasma parameters like ion temperature T_i , ion density n_i , electron temperature T_e and electron density n_e can be obtained without disturbing the plasma. To obtain these parameters, the radiation emitted by atoms or ions is detected and analyzed. In the following, only the theoretical aspects of OES relevant for the high-resolution spectroscopy of low density laboratory plasmas will be exemplified. For more detailed information about OES I refer to the following books [Coo66; BS77; Gri97; Kun09].

In this thesis the emission of Balmer lines of H atoms is analyzed which will be

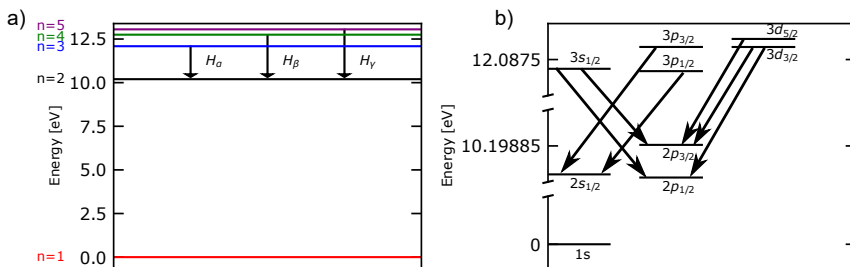


Fig. 2.6: (a) Energy scheme of the hydrogen atoms for the first five quantum numbers $n = 1 \dots 5$. (b) Scheme of the fine splitting structure and the possible transitions of the hydrogen atom at the H_α line.

discussed in more detail in the following. The Balmer lines belong to the line emission and the energy of the photon can be calculated using the energy of the upper or initial state E_{n_i} and the lower or final state E_{n_f} using the following formula:

$$\Delta E_{n_i \rightarrow n_f} = h\nu_{n_i \rightarrow n_f} = E_{n_i} - E_{n_f} , \quad (2.11)$$

where h is the Planck constant and $\nu_{n_i \rightarrow n_f}$ is the frequency of the emitted photon. For H ($Z = 1$) and H-like ions the Schrödinger equation can be solved analytically and the energy difference $\Delta E_{n_i \rightarrow n_f}$ is described by the Rydberg formula 2.12 [BS77]:

$$\Delta E_{n_i \rightarrow n_f} = Z^2 R \left(\frac{1}{n_f^2} - \frac{1}{n_i^2} \right) , \quad (2.12)$$

where Z is the atomic number and R is the Rydberg constant for the specific element. The Rydberg constant is calculated using equation 2.13:

$$R = \frac{R_\infty}{1 + \frac{m_e}{M}} , \quad (2.13)$$

where m_e is the electron mass, M is the nuclear mass of the specific element and R_∞ is the Rydberg constant for infinity nuclear mass, with $R_\infty = 10\,973\,731.57 \text{ m}^{-1}$. One special transition series of the H atom is the so called Balmer series named, after Johann Jacob Balmer, who has described in 1885 a mathematical expression to calculate the wavelength of different hydrogen lines in a spectrum [Bal85]. The Balmer series includes transitions with $n_i > 2$ to $n_f = 2$, where n is the principal quantum number. The H_α , H_β and H_γ were routinely measured in PSI-2 but due to the efficiency of the optical system the majority of the results are presented for the H_α line.

2.5 Fine Structure of Hydrogen

Solving the Schrödinger equation of the hydrogen atom for the radial and spherical coordinates of the wave function one can define the principal quantum number n , the azimuthal quantum number l and the magnetic quantum number m . Using these quantum numbers, the observation of the Balmer series can be explained (see Sec. 2.4). By using a spectrometer with a high resolution by the order of a few pm or less one observe that the spectral line of the transition from $n = 3$ to $n = 2$ is not a single line, but consists at least of seven lines. This substructure of the spectral line is called the fine structure and three corrections need to be made to the standard model [Dem10]:

1. A relativistic increase of the electron mass caused by its movement in the coulomb field which leads to a change of the kinetic energy of the electron.
2. A smearing of the electron charge over the volume $\lambda_c^3 = (\hbar/m_e c)^3$, with the Compton wavelength λ_c which leads to a change of the potential energy of the electron.
3. Interaction between the angular momentum and the spin of the electron (ls-coupling) which leads to a separation of the energy levels.

To calculate the relativistic mass increase the energy of the electron

$$E = \frac{p^2}{2m_e} + E_{pot} \quad (2.14)$$

needs to be exchanged with the relativistic term of the kinetic energy

$$E = c\sqrt{m_0^2c^2 + p^2} - m_0c^2 + E_{pot} . \quad (2.15)$$

The energy correction term can then be calculated to

$$E_{n,l} = -R_y \frac{Z^2}{n^2} \left[1 - \frac{\alpha^2 Z^2}{n^2} \left(\frac{3}{4} - \frac{n}{l + 1/2} \right) \right] , \quad (2.16)$$

with the fine structure constant $\alpha = \frac{1}{4\pi\epsilon_0} \frac{e^2}{\hbar c}$ [Dem10]. The ratio of the relativistic energy correction δE_r and the standard energy E_n scales with $\Delta E_r/E_n \approx \frac{\alpha^2}{n^2}$ which makes it a very small correction to the energy scheme of the H atom and becomes largest for the ground state ($n = 1$).

The second correction is caused by the uncertainty principle that the position of the electron can only be determined up to the Compton wavelength $\lambda_c^3 = (\hbar/m_e c)^3$. The calculation leads to the *Darwin Term* ΔE_D [Dem10]:

$$\Delta E_D = \frac{Z e^2 \hbar^2}{\epsilon_0 m_e^2 c^2} |\Psi(0)|^2 = 4Z^2 m_e c^2 \alpha^4 , \quad (2.17)$$

where $\Psi(0)$ is the wave function of the electron at the origin $r = 0$. Because only the s - wave function is not zero in the origin, the 1s - wave function is put into Eq. 2.17. Calculating again the ratio of the energy correction ΔE_D and unchanged energy E_n one gets $\Delta E_D/E_n = 8Z^2 n^2 \alpha^2$, which is $\approx \alpha^2$ for ($Z = 1, n = 1$).

The ls-coupling cannot be explained by the simple Schrödinger theory, because no other interaction than the coulomb interaction between nucleus and electron is taken into account. Instead, the fine structure can be understood as a Zeeman splitting due to the interaction of the electron spin with the magnetic field created by the movement of the electron on its orbit [Dem10]. Looking at the energy diagram in Fig. 2.6 (b) one can see that the energy levels with $l \geq 1$ are splitting into two energy levels with an energy difference in the range of μeV . Because this difference is so small the substructure is called fine structure. The different energy levels can be calculated using equation 2.18:

$$\begin{aligned} E_{n,m,l} &= E_n - \boldsymbol{\mu}_s \cdot \mathbf{B}_l \\ &= E_n + \frac{\mu_0 Z e^2}{8\pi m_e^2 r^3} (\mathbf{s} \cdot \mathbf{l}) , \end{aligned} \quad (2.18)$$

where $\boldsymbol{\mu}_s$ is the magnetic moment of the spin, \mathbf{B}_l is the magnetic field due to the movement of the electron, μ_0 is the vacuum permeability, Z is the atomic number, m_e is the electron mass, \mathbf{s} is the vector of the spin and \mathbf{l} is the vector of the electron momentum. The total momentum \mathbf{j} can be defined as:

$$\mathbf{j} = \mathbf{l} + \mathbf{s} \text{ with } |\mathbf{j}| = \sqrt{j(j+1)}\hbar \quad (2.19)$$

Using the total angular momentum the scalar product ($\mathbf{s} \cdot \mathbf{l}$) can be calculated to:

$$\begin{aligned} \mathbf{s} \cdot \mathbf{l} &= \frac{1}{2}[\mathbf{j}^2 - \mathbf{l}^2 - \mathbf{s}^2] \\ &= \frac{1}{2}\hbar^2[j(j+1) - l(l+1) - s(s+1)]. \end{aligned} \quad (2.20)$$

With Eq. 2.20 the formula for the energy splitting can be expressed with the following equation:

$$E_{n,l,s,j} = E_n + \frac{a}{2}[j(j+1) - l(l+1) - s(s+1)], \quad (2.21)$$

with the spin-orbit coupling constant

$$a = \frac{\mu_0 Z e^2 \hbar^2}{8\pi m_e^2 r^3}. \quad (2.22)$$

More information about the fine structure can be found in [Dem10] or [BS77].

Beside the fine structure also the Lamb shift needs to be taken into account if the resolution of the spectrometer is high enough. Accurate measurements of the fine-structure of H are made by Willis Lamb and Robert Retherford in 1947 [LR47] using microwave measurements. For the two levels $2S_{1/2}$ and $2P_{1/2}$ an energy difference of ≈ 1000 MHz was found, in disagreement with the Dirac theory. This shift is called Lamb shift and modern high precision measurements determine the difference between $2S_{1/2}$ and $2P_{1/2}$ in H to ≈ 1057.8450 MHz [Bea00] and for the ground state $1S_{1/2}$ to ≈ 8172.86 MHz [Wei94; Bea00]. The Lamb shift is the result of the interaction between vacuum fluctuations and the electron of the hydrogen atom. This interaction results in the emission and absorption of virtual photons which leads to a small shift δr of the energy terms by

$$\langle E_{pot} \rangle = -\frac{Ze^2}{4\pi\epsilon_0} \left\langle \frac{1}{r + \delta r} \right\rangle. \quad (2.23)$$

The lamb shift can also be calculated theoretically as can be found in [BS77]. The lamb shift for s-states for example can be calculated using Eq. 2.24 :

$$\Delta E(n, 0) = \frac{8Z^4 \alpha^3}{n^3 3\pi} R_y \left[2 \log \left(\frac{1}{Z\alpha} \right) + \log \left(\frac{Z^2 R_y}{K_0(n, 0)} \right) + \frac{19}{30} \right] \quad (2.24)$$

where Z is the atomic number, n is the principal quantum number, R_y is the Rydberg energy and $\log \left(\frac{Z^2 R_y}{K_0(n, 0)} \right)$ is the Bethe logarithm and the value $K_0(n, 0)$ can be calculated numerically. The Lamb shift scales with $Z^4 n^{-3}$ and thus increases with higher atomic number and smaller principal quantum number n . Compared to the other corrections made, the Lamb shift scales with α^3 , which is a factor of $\approx 10^{-3}$ smaller than the other corrections. For the $2P_{1/2}$ state of hydrogen the Lamb shift is 4.37×10^{-6} eV, but the fine splitting of the state is 1.81×10^{-4} eV which makes the Lamb shift negligible compared to the fine splitting.

2.6 Zeeman Effect

In the PSI-2 device a magnetic field is used to confine the plasma. All the radiation models mentioned above do not include an external magnetic field. If an atom is

brought into a magnetic field, the Zeeman effect is observed. The Zeeman effect was first observed in 1897 by Pieter Zeeman [Zee97a; Zee97b; Zee97c].

If a H atom is brought into a magnetic field, two kinds of Zeeman effects can be observed - the normal and the anomalous Zeeman effect [Dem10]. The normal Zeeman effect does not include the electron spin, which makes the anomalous Zeeman effect the more common one. In the semi-classical model the electron moves in circular orbits around the core, but the angular momentum is quantized to $|l| = \sqrt{l(l+1)}\hbar$. The circular motion of the electron induces a current and thus a magnetic moment which is described by Eq. 2.25:

$$\mathbf{p}_m = I \cdot \mathbf{A} = I \cdot \pi r^2 \hat{\mathbf{n}} = -evr/2\hat{\mathbf{n}} , \quad (2.25)$$

where $\mathbf{A} = \pi r^2 \hat{\mathbf{n}}$ is the enclosed area of the electron motion, r is the electron radius and $\hat{\mathbf{n}}$ is the normal vector perpendicular to the enclosed area, e is the electron charge and v is the electron velocity. Taking the angular momentum $\mathbf{l} = \mathbf{r} \times \mathbf{p} = rm_e v \hat{\mathbf{n}}$ into account, the magnetic moment can be written as:

$$\mathbf{p}_m = \boldsymbol{\mu}_l = -\frac{e}{2m_e} \mathbf{l} = -\frac{\mu_B}{\hbar} \mathbf{l} , \quad (2.26)$$

where m_e is the electron mass and $\mu_B = (e\hbar)/(2m_e)$ is the Bohr magneton. The potential energy E_{pot} in an external magnetic field \mathbf{B} is $E_{pot} = -\mathbf{p}_m \cdot \mathbf{B}$. Considering the magnetic field in z direction to be $\mathbf{B} = \{0, 0, B_z\}$ the scalar product between magnetic moment and magnetic field is calculated to:

$$E_{pot} = \frac{e\hbar}{2m_e} mB = \mu_B mB , \quad (2.27)$$

using $l_z = m\hbar$, where m is the magnetic quantum number with $-l \leq m \leq l$. Eq. 2.27 shows that the former $2l + 1$ degenerated energy levels split up in an external magnetic field \mathbf{B} with equidistant distance between two Zeeman levels of $\Delta E = \mu_B B$. This energy splitting is called the normal Zeeman effect.

The energy splitting results in a change of the emission and absorption profile of the atoms. Assuming σ^+ polarized photons a magnetic field $\mathbf{B} = \{0, 0, B_z\}$ will result in an alignment of the photon spin to a value of $+\hbar$. If these photons are absorbed in the atom this will result in a change of the z component of the angular momentum by $\Delta l_z = +\hbar$ and thus transitions with $\Delta m = m_2 - m_1 = +1$ will be observed. σ^- polarized light will induce transitions with $\Delta m = -1$. The same counts for the emission: If emitted light is observed in direction parallel to the magnetic field σ^+ and σ^- polarized light will be observed. If the emission is observed perpendicular to the magnetic field three linear polarized components will be observed: One unshifted vector with \mathbf{E} parallel to \mathbf{B} and two shifted components with $\mathbf{E} \perp \mathbf{B}$ [Dem10].

The Zeeman splitting described above is only valid for states with total spin momentum $\mathbf{S} = \sum \mathbf{s}_i = \mathbf{0}$. If the electron spin \mathbf{s} is taken into account, the emission spectrum becomes more complicated. Assuming the external magnetic field to be smaller than the magnetic field induced by the circular movement of the electron the Zeeman splitting is smaller than the fine structure splitting. As a consequence, the total angular momentum $\mathbf{j} = \mathbf{l} + \mathbf{s}$ with the absolute value $|j| = \sqrt{j(j+1)}\hbar$ stays constant in the external magnetic field. But the total magnetic moment $\boldsymbol{\mu}_j = \boldsymbol{\mu}_l + \boldsymbol{\mu}_s$ changes due to torsional moment induced by the magnetic field.

$$\mathbf{D} = \boldsymbol{\mu}_j \times \mathbf{B} , \quad (2.28)$$

with the component $j_z = m_j \hbar$ with values $-j \leq m_j \leq j$. As a consequence, the magnetic moment $\boldsymbol{\mu}_j$ and the total angular momentum \boldsymbol{j} are not parallel anymore. Using the values for the angular momentum $\boldsymbol{\mu}_l = -\mu_B/\hbar \boldsymbol{l}$ and for the spin moment $\boldsymbol{\mu}_s = -g_s \mu_B/\hbar \boldsymbol{s}$ (with $g_s \approx 2$) the total magnetic moment can be calculated to:

$$\boldsymbol{\mu}_j = -\frac{e}{2m_e} (\boldsymbol{l} + g_s \boldsymbol{s}) \quad (2.29)$$

The magnetic moment $\boldsymbol{\mu}_j$ processes around the direction of \boldsymbol{j} . To calculate the energy splitting of the states the time average of the magnetic moment needs to be calculated (Eq. 2.30):

$$\langle \boldsymbol{\mu}_j \rangle = g_j \mu_B \cdot |\boldsymbol{j}|/\hbar, \quad (2.30)$$

with the Landé factor g_j :

$$g_j = 1 + \frac{j(j+1) + s(s+1) - l(l+1)}{2j(j+1)}. \quad (2.31)$$

Taking the thoughts from above into account and assuming a magnetic field in z direction $\boldsymbol{B} = \{0, 0, B_z\}$ the z component of the magnetic moment can be calculated to:

$$\langle \boldsymbol{\mu}_j \rangle_z = -m_j \cdot g_j \cdot \mu_B \quad (2.32)$$

and the additional energy in the magnetic field is

$$E_{m_j} = -\langle \boldsymbol{\mu}_j \rangle_z \cdot B_z. \quad (2.33)$$

As can be seen in Eqs. 2.30 and 2.31 the Zeeman energy splitting depends on the quantum numbers l and s thus each of the degenerated $2l+1$ states splits up different for each combination of the quantum numbers in comparison to the equidistant three levels described by the normal Zeeman effect. Thus, the anomalous Zeeman effect is much more complicated than the normal one [Dem10]. The Landé factor can only be calculated by Eq. 2.31 for ls-coupling. If the ls-coupling is not the dominant term, the calculation of the Landé factor becomes more complicated and can be looked up for example in the NIST database [Kra18]. Note that the role of the Zeeman effect for the emission spectra is different for different species of atoms in the magnetized plasma. For the $2P_{1/2}$ state of hydrogen the zeeman splitting is 3.85×10^{-6} eV at a magnetic field of 0.1 T and can be neglected compared to the fine structure splitting which is 1.81×10^{-4} eV. For the emission of other gases, e.g. for Ar this is not the case and the Zeeman splitting needs to be taken into account (as can be seen in Sec. 5).

To analyze a Zeeman splitted spectrum also the relative components of the separated Zeeman components need to be known. The relative intensities can be calculated using the Wigner 3-j symbols (Eq. 2.34), assuming that all sublevels are equally populated [Cow81].

$$I \propto \begin{pmatrix} j_1 & 1 & j_2 \\ -m_1 & m_1 - m_2 & m_2 \end{pmatrix}^2, \quad (2.34)$$

where j_1 is the quantum number of the upper and j_2 of the lower level and m_1 and m_2 are the corresponding magnetic quantum numbers.

2.7 Broadening Mechanisms

In a low density laboratory plasma only two line broadening mechanisms are of importance, the natural line broadening and the Doppler broadening. The instrumental broadening of the spectrometer will be discussed later in in Sec. 3.3.1.

2.7.1 Natural Broadening

The natural line broadening is caused by the finite lifetime of an excited state. The energy of excited states is smeared out due to the Heisenberg uncertainty principle [Hut02]:

$$\Delta E \Delta t \approx \hbar \Rightarrow \Delta E \approx h/2\pi\tau, \quad (2.35)$$

where τ is the lifetime and depends on the Einstein transition probabilities of the upper and lower states:

$$\frac{2}{\tau} = \sum_j A_{n_i j} + \sum_j A_{n_f j} \quad (2.36)$$

The shape of the broadening is described by a Lorentzian function [Hut02]

$$I(\lambda) = I(\lambda_0) \frac{1}{1 + \left[\left(\frac{\lambda}{\lambda_0} - \frac{c}{\lambda_0} \right) 2\pi\tau \right]^2}, \quad (2.37)$$

where λ_0 is the center wavelength of the center line. The Lorentzian profile is normalized to one.

$$\int L(\lambda) d\lambda = 1 \quad (2.38)$$

The full width at half maximum (FWHM) is $\Delta\lambda_{1/2}^L = \lambda^2/\pi c\tau$. The natural line width is very small compared to the other broadening mechanisms, but nevertheless it is included in the line analysis of the spectral lines in this thesis, due to the high resolution of the spectrometer.

2.7.2 Doppler Broadening

The second important broadening mechanism is the Doppler broadening. Due to the motion of the atom the frequency of the emitted radiation is effected by the Doppler effect (a detailed description of the Doppler effect can be found in Sec. 2.3). The emission profile is described by a Gaussian function:

$$G(\lambda) = \frac{1}{\beta\sqrt{\pi}} \exp\left(\frac{-(\lambda - \lambda_0)^2}{\beta^2}\right), \quad (2.39)$$

where $\beta = 2kT_i\lambda_0^2/Mc^2$, k is the Boltzmann constant, T_i is the ion temperature, λ_0 is the wavelength at the line center, M is the ion mass and c is the speed of light in vacuum [Coo66]. The Gaussian profile is normalized to one (2.40) and the FWHM of the Gaussian function $\Delta\lambda_{1/2}^G$ can be calculated using formula 2.41 [Kun09].

$$\int G(\lambda) d\lambda = 1 \quad (2.40)$$

$$\lambda_{1/2}^G = \lambda_0 \sqrt{8 \ln(2) \frac{kT_i}{Mc^2}} \quad (2.41)$$

Using the FWHM of the Doppler broadening the ion temperature T_i can be calculated. Note that T_i has not to be the same as the electron temperature T_e . The reason is that the momentum transfer cross sections are small for particles with very different masses [Coo66].

2.7.3 Stark Broadening

A third broadening mechanism is the Stark broadening. Here the spectral line is broadened due to the interaction of the transition electron with other charge particles in the plasma (electrons or ions) via the Coulomb interaction. The Hamiltonian of the interaction can be described the following [Kun09]:

$$\Delta H = -e\mathbf{r}\mathbf{E}(t) , \quad (2.42)$$

where $\mathbf{Q} = -e\mathbf{r}$ is the dipole momentum operator of the emitting bound electron and $\mathbf{E}(t)$ is the electric field of the plasma at the position of the radiator. The electric field strength is given by [Kun09]

$$\mathbf{E}(t) = \frac{1}{4\pi\epsilon_0} \left(\sum_i z_i e \frac{\mathbf{r}_i(t)}{[r_i(t)]^3} - \sum_j e \frac{\mathbf{r}_j(t)}{[r_j(t)]^3} \right) , \quad (2.43)$$

where $\mathbf{r}_i(t)$ and $\mathbf{r}_j(t)$ are the positions of the ions and electrons in the plasma and z_i is the charge state of the ions. Higher terms in the Hamiltonian can be normally neglected [Kun09]. This interaction Hamiltonian ΔH is put in the time-dependent Schrödinger equation and has to be solved. This shows very clearly that there is no general formula for describing the Stark broadening, the Schrödinger equation has to be solved for every single situation separately. Nevertheless, there are approximations, which can be used to calculate the order of magnitude of the Stark broadening. For example for the H_α line, the Stark broadening can be calculated with Eq. 2.44 in a range of the electron density n_e between $1 \times 10^{23} \text{ m}^{-3} - 1 \times 10^{25} \text{ m}^{-3}$ [Kun09].

$$\Delta\lambda_{1/2}[\text{nm}] \approx 2.8 \times 10^{-17} (n_e[\text{m}^{-3}])^{0.72} \quad (2.44)$$

Using this formula for a typical density of the PSI-2 device of $1 \times 10^{17} \text{ m}^{-3}$ $\Delta\lambda_{1/2} \approx 5 \times 10^{-5} \text{ nm} = 5 \times 10^{-4} \text{ pm}$ is achieved. It is much smaller than the Doppler broadening under the used experimental conditions and can therefore be neglected in the analysis of the measurements.

CHAPTER 3

EXPERIMENTAL SETUP

In this chapter the plasma source and the experimental setup to detect the fast atoms are discussed. First, the PSI-2 device (Sec. 3.1), the optical setup and the different target holders at PSI-2 are presented (Sec. 3.2). In Sec. 3.3 the different diagnostic at PSI-2 are discussed with focus on the optical emission spectroscopy (OES).

3.1 The PSI-2 Device

The experiments in this thesis are performed at the linear plasma device PSI-2 in Jülich, Germany. A cross section of the PSI-2 device with annotations describing the different parts of the machine is shown in Fig. 3.1. PSI-2 was designed to provide a steady-state cylindrical plasma with similar conditions like the edge plasma in future fusion reactors. The device is used for fuel retention [Rei15] and plasma-material interaction studies [Kre15]. The plasma is created by an arc discharge between a cathode and an anode. The cathode, made of LaB_6 , is set on a negative potential and heated up to a temperature of around 1600°C . LaB_6 is a common used electron source because of its very low work function of around 2.7 eV [AB72]. The electrons emitted by the cathode are accelerated towards a hollow Mo anode which is set to the ground potential [Kre15]. To confine the plasma, six magnets are used with a maximum magnetic field of around 0.1 T [Kre15]. The diameter of the plasma column is approximately 10 cm . The common used gases in the PSI-2 device are hydrogen (H) and deuterium (D), but also other gases, such as argon (Ar), krypton (Kr), xenon (Xe) or nitrogen (N) are frequently used for plasma-surface interaction studies. In this thesis H, D, Ar and Kr are mainly used. Moreover, it is possible to adjust a mixture of different gases for plasma production. The overall length of the device including the axial manipulator is around 6 m , the exposition chamber has a length of around 2 m . Due to the hollow cylindrical profile of cathode and anode, the plasma has a hollow profile in temperature and density [Kre15], which can be seen in the Langmuir probe measurement in Fig. 3.2. Typical plasma parameters are provided in Tab. 3.1. The sample is observed at two different observation ports, namely at the 35° port and the side observation port, corresponding to 90° . To bring the sample into the plasma, two manipulators can be used, the radial and the axial

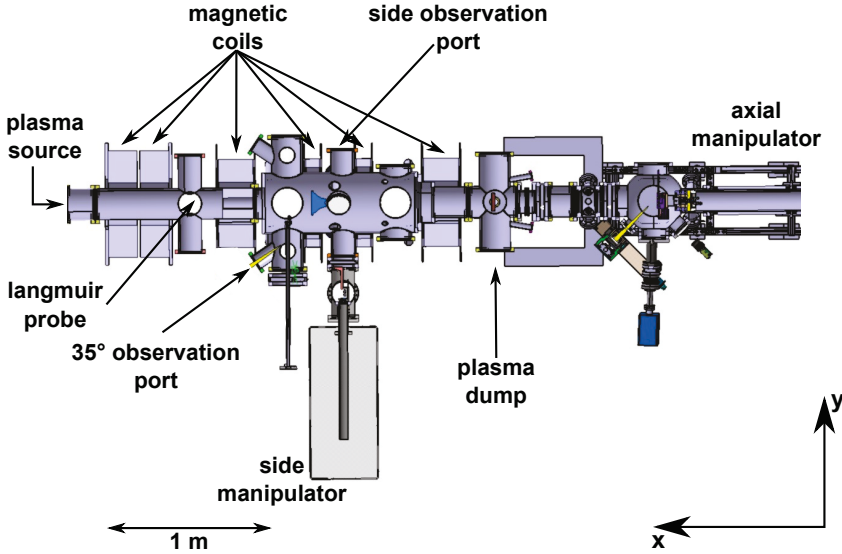


Fig. 3.1: Cross section of the PSI-2 device (with courtesy of A. Terra, FzJ). The annotations are added by the author.

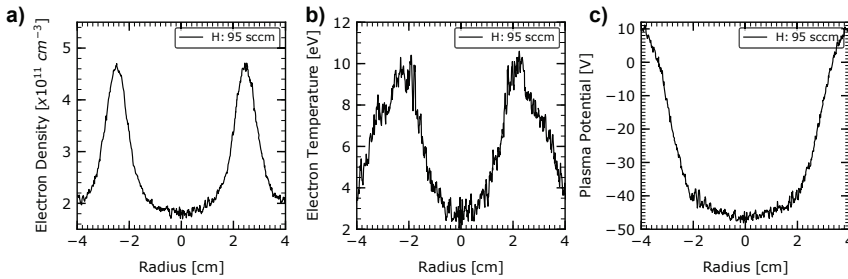


Fig. 3.2: Langmuir probe measurement of a H plasma with a gas flux of 95 sccm. In (a) the electron density n_e , in (b) the electron temperature T_e and in (c) the plasma potential U_p are depicted. Note, a negative radius means that the langmuir probe is moving into the plasma, a positive means the probe is moving out of the plasma.

Magnetic field in exposition chamber	0.1 T
Arc current	≤ 1000 A
Arc voltage	≤ 150 V
Electron temperature T_e	1 – 25 eV for D, up to 40 eV for He
Ion temperature T_i	0.5 – 5 eV
Electron density n_e	$\approx 10^{10} - 10^{13} \text{ cm}^{-3}$
Incident ion energy	1 – 300 eV

Table 3.1: Typical plasma parameters of the PSI-2 device taken from [Kre15].

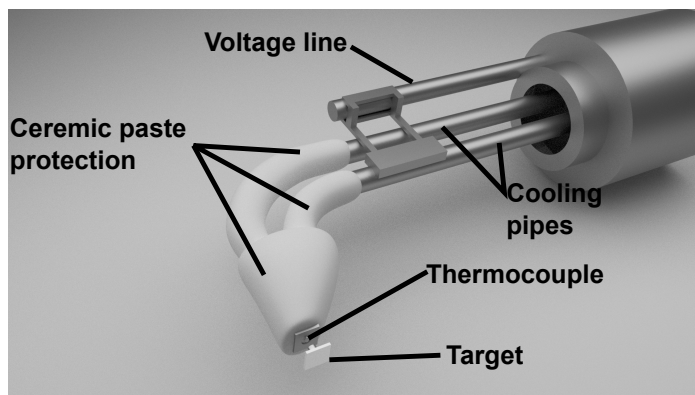


Fig. 3.3: 3D model of the side manipulator. Both models are created and rendered using the software Blender 3D [Ble18].

manipulator (see Fig. 3.1). In Sec. 4 it is always mentioned which manipulator is used for the specific measurement. The samples in the experiments are brought into the plasma at the maximum of the hollow profile at ≈ 2.5 cm in y direction and ≈ 1.5 m away from the anode in x direction. Both manipulators have advantages and disadvantages and will be explained in more detail in Sec. 3.2. The diagnostics used at the PSI-2 device are described in Sec. 3.3. For more detailed information about PSI-2 I refer to the papers [Kre15] and [KF04].

3.2 Manipulator at PSI-2

In this thesis metallic targets are used to create fast atoms. The targets have a size of around 1×1 cm, with a small pin at the bottom to mount the sample onto the holder (as shown in Fig. 3.3 or Fig. 3.4). The advantage of a small metallic samples is that surface potential, material and the area in which fast atoms can be created are well known. The sample holders are also called manipulators, because they are movable and the sample can be brought in and out of the plasma during operation.

3.2.1 Radial Manipulator

The radial manipulator (also called side manipulator) is located in a distance of approximately 1.5 m from the plasma source (Fig. 3.1). The mounted sample is water cooled and is hold on a constant temperature of around 30°C . A scheme of the side manipulator is depicted in Fig. 3.3. The manipulator is movable in y direction, so that a radial scan of the plasma can be performed. On the x axis it stays at a fixed position. The temperature of the target can be monitored using a thermocouple which is positioned directly behind the surface. Furthermore, it is possible to apply a negative voltage to the target between 0 V and -300 V. Because of arcs between sample and anode at higher voltages only voltages up to -220 V were applied. The parts of the manipulator, which are exposed to the plasma are protected using a ceramic paste, so that the voltage is only applied to the sample and not to the rest of the manipulator.

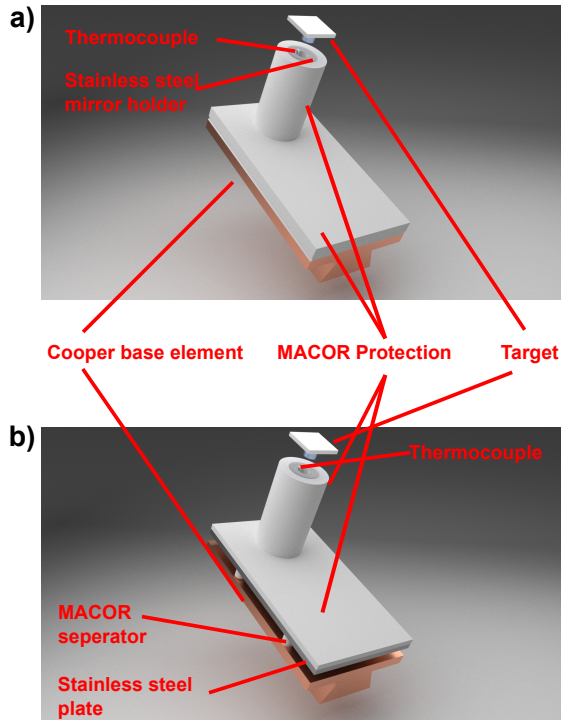


Fig. 3.4: 3D models of the two target holders used on the axial manipulator. In (a) the cooled target holder and in (b) the heated target holder are shown. With the MACOR separators the sample is thermally decoupled from the cooled cooper basement. Both models are created and rendered using the software Blender 3D [Ble18].

3.2.2 Axial Manipulator

For the axial manipulator (or target station) two different sample holders were used. The difference between them is that one holder is cooled and the other is not. In comparison to the radial manipulator the y position of this manipulator is fixed and the x position can be varied freely within the exposition chamber. Similar to the radial manipulator a negative voltage can be applied to the target holder. Like shown in Fig. 3.4 (a) and (b) both target holders are built on a cooper base element. This cooper element is cooled with water, which has a temperature of 20 °C. If a negative voltage is applied to the target holder, the complete cooper basement is set under this potential. Because only the sample should be biased in the plasma the cooper basement is protected with a MACOR plate. The plate acts as an isolator, so that the plasma facing side of the target holder is not under the applied potential and the potential is applied only to the sample. For the electrical connection between the cooper base element and the sample a hollow stainless steel cylinder is used in which the sample can be mounted. Inside the cylinder the thermocouple is located as well. The stainless steel cylinder is also protected with a MACOR surrounding (see Fig. 3.4). The cooling for the non cooled target holder cannot be switched off. Therefore four MACOR pins are used to thermally decouple the cooled cooper base

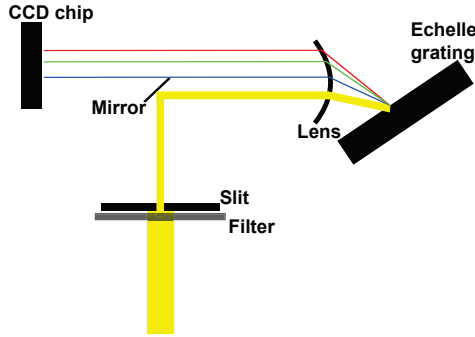


Fig. 3.5: Scheme of the used high resolution Echelle spectrometer (HRES). The light coming from the fiber is focused on the entrance slit of the spectrometer. In front of the entrance slit a interference filter is positioned to filter out all unnecessary wavelengths of the light. In the spectrometer the light is reflected from a mirror and focused on an Echelle grating. The grating separates the light with respect to the wavelength and reflects it back through the lens on an EMCCD chip.

from the rest of the target holder. To still apply a potential to the target, above the MACOR pins a stainless steel plate is located which is connected to sample. The plate is again covered by a MACOR plate to isolate it from the plasma. In this configuration the plasma can be used to heat up the target up to 500 °C depending on the tested material and plasma conditions.

3.3 Diagnostics at PSI-2

At the PSI-2 device different kind of diagnostics are used to investigate the plasma-material interaction. A double Langmuir probe is used to achieve the plasma parameters like electron temperature T_e , electron density n_e , ion flux Γ_i and plasma potential U_p . The Langmuir probe consists of two tungsten pins which are 1.5 mm in diameter and length and the spacing between them is 1.5 mm. The two pins are surrounded by a ceramic tube. At the moment the double probe is used as a single probe by biasing only one pin with 50 V and a frequency of 50 Hz. The obtained I-V curve is analyzed by a software written by Gennady Sergienko.

To check the values of n_e and T_e obtained by the Langmuir probe and to study turbulent transport in the device a Thomson scattering system is installed at the PSI-2 [Hub17]. For direct observation of the plasma and to obtain gas and ion temperature optical emission spectroscopy (OES) is used [Kre15].

3.3.1 High Resolution Echelle Spectrometer (HRES)

The spectroscopic measurements in this thesis are performed with a high resolution Echelle spectrometer (HRES), which is schematically depicted in Figure 3.5. The spectrometer is built in a Littrow configuration, thus incident angle and angle of reflection are equal. In the Littrow configuration the spectral order m , in which the

Spectrometer type	Echelle spectrometer in Littrow configuration
Groove density [grooves/mm]	79.015
Dispersion [$\text{\AA}/\text{pixel}$]	$\approx 1 \text{ pm}$
Camera type	Andor iXion DU-888 EMCCD
Chip size	$1024 \times 1024 \text{ px}^2$
Spectral order	$m = 37 \text{ (H}_\alpha\text{)}, m = 49 \text{ (H}_\beta\text{)}$
Grating angle	$286.86^\circ \text{ (H}_\alpha\text{)}, 290.24^\circ \text{ (H}_\beta\text{)}$

Table 3.2: *Characteristics of the HRES.*

emission is observed, can be calculated using Eq. 3.1 [Pal02]:

$$m = \frac{2 \sin(\alpha)}{G\lambda} = \frac{2d \sin(\alpha)}{\lambda}, \quad (3.1)$$

where α is the angle between grating and the surface normal, $G = 1/d$ is the groove density, d is the distance between two grooves and λ is the wavelength which should be analyzed in the spectrometer. Using Eq. 3.1 one found that H_α is measured in the spectral order $m = 37$ and H_β in the spectral order $m = 49$. The light is collect at the PSI-2 using a 30 m optical multi mode fiber. The spectrometer is self constructed in the institute and uses an Andor iXion DU-888 EMCCD camera with a size of $1024 \times 1024 \text{ px}^2$. The light is focused on a slit and reflected into the spectrometer using a mirror. By varying the slit width the resolution of the spectrometer and the measured intensity can be adjusted. In front of the slit a band pass filter can be placed to filter out all wavelengths except of the one, which should be analyzed. After the light is reflected from the mirror it is focused with a lens onto the grating. The grating has 79.015 grooves/mm and can be rotated to observe other wavelengths on the camera. The grating separates the light with respect to the wavelength and reflects it back on the focus lens. From there it is guided onto the EMCCD image sensor. The spectrometer has a dispersion of around $\approx 1 \text{ pm/px}$ and a resolution of $\approx 5 \text{ pm/px}$. The characteristics of the used spectrometer are summarized in Tab. 3.2.

3.3.2 Calibration of the HRES and Analysis of the Spectrum

In Sec. 3.3.1 the movable grating of the spectrometer was mentioned to change the wavelength range of interest which is observable in the camera. A disadvantage of this setup is that there is no absolute wavelength calibration of the spectrometer. The calibration needs to be done every time the grating is rotated by using a calibration lamp. In this thesis a D calibration lamp (Edmund optics: Deuterium Spectrum Tube) is used. Beside D a little amount of H is present in the gas tube, so that the spectral lines of D and H can be observed simultaneously (Fig. 3.6). The resolution of the spectrometer is high enough to observe the fine structure of the Balmer transition lines. As a consequence, for the fitting procedure not a single Voigt function but a sum of seven Voigt functions (each for a fine structure transition line) are used to fit the spectrum. For the fitting procedure the python algorithm **lmfit** is used [New14]. Note, a Voigt function is the convolution of a Gaussian and a Lorentzian function (Eq. 3.2):

$$V(\lambda) = (G * L)(\lambda) = \frac{A \operatorname{Re}[w(z)]}{\sigma \sqrt{2\pi}}, \quad z = \frac{\lambda + i\gamma}{\sigma \sqrt{2}} \quad (3.2)$$

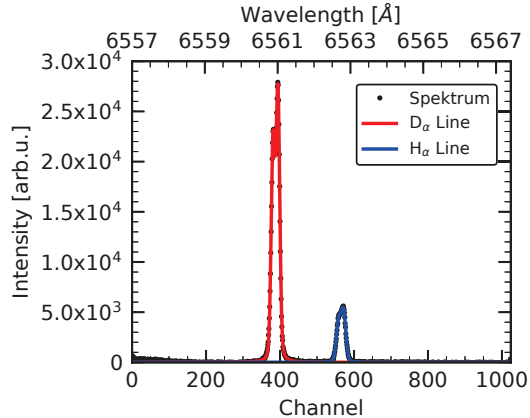


Fig. 3.6: Measurement of the calibration lamp. The left peak is the D_α line and the right is the H_α line. The fine structure of both peaks can be observed in this spectrum. The colored functions are the fits of both spectral lines.

where A is the amplitude, σ is the standard deviation of the Gaussian function, γ is the full width of the Lorentzian function, and w is defined as $w = e^{-z^2} \operatorname{erfc}(-iz)$, with the complimentary error function erfc [New14]. The full width half maximum (FWHM) of the Gaussian function is $f_G = 2\sigma\sqrt{2\ln(2)}$ and of the Lorentzian function $f_L = 2\gamma$. The Voigt function is not normalized but scaled with the amplitude A to fit the experimental data. A Voigt function is used, because the high resolution of the spectrometer allows to distinguish between Doppler broadening (Gaussian function) and the natural line broadening (Lorentzian function). The fitted lines can be used to calculate the mean wavelength λ_{mean} of the peak using Eq. 3.3:

$$\lambda_{mean} = \frac{\sum_i \lambda_i A_i g_i}{\sum_i A_i g_i}, \quad (3.3)$$

where λ_i is the wavelength, A_i is the Einstein coefficient and g_i is the statistical weight of fine structure element i . Eq. 3.3 can also be applied to calculate the center position of the peak in pixels by replacing the wavelength λ with pixel position x . This procedure is done separately for the H_α and the D_α line. For both lines a center position in the wavelength scale and in the pixel scale is obtained. Using both information of both spectral lines a linear dispersion relation can be calculated. For this procedure at least two known spectral lines are needed to be visible in the measured spectrum. Note, that this calibration is only valid at one position of the grating. If the grating position is changed a new calibration needs to be done. Also for each day and between measurements the spectrometer is calibrated.

3.3.3 Passive Emission of Balmer Lines in PSI-2

The Balmer lines in the PSI-2 device consists of two different components [WMF07] as can be found in Fig. 3.7. The first component is called the cold one, because it is caused by cold atoms and molecules at the plasma edge. The second is called the hot component, because it is caused by charge-exchange between fast ions from

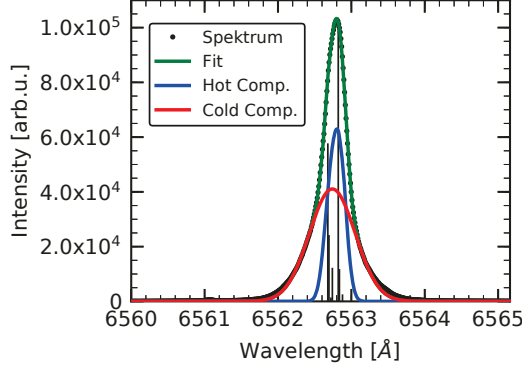


Fig. 3.7: H_α line measured with the high resolution Echelle spectrometer at a LOS of 35° . The H flux was 85 sccm and the neutral gas pressure was $p = 4.7 \times 10^{-2}$ Pa. The electron density was $n_e = 3.5 \times 10^{11} \text{ cm}^{-3}$ and the electron temperature was $T_e = 11 \text{ eV}$. To fit the spectral line two functions are used for the hot (red curve) and the cold (blue curve) component. Each function is the sum of seven single Voigt profiles for each line of the fine structure of hydrogen. The theoretical fine structure lines are shown as thin lines in the center of the spectrum and are taken from the NIST database [Kra18].

the inside of the plasma and atoms in the plasma (Eq. 3.6) and electron excitation afterwards (Eq. 3.7). The cold component is the result of excited neutrals either by electron excitation (Eq. 3.4) or due to dissociation of hydrogen molecules (Eq. 3.5) [Mey99]:



and for the hot component:



As a consequence the spectral line is fitted by using two different functions, one for the cold and one for the hot component (see Fig. 3.7). Thus, both parts of the spectral line need to be taken into account for fitting the total spectral line. The function describing either the hot or the cold component is again a sum of seven single Voigt functions for the seven fine structure lines of H_α . Moreover, it needs to be mentioned that the measured spectrum of the Balmer lines is shifted towards the theoretical values taken from the NIST database [Kra18]. This shift is the result of a rotation of the plasma due to a force $\mathbf{F} = \mathbf{E} \times \mathbf{B}$ which interacts with the ions inside the plasma [Mey99]. As a consequence, the ions begin to rotate and the rotation direction is clockwise in direction from the plasma source to the target holder. This rotation can be analyzed by comparing the central position of the measured spectrum with the known theoretical position of the lines. In Fig. 3.7 a measurement of the H_α line is shown, at a gas flux of H of 85 sccm. The electron temperature at this condition was $T_e = 11 \text{ eV}$ and the electron density $n_e = 3.5 \times 10^{11} \text{ cm}^{-3}$. The neutral

gas pressure in the exposition chamber was $p = 4.7 \times 10^{-2}$ Pa. Analyzing the hot component the ion temperature is determined to $T_i = 1.94$ eV and with the cold component the gas temperature is calculated to $T_g = 0.1$ eV. The rotation of the cold component is calculated to $\approx 0.2 \text{ km s}^{-1}$ and for the hot component $\approx 2.5 \text{ km s}^{-1}$. The rotation of the hot component is much higher compared to the cold component because the ions are influenced by the magnetic field before the charge-exchange interaction with the background gas. The neutral atoms, the source of emission for the cold component, are not influenced by the magnetic field.

CHAPTER 4

EXPERIMENTAL RESULTS OF THE EMISSION OF FAST ATOMS

The chapter starts with the discussion of the plasma conditions used in the experiments. In Sec. 4.2 and Sec. 4.3 the dependence of the Doppler-shifted emission on the applied surface potential and material is shown. Using the knowledge from the previous sections, in Sec. 4.4 a new kind of diagnostic is developed, which measures the spectral reflectance of the investigated surface during plasma exposition. In Sec. 4.5 this diagnostic is used to determine the spectral reflectance for various target materials. A summary of these results can be found in [Dic18a]. These measurements built the basis for the following experiment campaigns where the limits of the new diagnostic are tested. Experiments are performed to obtain not only the spectral reflectance of the target at the wavelength of H_{α} , but also at the position of H_{β} (Sec. 4.7). Moreover, the radial plasma profile of PSI-2 can be measured (Sec. 4.8) as well as the polarization of the reflected light (Sec. 4.9) and the *in situ* degradation of the target surface during plasma exposure (Sec. 4.10). In these measurements also the theoretical dependence of the refractive index on the temperature given by Kikuo Ujihara in 1972 [Uji72] was tested. For a better understanding of the emission of the fast atoms a new model is developed to fit the Doppler-shifted components and the passive Balmer line simultaneously (Sec. 4.11). Finally, in Sec. 4.12 the Doppler-shifted emission of fast H atoms in different gas mixtures of H and other noble gases are tested.

4.1 Characterization of the H-Ar Plasma in PSI-2

In Fig. 4.1 typical Langmuir probe measurements are shown. The measurements are performed with a H-Ar plasma with a gas flux of 40 : 40 sccm and 80 : 80 sccm. These are two typical gas flows used for experiments in this thesis. The hollow plasma profile of the PSI-2 device already mentioned in Sec. 3.1 can clearly be observed using the Langmuir probe (Fig. 4.1). In the plasma a low electron density of only $4 \times 10^{10} \text{ cm}^{-3}$ for 40 : 40 sccm and $6 \times 10^{10} \text{ cm}^{-3}$ for 80 : 80 sccm is detected. The neutral gas pressure is in the range of 0.1 Pa for both experiments. Beside the electron density n_e , the electron temperature is low at a constant value of around

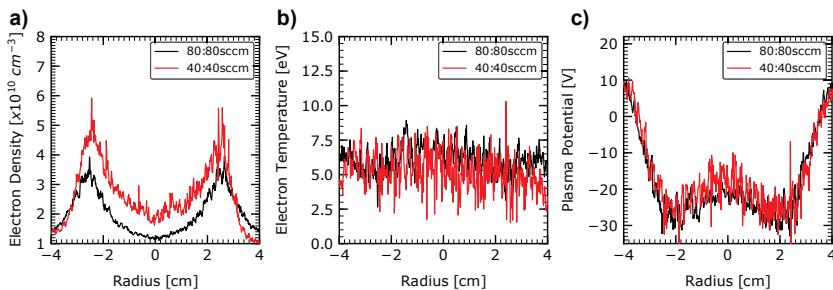


Fig. 4.1: Langmuir probe measurement for two different plasma conditions with two different gas flows namely 40 : 40 sccm and 80 : 80 sccm. In (a) the electron density n_e , in (b) the electron temperature T_e and in (c) the plasma potential U_p is depicted. Note, a negative radius means that the langmuir probe is moving into the plasma, a positive means the probe is moving out of the plasma. The image is mainly taken from [Dic18a].

6 eV for both plasma conditions. In Fig. 4.1 (c) the plasma potential for both plasma conditions is depicted and has a value of around -30 eV at maximum. The plasma values of n_e and T_e are representative for all measurements in a H-Ar mixed plasma presented in this thesis.

To make sure that the line emission is neither disturbed by effects like the Stark effect nor by emission from accelerated ions in the sheath two conditions need to be fulfilled (Eqs. 4.1 and 4.2):

$$l_{cx} = 1/n_g \sigma_{cx} \gg d, \quad (4.1)$$

$$l_{\lambda_0} = \nu \tau \gg d, \quad (4.2)$$

where l_{cx} is the mean-free path of the charge-exchange recombination of the ions in the sheath, $n_g = p/kT_g$ is the neutral gas density, where p is the neutral gas pressure, k is the Boltzmann constant and T_g is the neutral gas temperature, σ_{cx} is the charge-exchange cross section, d is the Debye sheath thickness, l_{λ_0} is the characteristic distance the atom moves before the emission process, ν is the velocity of the atom and $\tau = 1/\sum_k A_{if}$ is the lifetime of the excited level i and A_{if} is the Einstein coefficient for the transition from level i to f and the sum extends over all lower lying levels f . Eq. 4.1 describes that the mean-free path of the charge-exchange recombination is bigger than thickness to avoid emission by accelerated ions. Eq. 4.2 makes sure that no emission by fast atoms takes place inside the Debye sheath to avoid Stark splitting of the emission line.

Using typical values of the PSI-2 device at our conditions, an electron density $n_e \approx 5 \times 10^{10} \text{ cm}^{-3}$, an electron temperature of $T_e \approx 6 \text{ eV}$, a neutral gas pressure $p \approx 0.1 \text{ Pa}$ and kinetic energy of the atoms of 100 eV are assumed. Using these values a sheath thickness of $d = 0.5 \text{ mm}$ using the Child-Langmuir Law (Eq. 2.3) is achieved [Ben09]. In comparison to the sheath thickness, the distance $l_{\lambda_0} = \nu \tau$ the atoms can move before they emit a detectable amount of photons can be calculated to 1.4 mm (assuming a kinetic energy of the excited atoms of 100 eV and a lifetime of the $n = 3$ state of $\tau = 10 \text{ ns}$ [BS77]). Thus, the distance of the l_{λ_0} is a factor of 3 greater than the sheath thickness d , which proves two important facts. The first one

is that emission inside the sheath is avoided, which would make the analysis of the spectrum very difficult. Inside the sheath very high electric fields are present as a result of the potential drop between plasma and metallic surface. This high electric field would cause a strong Stark splitting, which makes the spectrum very complex. Thus, condition 4.2 is fulfilled in the used experimental setup. On the second hand, the difference between l_{λ_0} and d demonstrates that no Doppler-shifted emission by particles created due to charge-exchange interaction is observed, because this could only take place in sheath. To exclude charge-exchange interaction effect one can also take a look at the mean-free path for charge-exchange interaction $l_{cx} = 1/(n_g\sigma_{cx})$. The mean-free path can be estimated to $l_{cx} = 2.6$ m assuming a neutral gas density $n_g = 1.25 \times 10^{12} \text{ cm}^{-3}$, a neutral gas pressure of $p = 0.1$ Pa, a neutral gas temperature of $T_g = 0.5$ eV and a charge-exchange cross section of $\sigma_{cx} = 3 \times 10^{-15} \text{ cm}^2$ [JRS03]. The comparison of l_{cx} and d shows that charge-exchange in the sheath can be neglected in the experimental setup. As a consequence, the observed Doppler-shifted emission is only the result of fast neutrals created at the target surface (which can also be proven by the material dependence of the kinetic energy of the fast neutrals in Sec. 4.3).

4.2 Doppler-Shifted Emission of Fast Atoms as a Function of the Incident Ion Energy

In this section the dependence of the Doppler-shifted emission on the energy of the incident ions is investigated. For the measurements presented in this section the radial manipulator is used, the gas flow is adjusted to 40 : 40 sccm and the H_α wavelength at 656 nm is measured. In Fig. 4.2 the measured spectra for a Pd sample are shown. The surface potential was varied between -30 V and -220 V, where -30 V is the floating potential at the used plasma conditions. In Fig. 4.2 (a) the spectra is measured at an angle of 90° between surface normal and line-of-sight of the spectrometer. In Fig. 4.2 (b) the spectra for 35° are depicted. The different colors in the graph denote different applied potentials. Note, a negative energy on the x axis corresponds to wavelengths smaller than the unshifted wavelength of the central line.

All observations taken in Fig. 4.2 are also valid for Fig. 4.3 and Fig. 4.4. For clarity these observations are just explained for the Pd target. The first observation presented in Fig. 4.2 (a) is that there is no Doppler-shifted emission detectable at a floating potential of -30 V. The Doppler-shifted emission starts to arise at a target potential of -80 V and increases with increasing potential. This shows that a kinetic energy of ≈ -80 eV of the fast atoms is needed to observe the Doppler-shifted emission.

The fact that the Doppler-shifted emission profile gets broader with a higher applied target potential and thus a higher acceleration of the ions in the Debye sheath demonstrates very clearly that the Doppler-shifted emission can be controlled by only changing the applied potential. One can further see in Fig. 4.2 that the Doppler-shifted wings become broader with higher kinetic energy but the maximum intensity of the emission profile reaches its maximum at a target potential of around -120 V and stays nearly constant at potentials below. Assuming that the integral under the Doppler-shifted component needs to be constant, as well as the Ar density and the

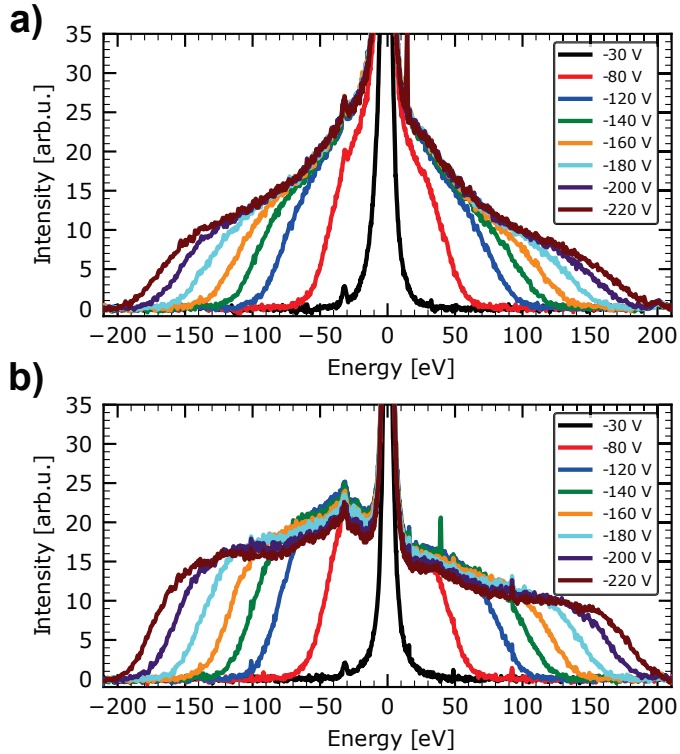


Fig. 4.2: Scan of the target potential between -30 V and -220 V for a Pd sample. The different colors denote the different applied potentials. For the experiment a gas flow of $40 : 40\text{ sccm H:Ar}$ and the radial manipulator was used. Both spectra were measured for H_{α} . (a) Spectra measured at an angle of 90° between surface normal of the target and line-of-sight are shown. (b) Spectra measured at 35° .

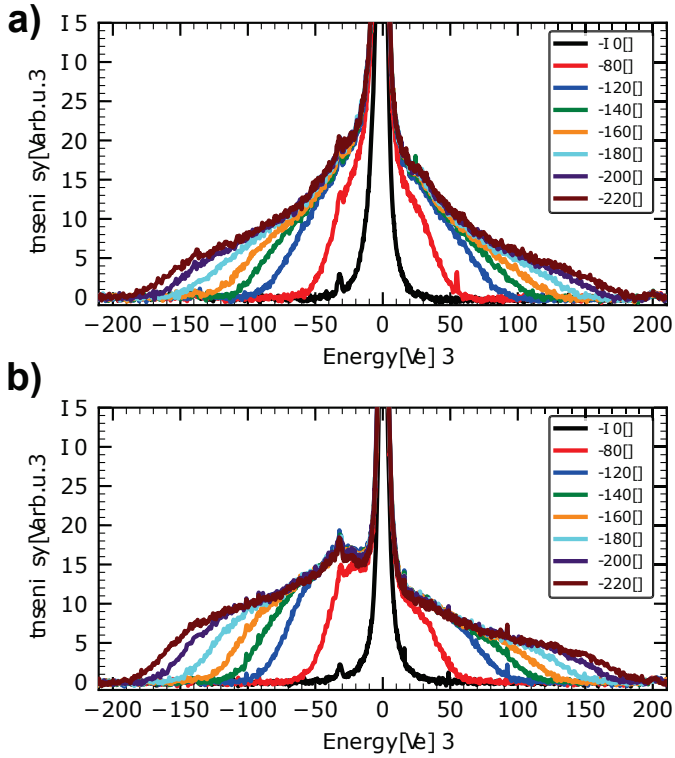


Fig. 4.3: Scan of the target potential between -30 V and -220 V for a Fe sample. The different colors denote the different applied potentials. For the experiment a gas flow of 40 : 40 sccm H:Ar and the radial manipulator was used. Both spectra were measured for H_{α} . (a) Spectra measured at an angle of 90° line-of-sight are shown. (b) Spectra measured at 35° .

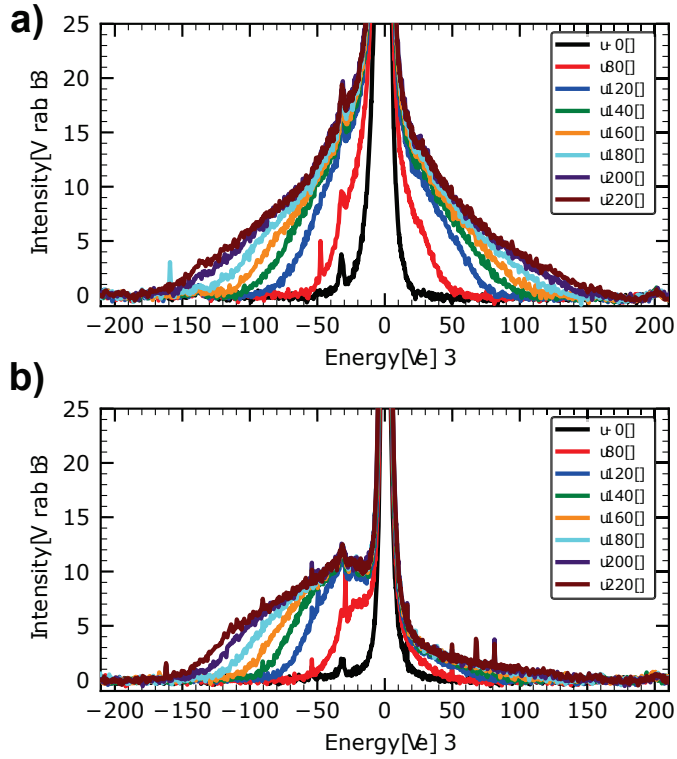


Fig. 4.4: Scan of the target potential between -30 V and -220 V for a C sample. The different colors denote the different applied potentials. For the experiment a gas flow of $40 : 40\text{ sccm H:Ar}$ and the radial manipulator was used. Both spectra were measured for H_α . (a) Spectra measured at an angle of 90° line-of-sight are shown. (b) Spectra measured at 35° .

H density, this observation can be explained with the presence of H_2^+ in the plasma. The H_2^+ ions are accelerated in the Debye sheath as well. After the neutralization process the H_2 molecule can diffuse into two H atoms (called $\text{H}(\text{H}_2^+)$ in the following), but the single atoms have only half the kinetic energy of the molecule. As a consequence, a H_2 molecule with a kinetic energy of 100 eV produces two H atoms with a kinetic energy of around 50 eV (for a precise calculation also the binding energy of the H molecule needs to be taken into account, but this is of weak importance at this place). However, fast atoms with an energy of 50 eV are below the threshold of 80 eV where the Doppler-shifted emission starts to arise, meaning that the emission of $\text{H}(\text{H}_2^+)$ only becomes more important at higher energies. Furthermore, the intensity seems to saturate at an energy of around -100 eV, but then it increases again to a second peak. This peak is caused by emission of $\text{H}(\text{H}_2^+)$ atoms [Phe90; Phe92; Mar18] and proves their presence in the plasma. But in contrast to the observations in high density plasmas where the emission is dominated by atoms created out of H_3^+ ions [AKK04], the emission in a low density plasma is dominated by fast atoms created out of H^+ ions [Dic18a].

A third observation is the difference in the emission profile between the two observation angles of 35° and 90° . The emission profile of the red and blue-shifted component is symmetrical as can be seen in Fig. 4.2 (a) (90°). Compared to that, the emission profile in Fig. 4.2 (b) (35°) is unsymmetrical. This is also true for Figs. 4.3 and 4.4. The difference between the emission profiles can be seen best for C in Fig. 4.4. The reason lies in the difference of the observation directions and is thus a geometrical effect. In Sec. 2.2 it is already explained that the emission profile depends on the angle of observation. In Fig. 2.5 the simple theory is developed that the backscattered neutral atoms are distributed in a half sphere in front of the target surface. From this simple picture one can conclude that the emission profile of fast atoms should be symmetrical, if one observes the emission parallel to the target surface (90° observation angle). For any other angle the emission profile should be more tilted to the blue-shifted direction. Comparing the ratio of the red and blue-shifted component of the different materials it turns out that the ratio is changing with the materials, but is practically independent on the kinetic energy of the atoms. Note that emission by ions accelerated towards the sheath is excluded at the used experimental conditions. The only possible solution for the red-shifted component is light reflection at the metallic surface emitted by the backscattered fast atoms. Taking this into account, the observed Doppler-shifted spectra can be explained, because Pd is a very good reflector at the wavelength of 656 nm ($R = 0.75$) [WGA09] compared to e.g. C ($R \approx 0.2$) [Que85].

4.3 Doppler-Shifted Emission of Fast Atoms as a Function of the Target Material

Beside the surface potential also the material can be varied. The maximal energy of the backscattered atoms can be calculated assuming a binary collision process (Eq. 2.4) [AFM07]. In this process the maximal energy of the backscattered atoms $E_m \propto f(E_0, m, M, \theta_0) \approx e(U - U_p)$ is a function of the incident energy of the ion E_0 , the projectile mass m , the surface mass M , the angle of observation θ_0 . In the low density plasma regime, where the measurements are performed, the maximal energy

of the ions E_0 can be described as $E_0 \approx e(U_s - U_p)$, where U_s is the applied surface potential and U_p is the plasma potential.

Fig. 4.5 clearly shows that the maximum energy of the backscattered atoms crucially depends on the surface mass. For all experiments a potential of -100 V was applied to the target (represented by the black dashed line). The colored areas under the spectra represent the range in which the integral is calculated (for more information about the integral calculation see Sec. 4.4.1). The point where the blue-shifted emission starts to arise is defined as the maximal energy of the backscattered atoms. The onset of the Doppler-shifted emission are determined by calculating first the background level b_{blue} left of the blue-shifted emission profile and the standard deviation of the background level σ_{blue} . The maximum photon energy can then be calculated as $E_m^p = E(I > b_{blue} + i\sigma_{blue})$, where i is a positive integer number. Assuming a Poisson statistic of the measured data and by choosing $i = 3$ the maximal energy E_m^p of the reflected atoms is derived in 99.73% of the confidence interval. The error bar on the onset is the result of the instrumental uncertainty of the spectrometer which is ≈ 5 px. Note that the maximal photon energy E_m^p has to be smaller than the maximum energy of the backscattered atoms E_m by the amount of $E_m^p = E_m - \delta E$, where $\delta E > 0$ and $\delta E \ll E_m$. δE is the energy the fast atoms loses for the excitation process to the $n = 3$ state. Depending on the kind of the excitation δE is different: $\delta E = 10.2$ eV for ground state excitation and $\delta E = 0.12$ eV for excitation transfer by Ar metastables [Dic18a]. The onset for the red-shifted emission is not determined out of the spectrum because of the much worse statistic compared to the blue-shifted onset for some elements, e.g. C (see Fig. 4.4 or Fig. 4.5). Assuming a symmetry of the Doppler-shifted emission, the red-shifted onset is just mirrored along the H_α line. The minimal observable energy E_{min}^p can then be calculated out of the maximal energy by $E_{min}^p = E_m^p \sin(\theta_0)^2$. Note, that this is not the minimal energy of the photons but the minimal energy the diagnostic can detect under a certain angle of observation [Dic18a]. The reflectance can then be calculated using Eq. 4.3.

The onset point of the Doppler-shifted emission crucially depends on the used material. For C the onset point is the lowest with 63 eV, but C is also the lightest material with an atomic number of $Z = 6$. With increasing atomic mass (or atomic number Z) also the onset point increases like expected from Eq. 2.4. For Fe it is 78 eV at an atomic number of $Z = 26$ and for W it is the highest with 96 eV with an atomic number of $Z = 74$. The strong dependence of the maximal photon energy E_m^p on the sample material proves that the source of emission can only be fast neutral atoms created at the target surface by surface neutralization. If ions in the sheath would emit the light during the acceleration process due to charge-exchange, the photon emission could not contain any information about the used target material because the emission takes place before the interaction. Furthermore, the energy interval of the red-shifted emission has to be extended to 100 eV for all materials.

Beside this it is tested how good the measurements of the onset energy can describe the formula for the binary collision (Eq. 2.4). The results of this test can be found in Fig. 4.6. The difference between onset energy E_m^p and calculated maximum energy of the reflected atoms E_m is not more than 10% for all the tested materials. Elements with a lower Z number ($Z < 20$) are close to the theoretical curve. For target materials with higher Z numbers ($Z > 20$) the determined data spreads more around the theoretical curve. This can be explained with the fact that for higher Z numbers

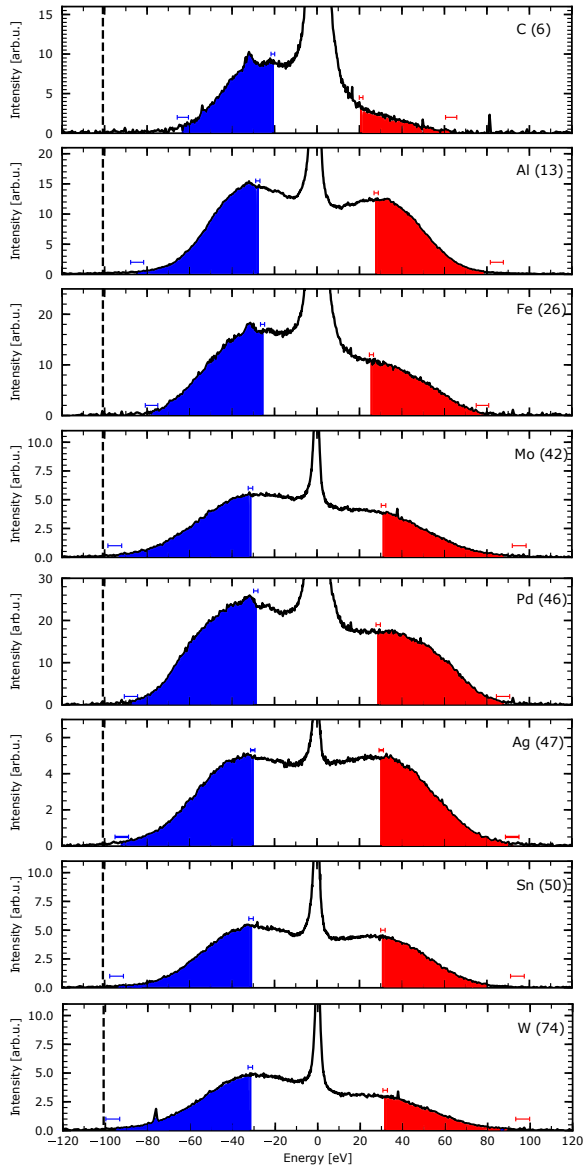


Fig. 4.5: Measured spectra for different target materials. The different energy ranges are shown and the colored areas represent the areas in which the integral for the reflectance is calculated. Blue for the blue-shifted direct emission and red for the red-shifted reflected emission. The error bars are the uncertainties for determine the energy of the spectrum and are the result of the instrumental uncertainty which is ≈ 5 px. The dashed black line represents the applied target potential of -100 V. In the upper right corner of each graph the measured element and in brackets its atomic number is given. All spectra were measured using the radial manipulator except of the measurements of Mo and W. For this spectra the axial manipulator was used.

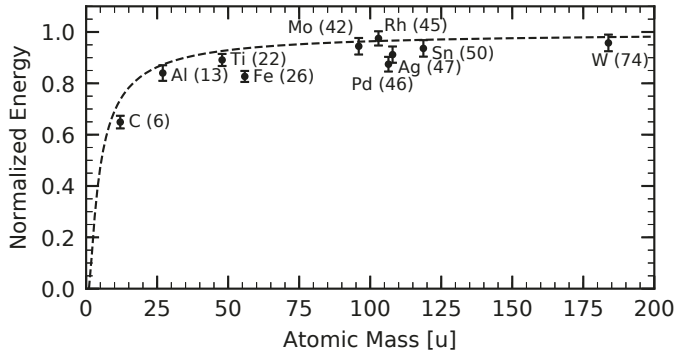


Fig. 4.6: Normalized energy E_m^P/eU_s versus the atomic mass for different target materials, where U_s is the applied target potential. The experimental data is shown in black points and the dashed black curve is the calculation using Eq. 2.4 [AFM07].

the ratio E_m^P/E_m reaches asymptotically one, what makes it more difficult to detect the difference. Another important observation is that the measured value of E_m^P systematically underestimates the theoretical value $E_m^P/E_m \approx 0.8 \dots 0.9$, because neither the plasma potential nor the energy offset δE of 0.12 eV or 10.2 eV is included in this calculations.

To conclude, the onset energy of the Doppler-shifted emission shows a strong dependence on the used sample material (at least for low Z materials) which proves that the detected light is emitted by fast neutral atoms accelerated in the Debye sheath and neutralized and backscattered at the target surface. No emission inside the Debye sheath caused by ions and charge-exchange is measured [Ada03; AKK04], because this signal does not contain any information about the target material. Furthermore, it is proven that the observed red-shifted emission is caused by light reflectance at the metallic surface.

4.4 Development of the Doppler-Shifted Reflectance Measurements (DSRM) Diagnostic

In the last sections it is shown that the emission of incoming ions in the sheath is not the source of the red-shifted component, like proposed in [Phe09; Phe11]. At the used experimental conditions the **source of the red-shifted component is only photon reflection** at the metallic target surface. This fact opens a field for completely novel diagnostics to use the emission of fast atoms in the plasma and to get a deeper insight into plasma-surface interaction. Moreover, this diagnostic can be used to *in situ* determine the optical properties of mirrors during plasma exposition. This diagnostic could be of importance in plasma physics as explained in the following.

Observations by optical spectroscopy are widely used in plasma physics to provide information on electron density n_e , electron temperature T_e , ion density n_i and ion temperature T_i without disturbing the plasma with a probe. Some examples for such a plasma diagnostic would be Charge-exchange Recombination Spectroscopy

(CXRS) [Mer15; Mer19], Motional Stark Effect (MSE) [Rei17], Beam-Emission Spectroscopy (BES) [Del10] or measurements of the Zeeman effect [Mer01]. But a diagnostic is only as good as its components and their accuracy and reliability. One of the components of optical diagnostic are metallic mirrors [Lit07a]. The first mirror of these diagnostics are positioned inside the vacuum chamber and is directly exposed to the plasma. As a consequence these mirrors need to withstand high particles fluxes and radiation which can damage their surfaces [Lit07b] and can change their optical properties, e.g. spectral reflectance and polarization behavior. Beside the plasma also laser pulses can damage these mirrors, depending on the diagnostic using them [KHV08]. Cleaning systems for the first mirror are currently discussed in literature [Mos17a; Mos17b]. Knowledge of the exact spectral reflectance is necessary for example if the absolute intensity of a spectral line should be measured. To do so the transmittance of the complete optical path has to be known, including the first mirror [Dic18a]. If the spectral reflectance changes, also the transmittance changes and the calibration done in advance is not valid anymore. Also the polarization effects of the mirror can be an issue for example for the CXRS diagnostic [Jas08; Mer15]. For the MSE diagnostic the polarization properties of the first mirror are of relevance as well [BA08].

The examples given above demonstrate that it is important to know the exact optical properties of the used mirror in order to run a reliable and precise diagnostic. It would be even better to be able to monitor these values *in situ* during the plasma operation. But until now there is no diagnostic or measurement technique known which is able to measure the optical properties of the first mirrors during the plasma operation. Right now two solutions for recalibration of the first mirror exist. In the first one a calibration source is brought into the vacuum vessel or the first mirror is taken out and is recalibrated outside the plasma chamber, e.g. with ellipsometry (Fig. 4.7) or with an Ulbricht sphere (Fig. 4.8). An ellipsometer is used to determine the dielectric material constants, by scanning the sample surface with polarized photons [TI06]. With an Ulbricht sphere the spectral reflectance of a sample can be measured by measuring first the emission of the Ulbricht sphere and after this the reflected emission of the Ulbricht sphere from the sample surface (Fig. 4.8 (b)). The second approach is to measure the optical properties during the plasma exposition using another external source, e. g. a laser [Miy16]. For the laser an additional optical access to the mirror is needed, but the number of optical ports is highly limited [Kri18]. Thus, a diagnostic is desired, which is able to measure the optical properties of the mirror without disturbing the plasma, without any additional calibration source and without an additional optical port. This kind of diagnostic is not only interesting for fusion research [Mos17a], but also for technological [Mas05] and laser produced plasmas [Lay95].

In this thesis I propose to use the Doppler-shifted emission of fast atoms in a low density H-Ar mixed plasma to measure the optical properties of metallic mirrors during the plasma operation. The basic idea is to transfer the time resolved measurement of the reflectance in the laboratory to an energy resolved measurement in the plasma. The **Doppler-Shifted Reflectance Measurement (DSRM)** diagnostic uses the Doppler-shifted line emission of the Balmer series of fast H atoms to measure the optical properties of metallic mirrors in the plasma as shown in Fig. 4.9. An atom at rest with a velocity $v = 0$ emits light spontaneously with wavelength λ_0 . If the atom is in motion ($v > 0$) the emitted light can be observed either blue-shifted λ_b

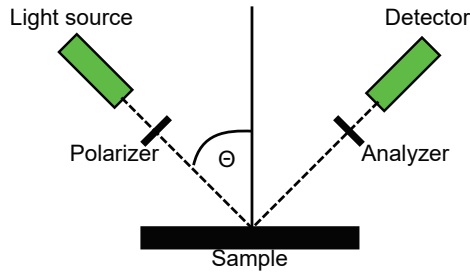


Fig. 4.7: Scheme of an ellipsometry setup. Emission from the light source is polarized with a polarizer and sent onto the sample surface. Afterwards the polarized light is reflected from the sample surface, analyzed in a second polarizer and measured with a detector.

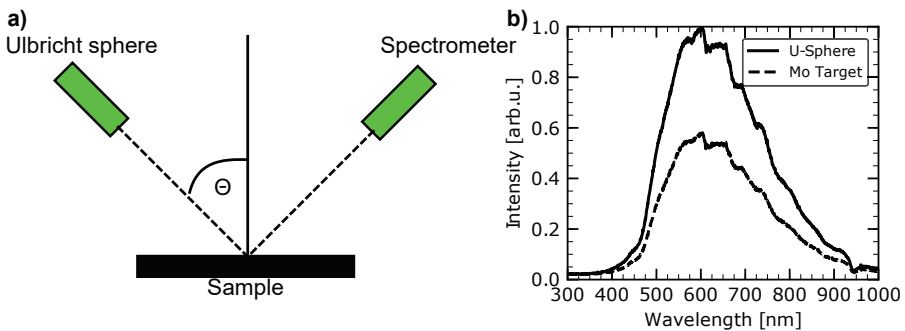


Fig. 4.8: (a) Setup to measure the spectral reflectance of a target with an Ulbricht sphere. (b) Spectra measured with (black dashed curve) and without target (black solid curve). The difference between both spectra is defined as the spectral reflectance of the sample.

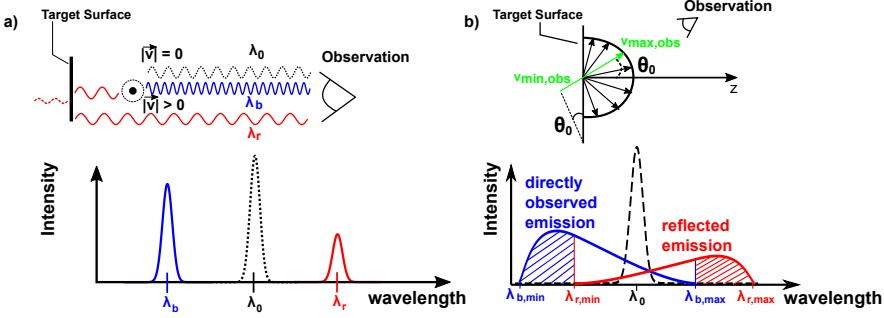


Fig. 4.9: (a) *Top: Scheme of the Doppler-shifted emission of a mono-energetic atom with velocity v moving in the detector direction. Bottom: Measured Doppler-shifted spectrum (blue and red peak). The black dashed line is the emission at a velocity $v = 0$.* (b). *Top: Geometrical conditions at an observation angle of Θ_0 . Bottom: Emission profile of the Doppler-shifted emission. The blue-shifted emission profile is in the interval of $[\lambda_{b,min}, \lambda_{b,max}]$ and the red-shifted emission $[\lambda_{r,min}, \lambda_{r,max}]$. The two emission profiles are overlapping depending on the observation angle Θ_0 . The shape is determined by the angular and energy distribution function of the fast atoms [EB83]. (Image taken from [Dic18a])*

or red-shifted λ_r with regard to the unshifted wavelength λ_0 (Fig. 4.9 (a), top). In the spectrum an emission line with unshifted wavelength λ_0 (black) is observed and separated from this line a blue-shifted λ_b (blue) and the red-shifted λ_r emission line (red) (Fig. 4.9 (a), bottom). The relative intensity of the red-shifted component with regard to the blue-shifted one is smaller, because the red-shift light is interacting with the mirror surface before it is detected in the spectrometer (see Fig. 4.9 (a), top). Using this fact, one can define the reflectance $R = I_r/I_b$ of the mirror surface as the ratio of the blue-shifted I_b and red-shifted component I_r . This can be done, because the source of emission for both emission lines is the same, but one can be observed directly and the other one after the interaction with the mirror surface. This is of course a very simple picture of the working principle of this diagnostic. A more realistic picture of the emission of fast atoms in the plasma is shown in Fig. 4.9 (b), bottom.

4.4.1 Calculation of Reflectance

At the experimental conditions used in this thesis, photon emission by accelerated ions and emission inside the Debye sheath are excluded. The blue-shifted light is emitted directly in the observation direction, whereas the red-shifted light is emitted in the opposite direction. The red-shifted component is only observable, if the light is reflected from metallic surface in the observation direction. Because the red-shifted photon is interacting with target surface before the detection and the blue-shifted photon does not, it is possible to define the ratio of the integrated signals over the blue (I_b) and red-shifted (I_r) emission peak as the spectral reflectance of the investigated sample:

$$R(\lambda_0) = \frac{\int_{\lambda_{b,max}}^{\lambda_{r,max}} I_r(\lambda) d\lambda}{\int_{\lambda_{b,min}}^{\lambda_{r,min}} I_b(\lambda) d\lambda}. \quad (4.3)$$

The integration range is chosen like this, to integrate only over the pure blue and red-shifted signal and not over the overlapping part. The integration range marked shaded in Fig. 4.9 (b), bottom. For the blue-shifted signal the integration area is $[E_{b,min}, E_{r,min}]$ and for the red-shifted signal $[E_{b,max}, E_{r,max}]$. The integration is done numerically using the trapezoidal method. This gives an error σ_b and σ_r on each of the integrals I_b and I_r [CN03]. The total error of the reflectance σ_R is then calculated using Gaussian error propagation:

$$\sigma_R = \sqrt{\left(\frac{I_r \sigma_b}{I_b^2}\right)^2 + \left(\frac{\sigma_r}{I_b}\right)^2} \quad (4.4)$$

According to [Dem06] the reflectance of a surface can also be theoretically calculated using the complex refractive index (Eq. 4.5):

$$\mathbf{n} = n + i\kappa, \quad (4.5)$$

where n is the refractive index and κ the absorption coefficient of the material. For dielectric materials the absorption coefficient is usually zero, e.g. for water $\kappa = 1.64 \times 10^{-8}$ at 650 nm [HQ73]. This results in a low reflectance value of dielectric materials ($R = 0.02$ for water at an incident angle of 0°). However, conducting materials, e.g. metals, have a large absorption coefficient and thus high reflectance value, e.g. for Ag $\kappa = 4.22$ at 656 nm and a reflectance of $R = 0.96$ at an incident angle of 0° .

The refractive index is needed if the interaction of light and a medium should be investigated. In the following, the light is described as a planar wave. To understand how the reflection and polarization of light wave works, one needs to look at the interaction between the electro-magnetic wave moving from a medium with refractive index n_1 to the surface of certain material with refractive index $n_2 > n_1$ (Fig. 4.10). The vector of the incoming wave is described with \mathbf{k}_e . The area between the incoming wave vector \mathbf{k}_e and the normal of the surface \mathbf{N} is called the plane of incidence. If the wave interacts with the surface of a material, the incoming wave can be either reflected (with wave vector \mathbf{k}_r) or refracted (with wave vector \mathbf{k}_f). All three waves can be explained as plane waves like mentioned above (Eqs. 4.6 to 4.8):

$$\mathbf{E}_e = \mathbf{A}_e \cdot \exp[i(\omega_e t - \mathbf{k}_e \cdot \mathbf{r})], \quad (4.6)$$

$$\mathbf{E}_r = \mathbf{A}_r \cdot \exp[i(\omega_r t - \mathbf{k}_r \cdot \mathbf{r})], \quad (4.7)$$

$$\mathbf{E}_f = \mathbf{A}_f \cdot \exp[i(\omega_f t - \mathbf{k}_f \cdot \mathbf{r})], \quad (4.8)$$

where \mathbf{A}_i is the amplitude, ω_i is the frequency and \mathbf{k}_i is the wave vector of the wave. As a consequence of the maxwell equations the tangential component \mathbf{E}_t of the waves relative to the surface have to be continuously:

$$E_{et} + E_{rt} = E_{ft} \quad (4.9)$$

Using this equation one finds that the frequency of all waves need to be the same and result in a relation for the phase velocity ν_{ph} of the wave if the light is moving from medium 1 into medium 2:

$$\nu_{ph} = c' = \frac{c}{n} = \frac{\omega \lambda}{2\pi}, \quad (4.10)$$

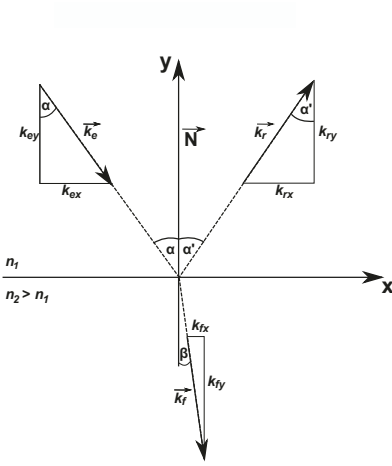


Fig. 4.10: Scheme of the reflection and transmission of an incoming wave with the wave vector \mathbf{k}_e , the reflected wave has the wave vector \mathbf{k}_r and the transmitted wave \mathbf{k}_f . The angles are measured from the surface normal \mathbf{N} . The incoming angle is named α , the reflectance angle α' and the transmittance angle β . The refractive index of first material is n_1 and of the second material $n_2 > n_1$.

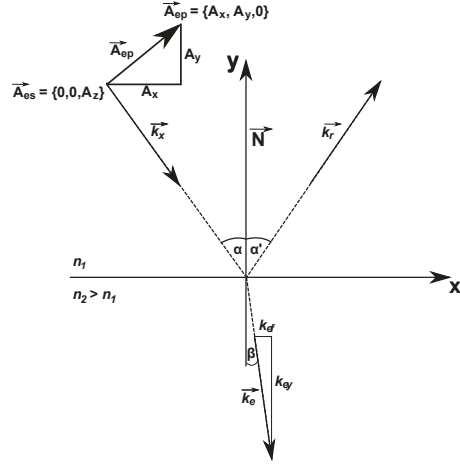


Fig. 4.11: Geometrical condition to derive the Fresnel formulas to calculate the reflectance of the surfaces.

where c is the velocity of light in vacuum and λ is the wavelength of the wave. Eq. 4.10 means that if light is penetrating from one material into another with different refractive indices, the frequency of the wave stays constant but the wavelength changes. Taking Eq. 4.9 and Eq. 4.10 into account the Snell's law of refraction can be derived:

$$\frac{\sin(\alpha)}{\sin(\beta)} = \frac{c'_1}{c'_2} = \frac{n_2}{n_1} \quad (4.11)$$

To calculate the reflectance and the polarization of the reflected wave one needs to take a closer look to the amplitude \mathbf{A}_i of the three waves. Similar to the tangential and perpendicular component of the wave with regard to the surface, the same definition can be made for the amplitude with regard to the plane of incidence. Thus, the amplitude is separated in a component perpendicular A_s and one component parallel A_p to the plane of incidence. The tangential component again needs to be continuously:

$$A_{et} + A_{rt} = A_{ft} \quad (4.12)$$

The geometrical conditions of the amplitude vector is shown in Fig. 4.11. Using $\mathbf{B} \approx (\mathbf{k} \times \mathbf{E})$ and Eq. 4.12 for non ferromagnetic materials (magnetic permeability $\mu \approx 1$) one gets:

$$(\mathbf{k}_e \times \mathbf{E}_e)_x + (\mathbf{k}_r \times \mathbf{E}_r)_x = (\mathbf{k}_f \times \mathbf{E}_f)_x \quad (4.13)$$

Using Eqs. 4.11, 4.12 and 4.13 the reflection coefficient ρ_s and the transmission coefficient τ_s perpendicular to the plane of incidence and ρ_p and τ_p for the component

parallel to the plane of incidence can be calculated:

$$\rho_s = \frac{A_{rs}}{A_{es}} = \frac{n_1 \cos \alpha - n_2 \cos \beta}{n_1 \cos \alpha + n_2 \cos \beta}, \quad (4.14)$$

$$\tau_s = \frac{A_{fs}}{A_{es}} = \frac{2n_1 \cos \alpha}{n_1 \cos \alpha + n_2 \cos \beta}, \quad (4.15)$$

$$\rho_p = \frac{A_{rp}}{A_{ep}} = \frac{n_2 \cos \alpha - n_1 \cos \beta}{n_2 \cos \alpha + n_1 \cos \beta}, \quad (4.16)$$

$$\tau_p = \frac{A_{fp}}{A_{es}} = \frac{2n_1 \cos \alpha}{n_2 \cos \alpha + n_1 \cos \beta}, \quad (4.17)$$

Eqs. 4.14 - 4.17 are called Fresnel equations and are the basis for any further calculation of the reflectance or the polarization of the reflected light at the interface of two materials with refractive index n_1 and n_2 . The s-polarized reflectance is defined as $R_s(\alpha, \beta, n_1, n_2) = \rho_s^2$ (Eq. 4.18) and $R_p(\alpha, \beta, n_1, n_2) = \rho_p^2$ (Eq. 4.18) for the p-polarized reflectance and the total reflectance R can be calculated out of R_s and R_p using Eq. 4.20.

$$R_s(\alpha, \beta, n_1, n_2) = \rho_s^2 = \left(\frac{A_{rs}}{A_{es}} \right)^2, \quad (4.18)$$

$$R_p(\alpha, \beta, n_1, n_2) = \rho_p^2 = \left(\frac{A_{rp}}{A_{ep}} \right)^2, \quad (4.19)$$

$$R = \frac{R_s + R_p}{2}, \quad (4.20)$$

In Eq. 4.16 one can see that the reflection coefficient decreases to zero $\rho_p = 0$ if the condition $\alpha + \beta = 90^\circ$ is fulfilled. The angle $\alpha = \alpha_B$ which fulfills the condition ($\alpha + \beta = 90^\circ$) is called Brewster angle. At the Brewster angle the parallel component of the reflection $R_P = 0$ and the Brewster angle is calculated using Eq. 4.21:

$$\tan(\alpha_B) = \frac{n_2}{n_1} \quad (4.21)$$

This can also be understood using a simple picture. The incoming wave excited the electrons at the interface to oscillate along the electronic field vector \mathbf{E} inside the material with refractive index n_2 . Then the electrons emit dipole radiation. At the Brewster angle the reflected wave vector is parallel to the dipole axis. But dipoles do not emit radiation parallel to the dipole axis and thus the parallel component of the reflectance R_P is zero [Dem06].

The measurement of the polarization of the reflected light cannot only be used to measure the polarization properties of the mirror, but also to detected changes in the surface morphology. The light is polarized if the angle of incidence is the Brewster angle, like shown in Fig. 4.12 (a). The assumption in this picture is that an ideal mirror has only one plain of incidence. In Fig. 4.12 (b) the situation is completely different. The mirror surface is now assumed to be totally diffusive, which results in many plains of incidence. Thus, every microsurface has a different orientation towards the normal of the macrostructure. The result is the loss of a preferable direction of polarization, because the orientation of the dipoles, induced at the surface by the incoming EM-wave, is different for all plains of incidence. As a consequence, the reflected light is not polarized anymore.

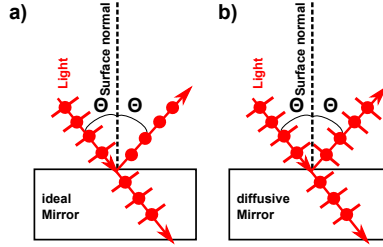


Fig. 4.12: Schematic picture of the polarization of reflected light at an ideal mirror (a) and a completely diffusive mirror (b). (a) If the surface is an ideal mirror, the light is polarized if the angle of incidence is the Brewster angle α_B . The theory of polarization by reflectance assumes only one plain of incidence and thus only one direction of dipole radiation. (b) The assumption of only one plain of incidence is not applied for a diffusive surface. In this picture the surface consists of many plains of incidence. As a result no preferable direction of polarization exists anymore and thus the reflected light is unpolarized.

4.5 Determination of the Spectral Reflectance for Various Mirror Materials

In this section the spectral reflectance is determined for various mirror materials namely: Ag, Al, C, Cu, Fe, Mo, Pd, Rh, Sn, Ti and W. The reflectance is calculated as explained in Sec. 4.4.1. The integral is calculated in the range $[-E_m^p : -E_{min}^p]$ for the blue-shifted component and $[E_{min}^p : E_m^p]$ for the red-shifted component using the trapezium rule. In Sec. 4.3 it can be found how this intervals are determined. The reflectance is defined as the ratio of red and blue-shifted emission $R = \int d\lambda I_r(\lambda) / \int d\lambda I_b(\lambda)$ (Eq. 4.3). The error on the reflectance is calculated out of the error for the calculated integral using Gaussian error propagation (Eq. 4.4). In Fig. 4.13 the results of the reflectance measurements are shown. The reflectance values are determined at the following surface potentials: $U_s = -80$ V for Fe and Pd, $U_s = -100$ V for Ag, Al, Mo, Sn and W, $U_s = -120$ V for C and Cu, $U_s = -140$ V for Rh and $U_s = -180$ V for Ti. For all 11 materials the difference between measured reflectance and the values taken from literature is at maximum 15 %. This is the first time a diagnostic is able to do this kind of measurement [Bra17; Mar18; Dic18a] and it proves that the ratio of blue and red-shifted components can be used to determine *in situ* the spectral reflectance of a metallic mirror. Nevertheless, for C the difference between measured reflectance and literature value is large. The difference can be explained with the low reflectance of C (≈ 0.2) which makes it difficult to gain a strong red-shifted emission signal. But also the literature values may need to be discussed. For e.g. W the DSRM diagnostic measured a larger value compared to literature which is also observed by the group of *Minissale et al.* in their recent publication [Min17]. The DSRM diagnostic determines a reflectance of 0.59 for W, *Werner et al.* 0.53, *Rakić et al.* 0.50. Thus, the difference is 10 % and 15 %, respectively. *Minissale et al.* achieve of a value of 0.55, which makes a difference of 7 % compared to the results of the DSRM diagnostic in this thesis. Note that for the red points in Fig. 4.13 the spectral reflectance is measured in the lab with an Ulbricht sphere before the plasma exposure. The determination of the spectral reflectance

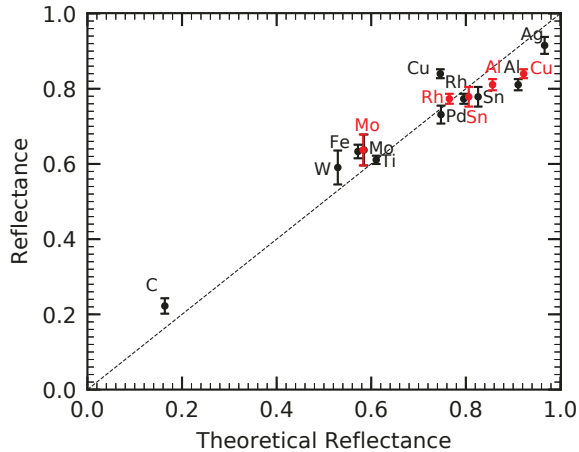


Fig. 4.13: Experimental reflectance compared to values taken from the literature. The values for Ag, Fe, Pd, W, Mo, Ti and Cu are taken from [WGA09], C data taken from [Que85], Al data taken from [Rak98], Rh data from [WOL77] and Sn data taken from [GM64]. It should be noted that there is no literature value for Sn available at the wavelength of 656 nm. The value given in this plot is taken for 730 nm. The error bars for the reflectance data is calculated using Eq. 4.4. For the red points the spectral reflectance of the mirror is measured in the lab with an Ulbricht sphere before plasma exposure.

using an Ulbricht sphere is schematically shown in Fig. 4.8. The difference between the measurements in the lab and the experimental results obtained by the DSRM diagnostic is around 3% smaller compared to the values taken from literature. Thus, it seems that it is quite difficult to achieve reflectance values for metallic mirrors and that different experiments could result in different values. Thus, the DSRM can be another important tool to test the spectral reflectance of metallic mirrors, to verify them and add these values to the databases which is demonstrated by the measurements in Fig. 4.13 very clearly. This is not only interesting for fusion devices [Lit07b; KHV08; Kra15], but for plasma physics and optics in general where metallic mirrors are used in the experimental setup [Ors01].

4.6 Time Stability and Voltage Dependence of the Reflectance

A very important property of a diagnostic is its time stability, since the results should be reproducible at any time under the same conditions. As a consequence, this property needs to be proven for the DSRM diagnostic as well. To do so, two scenarios need to be tested. First, the diagnostic uses a H-Ar mixed plasma to measure the spectral reflectance of the mirror, but the plasma itself should not change or influence the spectral reflectance or the mirror surface. Second, it needs to be shown that the determination of the spectral reflectance is independent on the applied surface potential.

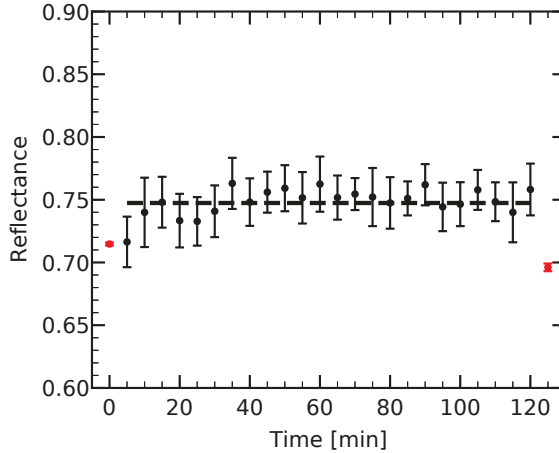


Fig. 4.14: Temporal evolution of the experimental determined reflectance of a Pd mirror during 2 h. The gas flux was adjusted to 80 : 80 sccm, the surface potential was -100 V and the radial manipulator was used to make this experiment. The red data points at the beginning and the end are reflectance measurements before and after plasma exposure outside the vacuum chamber using an Ulbricht sphere. The dashed line is the reflectance taking from Werner et al. [WGA09].

To check the first point a Pd mirror was exposed to a H-Ar plasma with a gas flux of 80 : 80 sccm and a surface potential of $U_s = -100$ V. Fig. 4.14 shows the measured reflectance versus time. The red data points at the beginning and the end of the measurement are measured in the lab using an Ulbricht sphere. The reflectance is determined out of a spectra measured with an exposure time of the EMCCD chip of 300 s, thus every five minutes one reflectance value is obtained. The long exposure time is used to have good statistic and signal-to-noise ratio in the spectrum. The dashed horizontal line is the literature value taken from [WGA09]. The measured reflectance value stays constant within in the error bars over 2 h and agrees well with the two measurement done in the lab before and after plasma exposure, the variation is only in the range of 1 % to 2 %. This measurement clearly demonstrates that the Ar flow do not change the optical property of the mirror surface and the measurement technique of the DSRM diagnostic is reliable and time stable.

In the second test the target potential is varied and the reflectance is measured at each potential. Again one spectrum is obtained in five minutes. The gas flow for this experiments was 40 : 40 sccm. The potential stability is tested for three mirror materials Pd, Fe and C. The target potential was varied between $U_s = -80$ V to $U_s = -220$ V. The measurements were started at -80 V and the potential is increased to its maximum in steps of $U_s = -20$ V. For each target potential the spectrum is measured with an integration time of 5 min and the reflectance is calculated. The determined reflectance values are compared with the values taken from literature as shown in Fig. 4.15. The literature values are depicted as dashed lines and taken from [WGA09] for Pd and Fe and from [Que85] for C. For Pd and Fe the measured reflectance seems to be only weak depended on the applied potential. Within the 1σ range the reflectance stays close to the literature values of 0.57 for Fe and 0.74 for

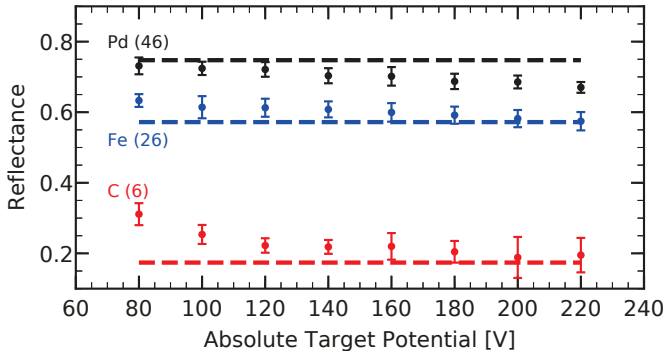


Fig. 4.15: Measurement of the spectral reflectance for a Pd, Fe and C mirror at different surface potentials. The measurements started at $U_s = -80$ V and the potential was increased to $U_s = -220$ V. The dashed line are the reflectance values taken from literature. For Pd and Fe the values were taken from Werner et al. [WGA09] and for C from Query [Que85]. (Image taken from [Dic18a])

Pd. A reduction of the measured reflectance is in the order of 5%. The reduction can be explained with a destruction of the mirror surface with a higher energy of Ar^+ ions at higher surface potentials. For C the reflectance is 0.31 at the beginning, which is a difference of 45% compared to the literature value of 0.17 [Que85]. The reason is the low reflectance of C which results in a bad statistic in the red-shifted component at -80 V, which also can be seen in Fig. 4.4. This makes it difficult to derive the spectral reflectance out of the spectrum. At higher target potentials the integration area and thus the statistic increases and the measured reflectance comes closer to the literature value. At -180 V the difference is only 15% and the literature value is in the 1σ range. For even higher target potentials the differences decrease to less than 5%.

To summarize the observations of the first part of this section one can conclude that the DSRM diagnostic is stable in time and the measurement procedure does not change the spectral reflectance of the mirror if the potential is small enough to avoid sputtering of the mirror surface by high energetic Ar^+ ions. As can be seen in Fig. 4.15 the reflectance slightly decreases for higher target potentials in case of Fe and Pd. C in this case can be left out, due to the given reasons. Thus, a good working potential of the DSRM diagnostic should be in the range of -100 V, where the energy of the Ar^+ is not high enough to damage the mirror surface in a reasonable amount of time (2 h) in the case of Pd (Fig. 4.14). For materials with a lower Z than Pd the sputtering is faster, because of the lower mass, for materials with a higher Z number the sputtering is slower. Because the Z number of Pd is near the middle of the used materials, in this thesis, the long term test was performed with Pd as mirror material. Thus, -100 V target potential should be a good compromise for all used materials in this thesis (except of C).

Beside the potential dependence of the reflectance also the potential dependence of the blue-shifted integral I_b is analyzed to learn more about the emission process itself. The blue-shifted integral can be estimated using the following equation [Dic18a]:

$$I_b \approx (N_+ R_N) N_{\text{Ar}, \text{Ar}^*} \langle \sigma(E_0) \sqrt{E_0} \rangle \text{ for } (U_s \gg U_p), \quad (4.22)$$

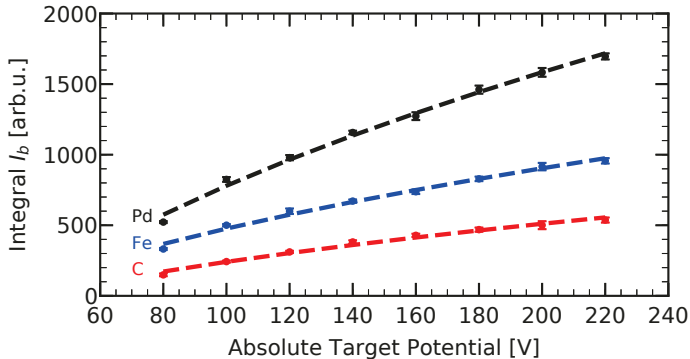


Fig. 4.16: Integral I_b of the blue-shifted component is plotted versus the applied potential. For this experiment Pd, Fe, and a C mirror was used and the target potential was started at -80 V and then increased in steps of -20 V to -220 V. The dashed line is the fitted function $I_b = a + b\sqrt{eU_s}$ to the data, where a and b are fitting coefficients, e the elementary charge and U_s the applied surface potential. The fitting function assumes the relation of Eq. 4.22. (Image taken from [Dic18a])

where N_+ is the ion density of H ions, R_N is the particle reflection coefficient for H, N_{Ar,Ar^*} is the density of Ar in ground state or Ar metastable [Mar18] and $\langle\sigma(E_0)\sqrt{E_0}\rangle$ is the rate coefficient of excitation. In Fig. 4.16 the blue-shifted integral is fitted using the function $I_b = a + b\sqrt{eU}$, which assumes that the Eq. 4.22 is correct. A very good agreement between fitting function and experimental data points is achieved. Thus, the variation in the surface potential changes the rate coefficient $\langle\sigma(E_0)\sqrt{E_0}\rangle$ and as a consequence also the Doppler-shifted emission. This demonstrates again very clearly that the emission measured by the DSRM diagnostic is only emitted by fast atoms produced at the mirror surface after the neutralization of the accelerated ions at the surface. Furthermore, it explains the observation in Figs. 4.2, 4.3 and 4.4 that the Doppler-shifted emission can be switched on and off by only varying the target potential. If no electrostatic potential is applied to the mirror, no Doppler-shifted emission will be detectable [Dic18a].

4.7 Spectral Reflectance Measurements at H_β

Beside the H_α spectral line, also the H_β line is tested. The H_α line is an important line for many diagnostics like for MSE measurements [Rei17], BES experiments [Del10] or measurement of the Zeeman effect. All these diagnostics are using the wavelength of the H_α line. Nevertheless, the following experiment should demonstrate that the DSRM diagnostic is not restricted to the wavelength of 656 nm, but also other wavelengths can be used. The H_β line at a wavelength of 486 nm is used because its only 18 nm away from the He II line at 468 nm. This line is of relevance for the CXRS diagnostic which should be built up at ITER to measure the density of the helium ash in the fusion reactor [Hel05; Jas08; Jas12]. Assuming that the spectral reflectance does not change considerably in the range between 468 nm and 486 nm, the DSRM diagnostic potentially can be used to solve the calibration problem of the

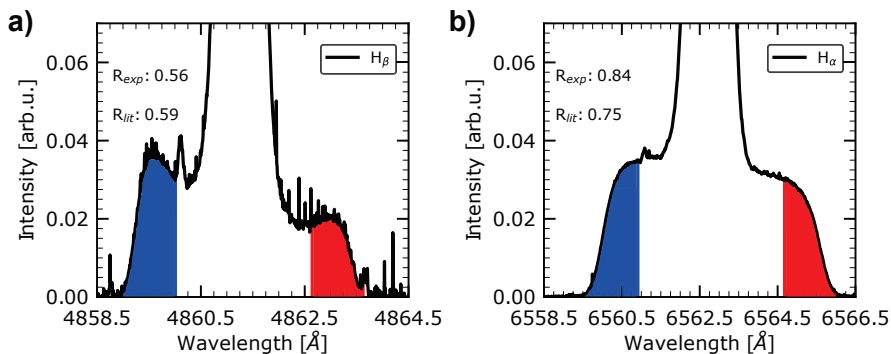


Fig. 4.17: Measured spectra of a Cu mirror in H-Ar mixed plasma with a gas flux of 40 : 40 sccm. The surface potential for both measurements was $U_s = -120$ V. Both spectra are normalized to the maximum of the passive Balmer line. (a) Spectra measured for the H_β line at 486 nm. The reflectance is calculated in the colored areas. Blue for the blue-shifted component and red for the red-shifted component. (b) Spectra measured using the same Cu mirror at the position of the H_α line at 656 nm. The literature values of the reflectance of Cu are taken from Werner et al [WGA09].

CXRS setup. The most promising material for the CXRS first mirror at the moment is Rh [Mer15; Mer19]. Using the Fresnel equations (Sec. 4.11) and the data given by [WOL77; Pal98] one can calculate the reflectance of Rh to 0.740 for 468 nm and 0.743 for 486 nm. Thus, by calibrating the Rh mirror at the H_β line one could also calibrate the He II line emission ($n = 4 \rightarrow n = 3$) of the CXRS diagnostics. It needs to be noted that all reflectances are calculated at an observation angle of 35° .

The H_β line is shown on the example of Cu. The reflectance of Cu at H_α is $R = 0.75$ and for H_β it is $R = 0.59$, thus the difference between both is 20% which allows to cross check the reflectance measurement of the same Cu mirror using both wavelengths (Fig. 4.17). The gas flux of H and Ar for this experiment was adjusted to 40 : 40 sccm and the surface potential was $U_s = -120$ V. For both measurements the reflectance is calculated using the colored areas in the spectrum. The blue color is the integral area for the blue-shifted component and the red-shifted area is integrated in the red colored area, similar to Fig. 4.5. The reflectance at H_α is determined to 0.84. The difference to the literature value of 0.75 [WGA09] is 11% and thus inside the accuracy of the DSRM diagnostic. For H_β the result is even better with 0.56 compared to the 0.59 in the literature [WGA09]. Here the difference is only 5%. Note that the reflectance value for H_α in literature can vary strongly from 0.75 [WGA09] to 0.97 (for Cu thin films) [McP15] compared to H_β where the difference is much smaller 0.59 [WGA09] to 0.61 [McP15]. This proves that the DSRM diagnostic is also able to measure the reflectance at other wavelengths as in the case of 486 nm. For the CXRS diagnostic at ITER the DSRM diagnostic could be a promising candidate to measure *in situ* the reflectance of the first mirror near the He II line.

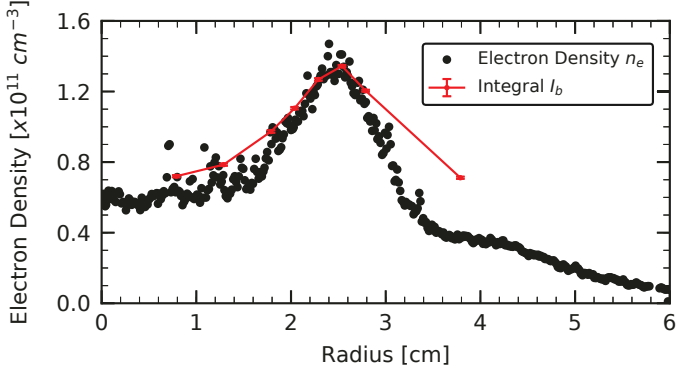


Fig. 4.18: Radial profile scan of a standard H-Ar mixed plasma with a gas flux of 40 : 40 sccm combined with a Langmuir probe measurement of the same plasma. A Pd mirror with an applied potential of $U_s = -100$ V was used. The black dots show the measured electron density n_e using a Langmuir probe. The red data points are the measured integral of the blue-shifted component. The measured profiles of the DSRM diagnostic and the Langmuir probe are aligned at their maxima.

4.8 Measurement of the Plasma Profile using the Emission of Fast Atoms

Taking a closer look to Eq. 4.22 one can see that the integral of the blue-shifted component should also be sensitive to a change of the electron density n_e , assuming that electron and ion density have the same profile in PSI-2. The intensity of the shown signal of the electron density in the PSI-2 device is a hollow one [KF04; Kre15] (Fig. 4.1). Due to the quasi-neutrality of the plasma the ion profile of H ions can be assumed to be similar to the electron density profile and the DSRM diagnostic should be able to measure the profile of the PSI-2 plasma as well. Assuming a spherically symmetric plasma profile, the only difference in the measurement with a Langmuir probe and the DSRM diagnostic is that the DSRM diagnostic measures in y direction, whereas the Langmuir probe measures in z direction (for a explanation of the directions see Fig. 3.1). As a consequence, the intensity of the blue-shifted emission should be proportional to the electron density. Note that the Langmuir probe measures the plasma approx. 0.5 m in front of the manipulator (see Fig. 3.1).

In Fig. 4.18 the measured integral of the blue-shifted component I_b is depicted (red dots) combined with a Langmuir probe measurement (black dots). For the measurements a Pd mirror is used and a potential of $U_s = -100$ V was applied. The plasma was a H-Ar mixed plasma with a gas flux of 40 : 40 sccm. One can clearly see that the DSRM diagnostic also measures a hollow structure of the plasma. Both profiles (black and red) are normalized to each other at their maxima. The fact that the measured signals are in very good agreement proves that the signal of the atoms is only linearly proportional to the electron density. Unfortunately only the data for one point at 3.9 cm outside the region is available and for this point the emission reduces only by a factor of 2 compared to the electron density. The latter drops by a factor of 4. There are few possible explanations of such behavior at the edge. First,

due to the low temperature the fraction of H ions increases at the edge compared to the Ar ions because of the higher ionization potential of the second one. Second, the plasma potential could be dropped to zero. In this case the kinetic energy of the ions will be increased and as a result the emission rate could be higher. At the same time the particle reflection coefficient $R_n(E)$ could be increased too. More detailed investigations at different materials and a few potentials are required to investigate the emission as a function of electron density also at the edge of the PSI-2 plasma. Nevertheless, this measurement is a prove that the assumptions made in Eq. 4.22 are correct as well as the fact that the ions and electrons need to have a similar density profile.

To conclude, the experiments have not only proven that the assumptions made in Eq. 4.22 are correct but have also shown another application of the DSRM diagnostic. Knowing all the other variables in Eq. 4.22 except of the ion density of H, the DSRM diagnostic can be used to measure the absolute ion density of the plasma like shown in Fig. 4.18. But up to now it is only possible to measure a relative change in the ion density but no absolute values.

4.9 Polarization of Light by Reflectance at the Mirror Surface

An unexplored application of the DSRM diagnostic is the measurement of polarization by light reflection at target surfaces. Indeed, until now the plasma polarization spectroscopy focuses only on polarization by electrical or magnetic fields (Zeeman effect [Rei17] and Stark effect [BA08]) or due to spatial anisotropy of the plasma [Fuj99]. Measurements of polarization properties of surfaces exposed to a plasma are not available. But these kind of measurements are highly needed since the polarization of the reflected light can be an issue for some diagnostics, e.g. for the CXRS diagnostics [Mer15]. Due to this reason it is tested if the polarization of the reflected light from the mirror surface can be measured by the DSRM diagnostic. The situation of the experimental setup used in this thesis is depicted in Fig. 4.19. The excited H atom is shown as a yellow sphere moving with velocity \mathbf{v} away from the mirror surface. On the scale of the life time of the excited state τ the atom emits a photon. The emitted light is not polarized, thus the observed blue-shifted component should show no polarization. The red-shifted component, interacting with mirror surface before the detection, is polarized according to the Fresnel equations 4.18 and 4.19. The difference in s and p-polarization is the largest at the Brewster angle (Eq. 4.21) and thus the experiments were performed as close to the Brewster angle as possible ($\theta_0 = 75^\circ$). Using the Fresnel equations and the data of *Werner et al.* [WGA09] one can calculate the Brewster angle of Mo to $\alpha_B = 79.9^\circ$ at a wavelength of 656 nm. At the Brewster angle the difference between s and p-polarization is a factor of 7, at 75° it is a factor of 5.5 and at 35° it is 1.2 (see Fig. 4.20 (c)).

In Fig. 4.20 (a) and (b) the polarization of reflected light of a Mo mirror is measured at different line-of-sights, namely at 35° and 75° , which is the highest achievable angle, due to space limitations at the diagnostic port. To measure the polarization a polarizer is put in the optical path before the light is coupled into the fiber. The gas flux for both measurements for the H-Ar mixed plasma was 80 : 80 sccm. For the measurements in Fig. 4.20 (a) a target potential of -100 V was used, for (b)

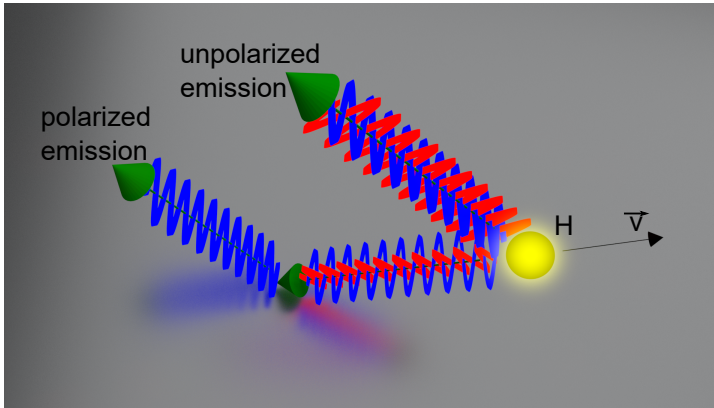


Fig. 4.19: Schematic how the light emitted by fast atoms is polarized at the metallic surface. The two polarization directions s and p are depicted in different colors, blue for s -polarization and red for p -polarization. The light emitted by the excited H atom (yellow sphere) moving with a velocity v away from the mirror surface consists of both polarization directions. At the surface the light is interacting with the mirror surface (this can be calculated using the Fresnel equations Eqs. 4.18 and 4.19). At the Brewster angle only s -polarized light is reflected back from the surface. Image is created and rendered using the software Blender 3D [Ble18].

it was -120 V. For both experiments the axial manipulator was used in order to be able to change the observation angle during the measurement (Sec. 3.2.2). The two spectra are normalized to the blue-shifted component since the direct observed emission should not be polarized, because it is not interacting with the mirror surface. As can be seen in Fig. 4.20 (a) the difference between s and p -polarization is only around a factor of 1.06 at an observation angle of 35° .

After the measurement at 35° the observation angle is changed to 75° in Fig. 4.20 (b). Now a clear difference by a factor of two is observed, which is a difference of around 60% to the expected factor of 5.5. The reason is as follows: at $\theta_0 = 75^\circ$ the overlap of both distributions functions is strong, which is indicated by the colored lines for direct and reflected emission. There is only a small amount of each component which is not disturbed by the other. As a consequence, the observed emission is the sum of the blue-shifted or unpolarized signal and red-shifted or polarized signal. Because of that, the difference between R_S and R_P directly observed from the spectrum is much smaller than the theoretical expectation. Furthermore, it is not possible to measure the reflectance out of the spectrum, because of the small region where the components are not overlapping. These problems will be solved by modeling the distribution functions in Sec. 4.11. To demonstrate that the DSRM diagnostic can also measure the polarization of other mirror materials, a W mirror is tested as well (Fig. 4.21). Comparing Fig. 4.20 (a), (b) and Fig. 4.21 (a) one can conclude that the DSRM is able to measure the polarization of the reflected light quantitatively.

Like explained in Sec. 4.4.1 it is possible to use the measurement of the polarization of reflected light to determine a change in the surface morphology. This is demonstrated in this thesis by measuring the polarization characteristic of a Sn mirror. Sn is used as a mirror material for two reasons. First, it is a light material ($Z = 50$), which

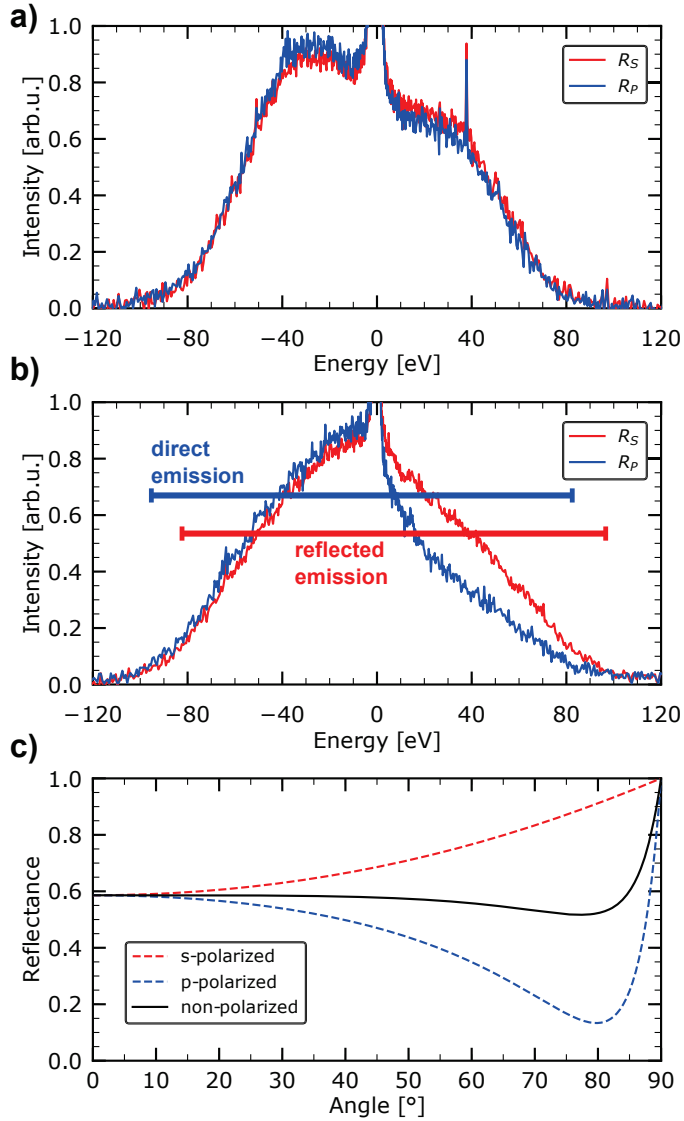


Fig. 4.20: Polarization measurement of a Mo mirror. The applied potential was -100 V for (a) and -120 V for (b). The gas flux was 80 : 80 sccm for the H-Ar mixed plasma and the axial manipulator was used for this experiments. For both experiments a polarization filter was used before the light, emitted in the plasma, is coupled into the fiber to the spectrometer. (a) Measured spectra at an angle of 35° . (b) Measured spectra at an angle of 75° . (c) Theoretical curve calculated using the Fresnel equations (Eqs. 4.18 and 4.19) with the data from Werner et al. [WGA09]. The color code is similar to (a) and (b) and the black curve is the total reflectance $R = (R_s + R_p)/2$.

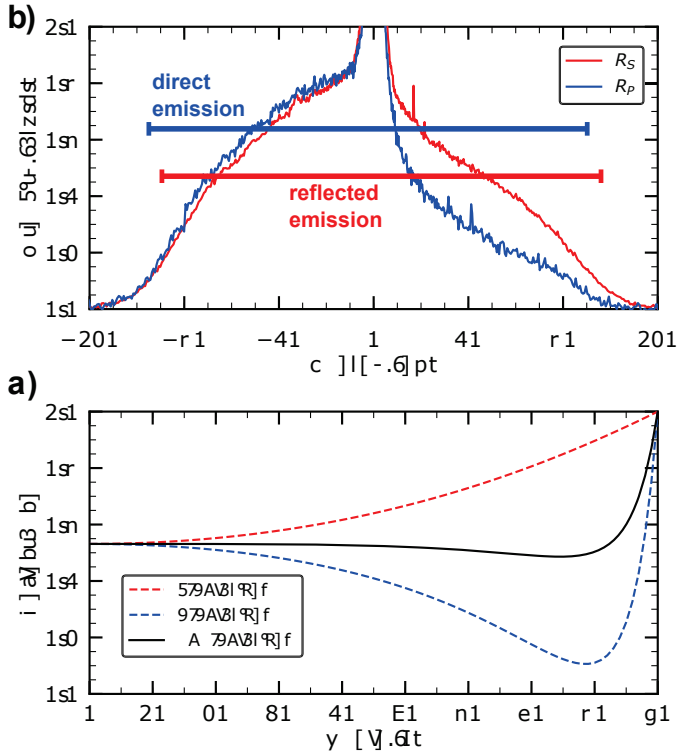


Fig. 4.21: Polarization measurement of a W mirror. The applied target potential was -120 V. The gas flux was adjusted to 40 : 40 sccm for the H-Ar mixed plasma. The axial manipulator was used for the measurements. For both experiments a polarization filter was used before the light, emitted in the plasma, is coupled into the fiber to the spectrometer. (a) Measured spectra at an angle of 70° . S-polarization is depicted in red and p-polarization in blue. (b) Theoretical curve calculated using the Fresnel equations (Eqs. 4.18 and 4.19) with the data from Werner et al. [WGA09]. The color code is similar to (a) and (b) and the black curve is the total reflectance $R = (R_s + R_p)/2$.

makes it easy to sputter with Ar and second it has a low melting point of 232 °C. The low melting point makes it easy to change the surface morphology by temperature [Bal17]. In Fig. 4.22 polarization measurements on the same Sn mirror are shown. In Fig. 4.22 (a) a new Sn mirror was tested. A target potential of $U_s = -120$ V was applied and a gas flux of 80 : 80 sccm of H and Ar was adjusted. For the experiment the axial manipulator was used and the observation angle θ_0 was 75°. Analyzing the spectrum, one can see that the difference between R_S and R_P is a factor of 1.5 for the polished Sn mirror. As can be seen in the upper left corner of Fig. 4.22 (a) the Sn mirror is well polished with a diamond polish paste with a grain size of 0.5 μm . After this measurement the mirror was heated up to around 170 °C and the polarization properties of the same Sn mirror were measured again (Fig. 4.22 (b)). The difference between R_S and R_P is nearly vanished. In the upper left corner one can see that the mirror surface is degenerated and diffusive in comparison to the surface before the treatment, which results in the loss of polarization.

To conclude, the DSRM diagnostic is able to measure the polarization of the reflected light of several mirror materials, namely Mo (Fig. 4.20), W (Fig. 4.21) and Sn (Fig. 4.22). Note that detailed studies of the morphology by SEM or XPS or its modification was not performed during this thesis. The main aim was to prove that measurements of the polarization are feasible at all.

4.10 Temperature Dependence of the Spectral Reflectance

The Sn mirror in the previous section was heated up in order to destroy the mirror surface and change the polarization properties. In this section an Al is heated up and the spectral reflectance of the surface is measured *in situ* during the heating process. The spectral reflectance of a surface depends on the surface temperature, because the plasma frequency and the electron-phonon collision frequency and thus the index of refraction are temperature depended [Uji72]. In 1972 Kikuo Ujihara has developed a model based on the Drude theory and the theory of electron-phonon scattering. In his calculation he predicts a reduction of the spectral reflectance for different metals. In Fig. 4.23 his data were digitized using the plot in his paper and is replotted. One can see that the change of reflection is the largest for Al with 20 – 30 %. For the experiments in this thesis Al is chosen as testing material, due to the following reasons: First, it is frequently used in the experiments. Second, it is described by the theory of K. Ujihara and the obtained experimental data can be cross checked with the theory. Third, the change of reflection is the highest for Al and fourth Al has a the lowest melting temperature of all investigated metals by K. Ujihara. The melting temperature is important, since only a passive heating by the plasma is available in the used experimental setup.

At first the Al mirror is mounted onto the radial manipulator and exposed to the H-Ar mixed plasma with a gas flux of 40 : 40 sccm. The mirror was cooled during the experiment holding its temperature constant at around 300 K. A potential of $U_s = -100$ V is applied and the reflectance is measured each minute for 1 h. In Fig. 4.24 (a) the first spectra (black dashed curve) and the last measured spectra after 1 h of plasma exposition (blue solid curve) are shown. Comparing both spectra one can see that there is only a small difference between both curves and the reflectance

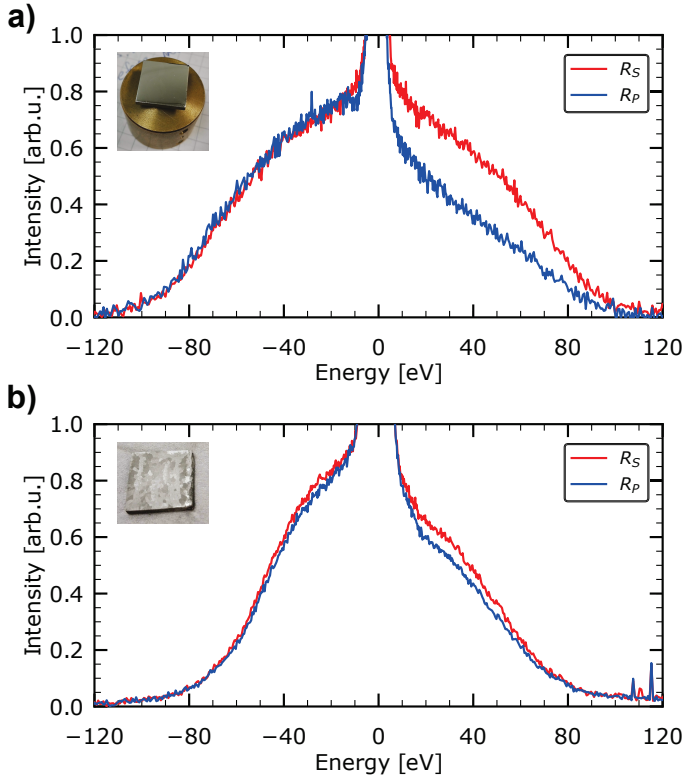


Fig. 4.22: Polarization measurement of a Sn mirror. The applied potential was -120 V for (a) and -100 V for (b). The gas flux was $80 : 80$ sccm for the H-Ar mixed plasma and the axial manipulator was used for both experiments. For both experiments a polarization filter was placed in the optical path before the light, emitted in the plasma, is coupled into the fiber. (a) Measured spectra at an angle of 75° of a polished Sn mirror. In the upper left corner a picture of the measured mirror is shown. (b) Measured spectra at an angle of 75° of the same Sn mirror after heating up and sputtering the surface. In the left upper corner the investigated mirror with the degenerated surface is shown.

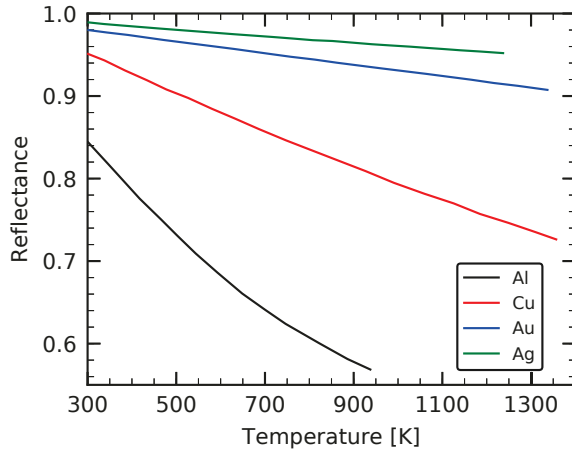


Fig. 4.23: Theoretical calculated temperature dependence of the reflectance of the metals Ag, Al, Au and Cu at a wavelength of 690 nm. The data is digitized and replotted from [Uji72].

changed only by 5% (Fig. 4.25 (a)), similar to the Pd mirror in Sec. 4.6. Thus, the optical properties of the mirror surface did not change during the exposition. After this experiment the same Al mirror was mounted on the axial manipulator. Again the gas flux is adjusted to 40 : 40 sccm, the surface potential was set to $U_s = -100$ V and the mirror was exposed to the plasma for 1 h and every minute one spectra is obtained. But this time the mirror holder is not cooled and thus the temperature of the Al mirror increases during the measurement up to 600 K. Again the first and last measured spectrum of the Al mirror is shown in Fig. 4.24 (b). A dramatic change of the red-shifted component is observed. During 1 h the intensity decreases by a factor of 4 from 0.8 to 0.2. Furthermore, the shape of the Doppler-shifted component changes as well. This means that the mirror surface of the Al mirror is changed during the heat treatment.

In Fig. 4.25 (a) the measured reflectance of the cooled mirror (blue data points), of the heated mirror (red data points) and the theoretical curve of Ujihara (black dashed curve) are shown. The red and black data points are plotted versus temperature, the blue data points versus time (because the temperature of the blue data points is constant at around 300 K). The reflectance for the cooled mirror stays constant within the error bars, which is expected comparing the first and last measured spectrum (Fig. 4.24 (a)). To understand and explain the reflectance behavior of the heated mirror also Fig. 4.25 (b) needs to be taken into account. In Fig. 4.25 (b) the measured reflectance versus the exposure time of the mirror to the plasma is shown in red (belonging to the red y-axis). The black data points represent the measured temperature of the mirror surface using a thermocouple between manipulator and mirror (belonging to the black y-axis). The green data points are the integrals over two different Al lines, namely at 394.40 nm and 396.15 nm (belonging to the green y-axis). These lines were measured using a second spectrometer at PSI-2. The integral over the spectral lines should be a good measure of the Al sputtering during the measurement. Comparing Fig. 4.25 (a) and Fig. 4.25 (b) the following observations

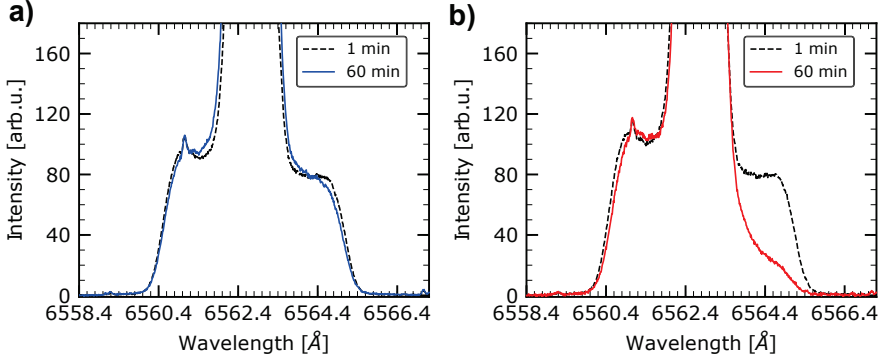


Fig. 4.24: Measured spectra of an Al mirror. For both experiments the gas flux was adjusted to 40 : 40 sccm and the applied surface potential was $U_s = -100$ V. In both experiments the Al mirror was exposed for 1 h to the plasma. (a) For this experiment the radial manipulator was used and the mirror temperature was hold constant at about 300 K during the exposition. (b) For this experiment the axial manipulator was used and the mirror was heated up to about 600 K during the exposition.

are made. At the beginning of the measurement the reflectance of the heated mirror is the same as for the cooled mirror. For the first 10 min or up to a temperature of around 440 K the reflectance of the headed mirror stays constant within the error bars. After 10 min the slope of the reflectance changes and decrease about 15 % from 0.81 to 0.7. This decrease between 380 K – 500 K is in a good agreement with the calculations of Ujihara (compare Fig. 4.25 (a)) [Uji72; CCN77]. At around 500 K or 20 min after the experiment starts the reflectance drops rapidly by 70 % to a value of 0.21 in a time interval of 25 min. After the rapid drop the reflectance stays constant at 0.21 within the error bars for the rest of the experiment. This extreme decrease of reflectance cannot be explained with only the change of temperature of the mirror surface (Fig. 4.25 (a)). The increase of erosion at the surface of Al is responsible for the strong decrease in reflectance (Fig. 4.25 (b)). The integral of the spectral line of the two observed Al lines became stronger by a factor of 5 – 10 within 15 min. The ratio between two integral equals to two, as both lines are originated from the same upper level [Kra18]. Quite remarkable is the delay between erosion and decrease of the reflectance, since the erosion starts 5 – 10 min earlier. The reason is that a layer of ≈ 1 μm needs to be removed by Ar sputtering, before an effect on the spectral reflectance can be observed. After this experiment the mirror surface was completely destroyed and diffusive [Dic18b]. Thus, the second phase of decrease of the reflectance cannot only be explained by temperature but also by an increase of sputtering and thus a mixture of both effects. In the lab after the experiment a reflectance value of the 0.19 was obtained for the destroyed Al mirror. This proves that even for a diffusive mirror the DSRM diagnostic provides reasonable results.

The strong decrease of the reflectance reveals a problem of these kind of experiments. Experiments measuring the spectral reflectance at elevated temperature are very rare and are normally performed using lasers [Min17]. In this experiment the plasma itself was used as a heating source, which works good if the temperature is not too high (for Al below 500 K). But then also sputtering needs to be taken into account

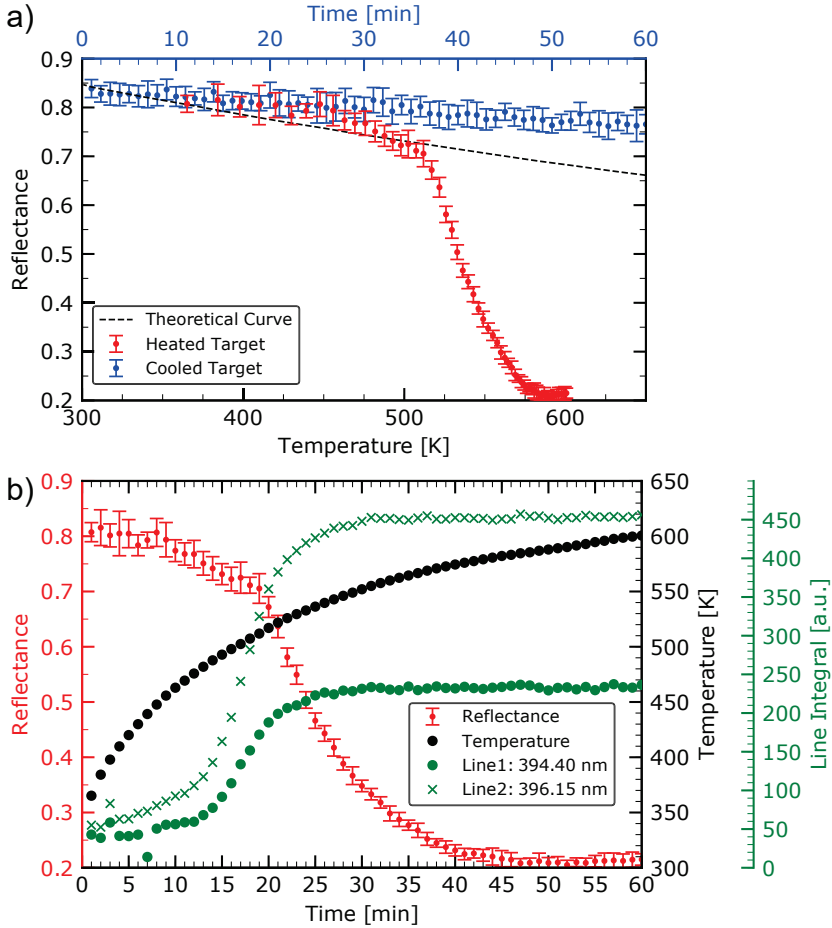


Fig. 4.25: (a) Comparing the temperature dependence of the reflectance of a cooled (blue data points) and a heated mirror (red data points) with the theoretical calculations of Ujihara [Uji72]. (b) Comparing the reflectance dependence of the heated mirror (red data points) with the measured temperature curve (black data points) and the calculated integral of two spectral lines of Al at 394.40 nm and 396.15 nm (green data points). (Images taken from [Dic18b])

and the change of reflectance is caused by both effects simultaneously, which makes it impossible to extract only the temperature part out of the decrease. Therefore a new kind of target holder needs to be designed which is able to heat the mirror directly without using the plasma as heating source. Then it should be possible to measure only the change of the reflectance by temperature with the DSRM diagnostic.

Beside the *in situ* surface degradation of mirrors at elevated temperatures this kind of experiment can also be used to prove the temperature stability of reflectance inside a certain temperature range. Again Rh is taken for this experiment as mirror material because the temperature stability of the spectral reflectance for Rh is important for the CXRS diagnostic at ITER [Mer19]. In the following a Rh polycrystalline mirror was exposed to a 40 : 40 sccm H-Ar mixed plasma. For this experiment the axial manipulator is used in order to be able to heat up the mirror. The mirror was heated up from around 460 K to 650 K within 27 min. For the experiment a surface potential of $U_s = -100$ V is applied and a Doppler-shifted spectrum is recorded each 30 s. Compared to Al the reflectance of Rh stays constant within the error bars of around 3% over the total temperature range. Furthermore, the experiments show that the reflectance of Rh is stable at the expected in-port temperature for the first mirrors in ITER, which is expected to be 533 K [Kri15]. This result is important for the design of the CXRS diagnostic at ITER [Mer19]. The first idea is to explain this difference in behavior by the different atomic masses Al ($Z = 13$) and Rh ($Z = 45$) and thus a different sputtering yield. But the values found in literature are nearly equal with 10^{-1} atoms/ion for Ar sputtering at an energy of 100 eV [Eck07; LW61]. As a consequence, the reason for different temperature dependence of both materials need to be a different one. One possible explanation could be the different melting points of both materials. The melting point of Al is 933 K and for Rh 2237 K [Lid05]. Thus, the maximum temperature of 600 K is only 333 K away from the melting point of Al, whereas the difference to Rh is 1637 K. It is already observed for Cu and Ag that at temperature around 70% of the melting temperature T_m and larger temperatures, the surface of the materials changes due to evaporation [Boh86]. Assuming the same critical point of $0.7T_m$ for Al and taking into account that the temperature of the mirror is measured at the backside of the mirror and not at the exposed front side it is possible that this critical point is reached during the measurement. Thus, the decrease in reflectance and the increase of the line intensity of the Al lines can be explained by evaporation which enhances the sputtering yield [Gus03; Doe05].

In this section it was shown that the DSRM diagnostic is even able to measure the degradation of the mirror surface *in situ*. Using the example of an Al mirror one observes that the reflectance of a cooled Al mirror is not effected by the plasma. Whereas if the mirror is heated up to a temperature of 600 K the surface degenerate and the reflectance decrease rapidly by 75% from 0.81 to 0.21 (Fig. 4.24). At the beginning of the decrease between 380 K – 500 K it is in a good agreement with the theoretical description of Ujihara [Uji72]. For higher temperature the sputtering of Al increase, which is proven by measuring the intensity of two Al spectral lines, namely 394.40 nm and 396.15 nm. The enhanced sputtering leads to a rapid drop of the reflectance, which cannot longer be explained by only temperature effects (Fig. 4.25). For the Rh mirror no temperature dependence of the reflectance can be observed in the temperature range between 460 K and 650 K. This can be explained with the higher melting temperature of Rh compared to Al and thus an increase

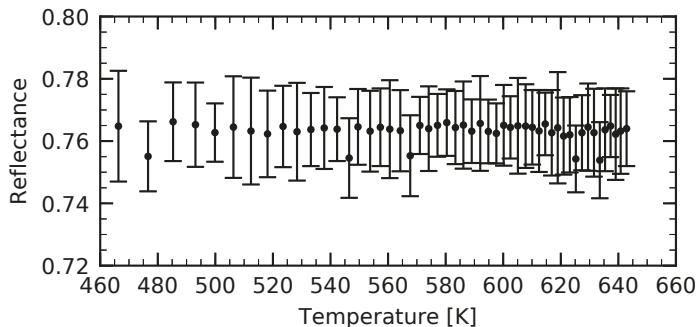


Fig. 4.26: Temperature stability measurement of a polycrystalline Rh mirror. The mirror was heated up to around 650 K in 27 min by plasma heating. The surface potential was -100 V and the gas flux was adjusted to 40 : 40 sccm. The exposure time was set to 30 s. For this experiment the axial manipulator was used.

of evaporation at the Al surface close to the melting point [Boh86; BE93]. Thus, the sputtering of the mirror surface is enhanced at higher temperatures. In this experimental setup it is not possible to distinguish between evaporation effects and physical sputtering by Ar^+ ions.

4.11 Modeling of the Doppler-shifted Emission Profiles

To understand the physical processes behind the Doppler-shifted emission better and to calculate the reflectance values also for the polarization experiments a new model is needed which can describe the Doppler-shifted emission at all possible observation angles. The model developed by Phelps is limited to only two observation angles [Phe09]. Furthermore, Phelps describes the red-shifted emission of the fast atoms by the emission of ions in the sheath, which is hardly applied for the experimental conditions in this thesis. Therefore a model was developed which can describe the Doppler-shifted emission profiles including light reflection. Eq. 4.22 describes the dependency of the intensity of the blue-shifted component on the ion density N_i , the particle reflection coefficient R_N , the density of Ar $n_{\text{Ar}, \text{Ar}^*}$ and the rate coefficient of the excitation $\langle \sigma(E_0) \sqrt{E_0} \rangle$. The same applies for the red-shifted component, but the intensity needs to be additionally multiplied with the spectral reflectance R of the used mirror material. To calculate the emission of the Doppler-shifted components one focuses on the blue-shifted component first. To model the observed emission profile an integration over the complete hemisphere of particles in front of the mirror needs to be done. Therefore the following integral is solved [Dic19a]

$$\epsilon_b(\Delta\lambda) = \int_v f(v) \langle \sigma v \rangle dv^3, \quad (4.23)$$

where $\epsilon_b(\Delta\lambda)$ is the emission at the Doppler-shifted wavelength $\Delta\lambda$ compared to the unshifted wavelength λ_0 and $\langle \sigma v \rangle$ is the excitation rate coefficient for the interaction between H atoms with energy E and Ar atoms. The Doppler-shift is calculated

with $\Delta\lambda/\lambda = \mathbf{v}\mathbf{e}_{\theta_0}/c$, with the unit vector \mathbf{e}_{θ_0} along the LOS, the velocity of the backscattered atoms \mathbf{v} and the velocity of light c . $f(v)$ is the normalized distribution function of the backscattered atoms ($\int_v f(v)dv^3 = 1$). For the interaction of Ar and H the rate coefficients are calculated using Eq. 4.24 [Dic19a] and the cross section calculations of *Van Zyl et al.* [Van80].

$$\langle\sigma v\rangle(E) = \exp\left(-\left(\frac{a_0}{E}\right)a_1\right) \cdot (a_2 + a_3 \log_{10}(E)), \quad (4.24)$$

where a_0 , a_1 , a_2 and a_3 are free parameters. To solve the integral in Eq. 4.23 the assumption is made that the distribution function $f(v)$ can be separated in an angular part $f_1(\theta)$ and a kinetic part $f_2(v)$:

$$f(\theta, E) = f_1(\theta) * f_2(E) \quad (4.25)$$

For the angular function a power cosine distribution (Eq. 2.6) is used which is proposed by Eckstein and Biersack [EB85]. The energy distribution is modulated by Eq. 2.8 which reproduces the calculated TRIM spectrum in Fig. 2.3. Both functions are already discussed in detail in Sec. 2.2.

Putting everything together, the model is tested for the polarization measurements of the W mirror, already presented in Sec. 4.9 and for comparison also with the measurement at 35° . In Fig. 4.27 the result of the modeling process of the measurement at a LOS of 35° is shown and in Tab. 4.1 the reflectance values obtained by the model are presented. The fitting parameter b for the angular distribution and β for the energy distribution obtained by the fit are shown in Tab. 4.2. For the measurement a surface potential of -120 V was applied, the gas flux was adjusted to $40 : 40$ sccm and the neutral gas pressure in the exposition chamber was 4.4×10^{-2} Pa. It is found that the model already gives a good description of the Doppler-shifted emission although not all interactions leading to the Doppler-shifted emission are included. The model does not consider the fine structure of the Doppler-shifted emission, the magnetic field of $B = 0.1$ T or the contribution of fast atoms created out of H_2^+ ions. The local minimum close to the passive H_α line is not an error in the model, but shows the importance of the emission of fast atoms created out of former H_2^+ ions. The reflectance value obtained by the fit is $R = 0.53$, which agrees with the value of $R = 0.53$ of *Werner et al* [WGA09]. The DSRM diagnostic has measured a value of $R = 0.59$, which is a difference of 10% and a difference of 3% to the value obtained by *Minissale et al* [Min17]. Thus the model can also be used to determine the spectral reflectance with a good accuracy out of the measured spectrum at an observation angle of 35° .

Even more important are polarization measurements at a higher observation angles (Fig. 4.28). The experimental conditions are the same like before only the observation angle was changed to 69° . Again the spectra is fitted and the obtained reflectance values are shown in Tab. 4.1 and the fitting parameters in Tab. 4.2. It turns out that also for the polarization measurements the model can fit the experimental data quite well. The blue-shifted component is in good agreement with the experiment except of the part where the H_2^+ ions contribute to the emission profile. But it seems difficult to fit the red-shifted component at a higher observation angle. A reason for this could be that the plasma is not symmetrical anymore at an angle of 69° . The plasma symmetry is not included in the model and thus its effect on the geometry of the blue and red-shifted component is neglected. Nevertheless, the agreement

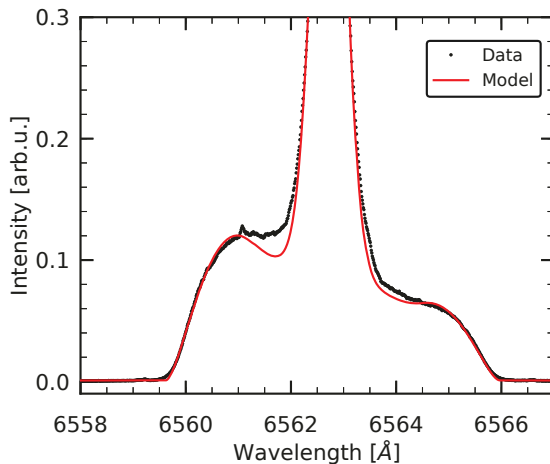


Fig. 4.27: Experimental spectrum of H_α using a W mirror (black dots) measured under an observation angle of 35° and fitted with the developed model (red curve). For the experiment the target potential was set to -120 V. The gas flux was adjusted to 40 : 40 sccm and the neutral gas pressure was 4.4×10^{-2} Pa.

	R_S	R_P	R
Model 35°	-	-	0.53
Werner et al	0.59	0.46	0.53
Minissale et al	-	-	0.55
Model 69°	0.68	0.08	0.38
Werner et al	0.80	0.19	0.49

Table 4.1: Comparison of fitted reflectance values and data taken from [WGA09] and [Min17].

Model	b	β
Fit 35°	0.2	1.6
Fit 69° , R_P	0.2	1.4
Fit 69° , R_S	0.2	2.1

Table 4.2: Fit parameters of the different fitted spectra.

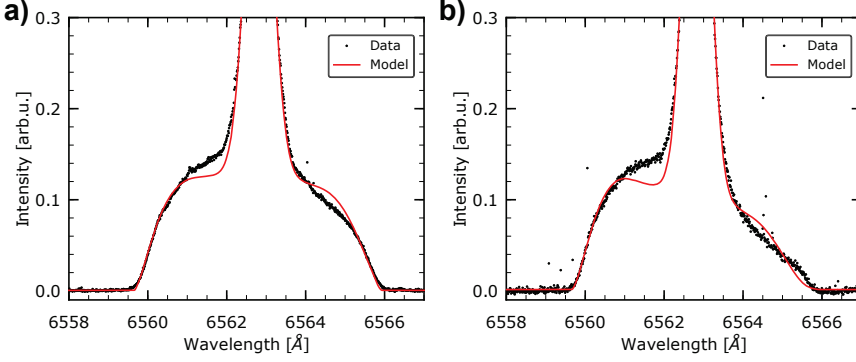


Fig. 4.28: Experimental data of a W mirror (black dots) measured under an observation angle of 69° and fitted with the developed model (red curve). For the experiment the surface potential was set to -120 V. The gas flux was adjusted to 40 : 40 sccm and the neutral gas pressure was 4.4×10^{-2} Pa. (a) Spectrum of the measurement of R_S . (b) Spectrum of the measurement of R_P .

between fitted reflectance values and values taken from literature is in the range of 10–15 %, except of the data for R_P . Here again it seems difficult to measure the low spectral reflectance experimentally, similar to C. One can conclude that with this model it is now possible to measure also the polarization components R_S and R_P with the DSRM diagnostic by modeling the Doppler-shifted components, because the calculation of the spectral reflectance does not depend on the exact values of b and β . Nevertheless, the model still have some issues which will be discussed in the following.

During the fitting process it turns out that if only one LOS is taken into account, more than one solution for b and β can fit the experimental data in a good agreement. The reason is that several combinations of angular and energy distribution can describe the observed Doppler-shift. Thus, at least a second LOS is needed in order to reduce the possible combinations of b and β . As can be seen in Tab. 4.2 b is held constant at 0.2 between the measurements of 35° and 69° so that the variation of β is as small as possible for all fitted spectra, as can be found in [Dic19a]. This is the only solution that fits the experimental data for all three measurements and is thus the unique solution to describe the observed experimental data. However, the TRIM code predicts a much higher value $b = 1.5$ (TRIM calculations of D. Reiter) for H on W with an incident energy of $E_0 = 100$ eV [EB85]. The difference between the model and TRIM calculations could be explained by penetration of H or Ar into the target e.g. retention of H, but it is still not clear. Compared to the results of *Phelps et al.* ($b = 0.6$, at $E = 2$ keV) [Phe09], ($b = 0.6$, at $E = 4.5$ keV) [Lan84] and ($b \approx 1$, for $E > 5$ keV) [VEB80] the result of $b = 0.2$ shows at least a consistent trend: by decreasing the energy of H atoms the distribution becomes broader. Again it is still not clear if the retention of H in the target and destruction by Ar^+ plays any role. Thus, further investigations on this topic are highly needed in the future. Nevertheless, the spectral reflectance can be calculated out of spectrum independent from the exact values of b and β , which is important for the DSRM diagnostic.

4.12 Gas and Pressure Scan of Different Mixed Plasmas with Ar, Kr and Ne

In a mixed plasma fast H atoms cannot only be excited Ar atoms, but also by other nobles gases like Ne or Kr [LM93]. The experiments on the fast H atom emission in mixed plasmas with Ne, Kr and Ar were performed by *Lavrov et al* at a pressure of 2.6×10^2 Pa, which is a factor of 10^4 higher compared to the condition used in this thesis. Again, for low density plasmas ($p < 1$ Pa) no experimental data is available. Therefore, the Doppler-shifted emission of fast H atoms is also tested in a H-Ne and H-Kr mixed plasma at the low density of the PSI-2 device and the results are compared to the measurements in H-Ar.

In Fig. 4.29 the experimental data for different plasma mixtures of H-Ar, H-Kr and H-Ne are presented. All measurements are performed using a Pd mirror at a negative potential of -100 eV. The gas flux and the composition was varied in a way that the neutral gas pressure in the exposition chamber stays nearly constant at around 4×10^{-2} Pa. The experiment shows that Ar has the highest signal intensity of the Doppler-shifted emission, compared to Kr and Ne. Furthermore, one can see that the highest signal is achieved if a factor of 2 – 3 more Ar than H is used in the mixture (20 : 50 or 30 : 60), but on the other hand the passive H_α component is reduced compared to an equal composition (40 : 40, red curve). For this configuration the Doppler-shifted emission is only a factor 1.2 less, but the intensity of the passive component increases by a factor of 2, which results in a better signal-to-noise ratio. For Kr the highest intensity for the Doppler-shifted components are achieved if only a little amount of Kr is mixed into the H plasma (60 : 05) or if a low gas flux of H and Kr is used but with the same amount of both gases (10 : 10). For Ne the Doppler-shifted emission is a factor of 14 weaker than for Ar and is not further investigated.

In Fig. 4.31 the spectrum for each noble gas with the highest signal-to-noise ratio is depicted. The plasma parameters for the three measurements are summarized in Tab. 4.3. It is clearly observed that the intensity of the Doppler-shifted emission is a factor of 3 – 5 higher by using Ar compared to Kr. The plasma parameters like n_e , T_e and p are comparable for both measurements as can be seen in Tab. 4.3 and Fig. 4.30. Therefore, the difference in the gas fluxes cannot explain the different signal intensity. This difference in the intensity of the Doppler-shifted H_α emission in a H-Ar and H-Kr plasma is also observed in other experiments [LM93] and also in D mixed plasmas [Bra17]. To answer this open question, the cross section for excitation by the ground state is taken into consideration, since excitation by the ground state is the most common kind of interaction. In Fig. 4.32 the cross sections for the excitation to $H(n = 3)$ by Ar [Van80], by He [VGN83], by Ne [VGN85], by Kr and Xe [VNG86] are shown. It is found that the excitation cross section for Ar and Kr are nearly equal in the energy range of 80 eV – 200 eV, which is not expected taking the experimental observations into consideration. The excitation cross section of Ne and He is a factor of 10 less compared to Ar and Kr. Thus, the difference of the experimental data cannot be explained by ground state excitation.

Beside ground state excitation also other processes are known to excite H atoms in a mixed plasma. *Clyne et al.* have found that H can be excited by metastable Ar to $H(n = 2)$ [CM77; Cly80]. The energy band diagram of this reaction is shown in Fig. 4.33. In this interaction metastable Ar and H built an excimer molecule for a short

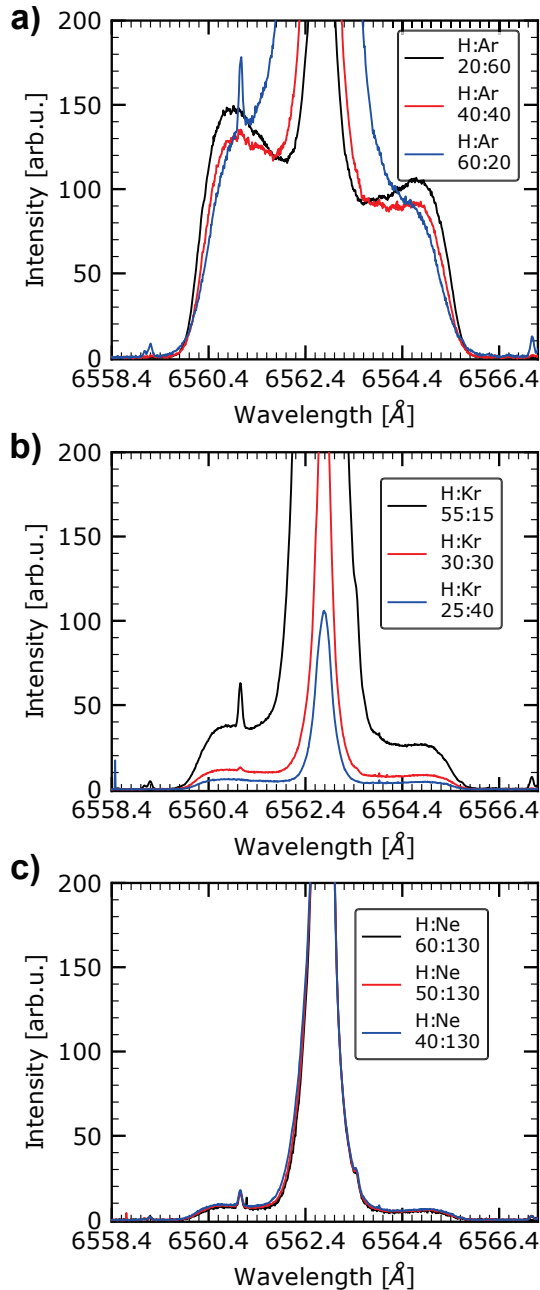


Fig. 4.29: H_α spectrum obtained in different mixed plasmas of H-Ar (a), H-Kr (b) and H-Ne (c). For all measurements a Pd mirror was used with a negative target potential of -100 V. The gas flux was varied under the condition that the neutral gas pressure in the exposition chamber stays constant. To make the spectra comparable the measured signal of each spectrum is divided by the exposure time of the camera.

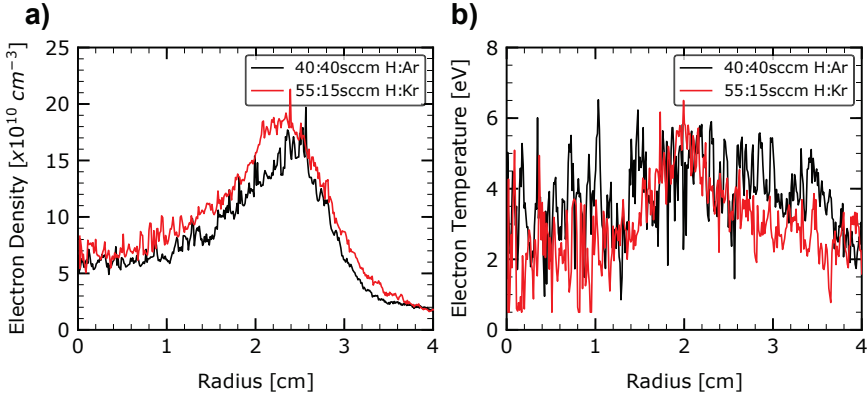


Fig. 4.30: Langmuir probe measurement of the H-Ar (40 : 40 sccm) and H-Kr (55 : 15 sccm) mixed plasmas. The neutral gas pressure was $p = 3.9 \times 10^{-2} \text{ Pa}$ and $p = 4.1 \times 10^{-2} \text{ Pa}$, respectively. In (a) the electron density and in (b) the electron temperature is shown.

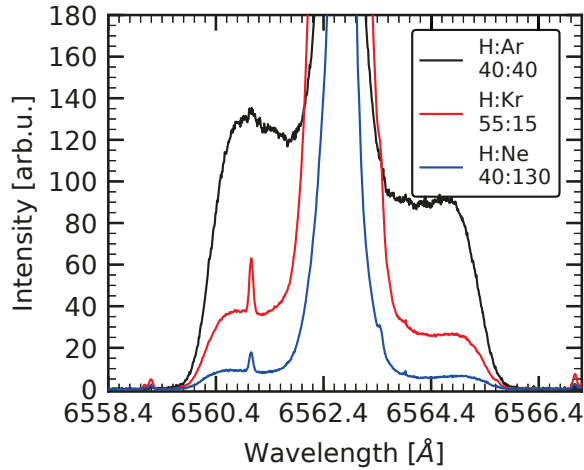


Fig. 4.31: Comparison of the H_α emission spectra of three different gas mixtures, namely H-Ar, H-Kr and H-Ne. The used composition and gas flow of the measurement is given in the graphs legend (the unit is sccm). For all measurements a Pd mirror was used and the target potential was -100 V neutral gas pressure in the exposition chamber was $3.9 \times 10^{-2} \text{ Pa}$ for Ar, $4.1 \times 10^{-2} \text{ Pa}$ for Kr and $2.6 \times 10^{-2} \text{ Pa}$ for the measurement with Ne.

Plasma	Gas flux [sccm]	n_e [cm^{-3}]	T_e [eV]	p [Pa]
H-Ar	40 : 40	1.8×10^{11}	4	3.9×10^{-2}
H-Kr	55 : 15	1.9×10^{11}	4	4.1×10^{-2}
H-Ne	40 : 130	1.6×10^{11}	4	2.6×10^{-2}

Table 4.3: Plasma parameters of the different gas configurations in Fig. 4.31.

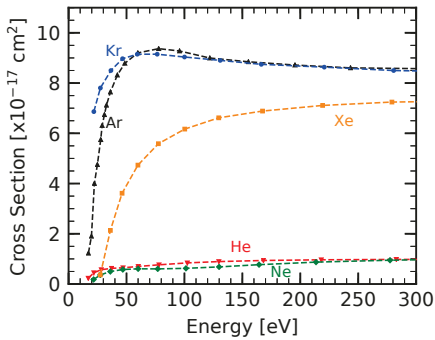


Fig. 4.32: Cross sections for the ground state excitation of H to the state $n = 3$ for He, Ar, Ne, Kr, Xe. The data is digitalized and taken from [Van80] for Ar, from [VGN83] for He, from [VGN85] for Ne and from [VNG86] for Kr and Xe.

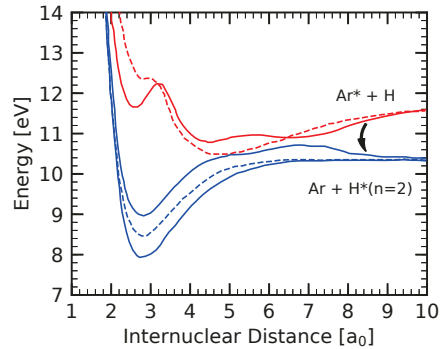


Fig. 4.33: Potential curve for H and Ar. The data is digitalized and taken from [VG80].

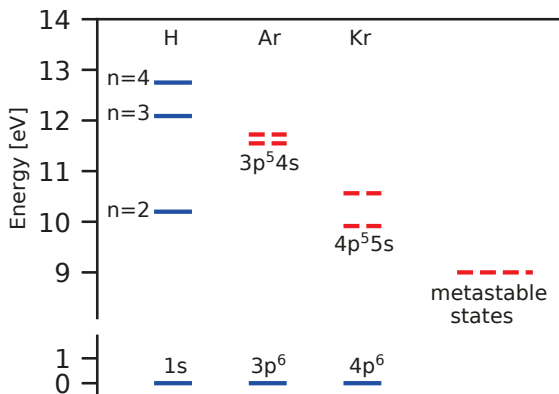


Fig. 4.34: Grotian diagram of H, Ar and Kr. The first three excited levels of H and the metastable states of Ar and Kr are shown. The data is taken from the NIST database [Kra18].

time if they are brought close together (inter nuclear distance $< 5a_0$ where a_0 is the Bohr radius). After this formation the molecule diffuses again in $H^*(n = 2)$ and Ar in the ground state. Clyne has called this process non-adiabatic potential crossing (Fig. 4.33).

He proved this excitation process for the Lyman- α line, but the overall principle could be the same for the Balmer- α line. Taking the Grotian diagram for H, Ar and Kr into account, one found that the $n = 3$ state is close to the metastable levels of Ar (the energy difference is only around 0.5 eV and -1.5 eV to the $n = 2$ level (Fig. 4.34) in comparison to other gases). As a consequence, the interaction between H and Ar* to excite H to the level $n = 3$ should be an endothermic process compared to the exothermic process for the Lyman- α line ($n = 2$). The energy difference between H($n = 3$) and the Kr metastable state is around 1.5 eV and thus a factor of 3 greater compared to Ar. This could explain the difference in the signal intensity which is observed in Fig. 4.31. As a consequence, it is possible that the fast H atoms are excited by Ar in the metastable state rather than in the ground state, but theoretical calculation for excitation of H atoms by Ar atoms in the ground state or metastable fraction is until now not available. To give an answer about the excitation process of H by Ar, a TDLAS system is installed at the PSI-2, to measure the metastable density in the plasma and to study the interaction between H and Ar further.

CHAPTER 5

MEASUREMENTS OF METASTABLE AR IN PSI-2

The results of the emission of fast atoms in the PSI-2 plasma have demonstrated that in addition to excitation by the ground state of Ar ($Ar + H \rightarrow H^*(n=3) + Ar$) also the excitation transfer between the metastable states of Ar and H ($Ar^* + H \rightarrow H^*(n=3) + Ar$) could be considered as the leading reaction increasing the Doppler-shifted emission of the H_α line. The population of metastable levels cannot be measured by OES, therefore other diagnostics have to be involved. One of the most used diagnostics to measure the density of a species in a gas or plasma is the **Tunable Diode Laser Absorption Spectroscopy (TDLAS)**. In this thesis TDLAS is used to measure the metastable Ar density in the PSI-2 and the results are discussed in the following.

Sec. 5.1 and Sec. 5.2 deal with the theory of TDLAS and the setup of such a system at the PSI-2 device. In Sec. 5.3 the impact of the magnetic field on the absorption profile is investigated and how the Zeeman splitting can be used to determine the magnetic field of the PSI-2 device. In Sec. 5.4 the metastable density in a pure Ar plasma is determined, a radial scan is performed in order to obtain the radial distribution of the metastable density in a pure Ar plasma and the obtained values are cross checked by theoretical calculations. Last in Sec. 5.5 the influence of hydrogen in a pure Ar plasma is examined as well as the influence of the laser beam on the Doppler-shifted emission on the H_α line.

5.1 Theoretical Aspects of Tunable Diode Laser Absorption Spectroscopy (TDLAS)

The **Tunable Diode Laser Absorption Spectroscopy (TDLAS)** is a routine technique to measure the temperature and density of gases and molecules using a tunable laser in different kind of scenarios [Kun02; Nie10; Nie12]. The laser frequency (wavelength) is tailored to fit for a certain line transition in the atom or molecule species that should be analyzed. A schematic picture of a TDLAS system is shown in Fig. 5.1. In this thesis a TDLAS system is used to measure the density of metastable Ar atoms in the PSI-2 device. The diagnostic measures the absorption of the laser beam in

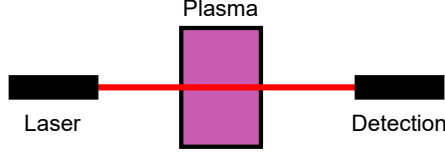


Fig. 5.1: Schematic picture of a TDLAS system to measure the density of a species.

the gas or plasma described by the Beer-Lambert law (Eq. 5.1) [Nie10; Sad04]:

$$T(\nu) = \frac{I(\nu)}{I_0(\nu)} = \exp(-\alpha(\nu) \cdot L) , \quad (5.1)$$

where $T(\nu)$ is the transmittance signal at frequency ν , $I(\nu)$ and $I_0(\nu)$ are the intensity at frequency ν with and without absorbing species, $\alpha(\nu)$ is the absorption coefficient and L is the absorption length of the laser signal. The absolute concentration of a species n_s can be calculated using the total transmittance and the Beer-Lambert law. Four different measurements need to be performed in order to avoid influence by the experimental setup and the diagnostic itself (e.g. transmittance of windows in the optical pass or plasma properties) [Nie10]:

$$\begin{aligned} L(\nu) &- \text{Plasma and Laser on,} \\ L_0(\nu) &- \text{Plasma off, Laser on,} \\ P(\nu) &- \text{Plasma on, Laser off,} \\ B(\nu) &- \text{Plasma and Laser off.} \end{aligned} \quad (5.2)$$

The total transmittance can be calculated with the following formula:

$$\frac{I(\nu)}{I_0(\nu)} = \frac{L(\nu) - P(\nu)}{L_0(\nu) - B(\nu)} \quad (5.3)$$

The absorption coefficient α in Eq. 5.1 is connected to the total population of metastable atoms by

$$\alpha(\nu) = \frac{e^2}{4\epsilon_0 c m_e} f_{if} N_i F(\nu) , \quad (5.4)$$

where e is the elementary charge, ϵ_0 is the dielectric constant, c is the velocity of light, m_e is the electron mass, f_{if} is the oscillator strength of the investigated transition from state with quantum number n_i to n_f , N_i is the density of the lower level and $F(\nu)$ is the normalized function representing the absorption line shape [Nie10]. The area S under the line-integrated absorption curve can be connected to the metastable density by Eq. 5.5:

$$\int_0^\infty \ln \left(\frac{I_0(\nu)}{I(\nu)} \right) d\nu = S = \frac{e^2 f_{if} L}{4\epsilon_0 m_e c} N_i \quad (5.5)$$

The total metastable density can then be calculated out of the experimental data with Eq. 5.6:

$$N_i = \frac{4\epsilon_0 m_e c}{e^2 f_{if} L} S \quad (5.6)$$

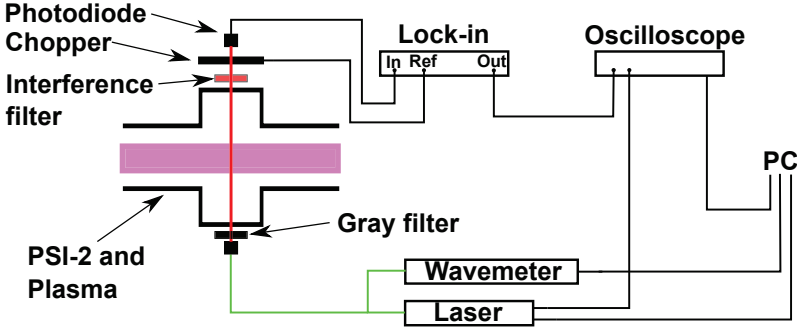


Fig. 5.2: Schematic of the TDLAS setup at PSI-2.

5.2 TDLAS Setup at PSI-2

The TDLAS diagnostic at PSI-2 was built up in cooperation with the Institute of Experimentalphysik V at the Ruhr University Bochum and is schematically shown in Fig. 5.2. The laser source is a tunable diode DLpro laser from Toptica with an output of 70 mW at 763.5 nm. The wavelength range of the laser is between 750 nm – 795 nm and can be adjusted freely by varying the diode temperature and the grating position. During a measurement the laser wavelength is scanned in the range of 1 nm to measure the absorption signal as a function of the laser wavelength. To monitor the actual wavelength of the laser during the measurement it is checked using a wavemeter WS-6 produced by HighFinesse by splitting up the laser beam in the ratio 99 : 1. 99% are guided with a fiber to the PSI-2 device and 1% is guided into the wavemeter. The wavemeter has a precision of around 0.1 pm. The laser beam is coupled into a fiber and transported to the PSI-2 device, where it is coupled out and transmitted through a filter wheel with different gray filters (as shown in Fig. 5.2). With the gray filters the laser intensity, which is coupled into the plasma, can be adjusted. The used plasma in the PSI-2 device is an Ar plasma with a gas flow of 40 sccm. The plasma characteristics measured with a Langmuir probe are shown in Fig. 5.3.

If the laser wavelength is close to the wavelength of the line transition, the laser pumps electrons from the metastable level into a higher energy level (for more explanation see Sec. 5.1). The following experiments focus on the Ar I transition from $1s_5 \rightarrow 2p_6$ with a wavelength of 763.5106 nm in air. As a consequence, laser power is absorbed in the plasma and the reduction of the signal can be measured. Behind the plasma the laser beam is chopped up with a chopper wheel to modulate the laser beam and analyze the resulting signal with a Lock-in amplifier (Ortholoc Model 9502). The frequency of the chopper wheel can be freely adjusted between 1 Hz and 1 kHz with a precision of 1 Hz. The modulated signal is measured with a photo diode and analyzed using the Lock-in amplifier. In front of the photo diode an aperture and an interference filter are mounted to filter out all wavelengths which are not close to the transition wavelength of 763.5106 nm. The Lock-in amplifier uses the signal of the chopper wheel as the reference signal $V_{ref} = V_r \sin(\omega_{ref}t + \theta_{ref})$, where V_r is the amplitude of the reference signal, ω_{ref} is the frequency of the chopper wheel and θ_{ref} the phase of the chopper wheel. The input signal of the Lock-in amplifier $V_{inp} = V_{sig} \sin(\omega_{sig}t + \theta_{sig})$ is measured by the photo diode. By using a

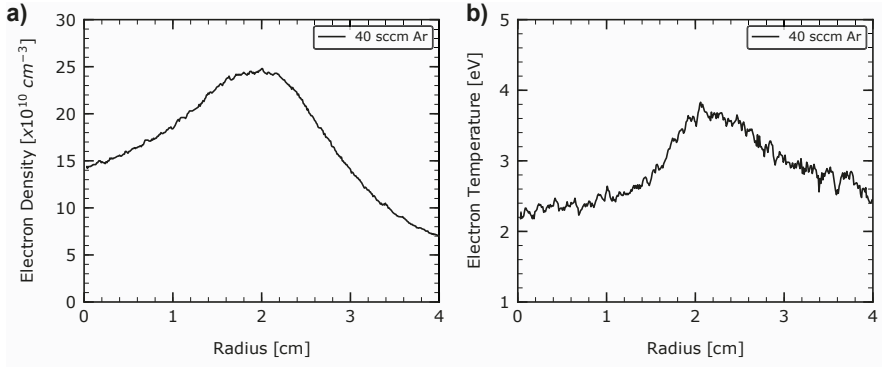


Fig. 5.3: Langmuir probe measurements of the Ar plasma used for the TDLAS measurements at PSI-2. The neutral gas pressure was $p = 3.4 \times 10^{-2}$ Pa. In (a) the electron density is presented and in (b) the electron temperature.

Configuration	J	Paschen	E [eV]
$3s^23p^5(^2P_{3/2})4s$	2	$1s_5$	11.55
$3s^23p^5(^2P_{3/2})4s$	1	$1s_4$	11.62
$3s^23p^5(^2P_{1/2})4s$	0	$1s_3$	11.72
$3s^23p^5(^2P_{1/2})4s$	1	$1s_2$	11.83
$3s^23p^5(^2P_{3/2})4p$	1	$1p_{10}$	12.90
$3s^23p^5(^2P_{3/2})4p$	3	$1p_9$	13.08
$3s^23p^5(^2P_{3/2})4p$	2	$1p_8$	13.09
$3s^23p^5(^2P_{3/2})4p$	1	$1p_7$	13.15
$3s^23p^5(^2P_{3/2})4p$	2	$1p_6$	13.17
$3s^23p^5(^2P_{3/2})4p$	0	$1p_5$	13.27
$3s^23p^5(^2P_{1/2})4p$	1	$1p_4$	13.28
$3s^23p^5(^2P_{1/2})4p$	2	$1p_3$	13.30
$3s^23p^5(^2P_{1/2})4p$	1	$1p_2$	13.33
$3s^23p^5(^2P_{1/2})4p$	0	$1p_1$	13.48

Table 5.1: Electronic configuration and Paschen notation shown for the lowest excited levels of Ar [Kra18].

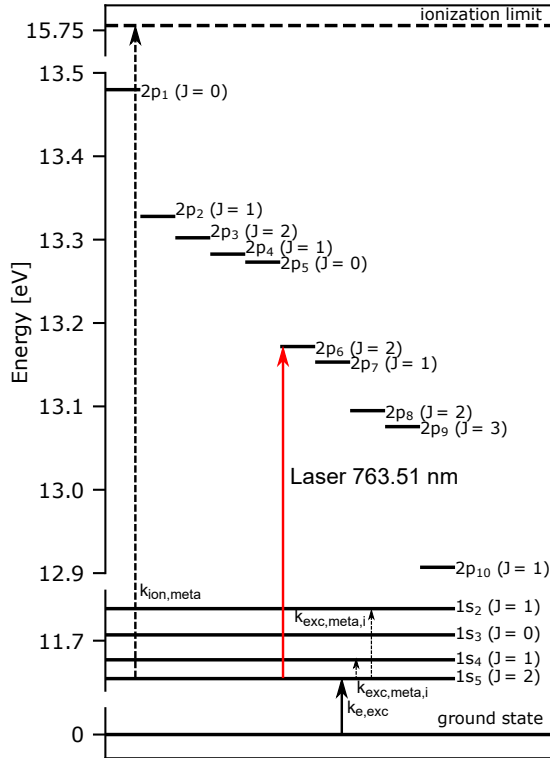


Fig. 5.4: Grotian diagram of Ar showing the ground state, the first 14 excited levels in Paschen notation and the ionization limit taken from NIST database [Kra18]. The transition from $1s_5$ to $2p_5$ is pumped by the laser to measure the metastable Ar density (shown with the red arrow). The black arrows represent the production channel (electron excitation) and the dashed arrows the considered loss channels (electron excitation in resonant states, electron impact ionization and not shown here diffusion) for the $1s_5$ state.

phase-sensitive detector (PSD) the output signal can be measured as the product of both signals [Sys11]:

$$\begin{aligned} V_{out} &= V_r V_{sig} \sin(\omega_{ref} t + \theta_{ref}) \sin(\omega_{sig} t + \theta_{sig}) \\ &= 0.5 V_r V_{sig} \cos([\omega_{sig} - \omega_{ref}]t + \theta_{sig} - \theta_{ref}) - \\ &\quad 0.5 V_r V_{sig} \cos([\omega_{sig} + \omega_{ref}]t + \theta_{sig} + \theta_{ref}) \end{aligned} \quad (5.7)$$

The output are two AC signals, one with the difference frequency $\omega_{sig} - \omega_{ref}$ and one with the sum frequency $\omega_{sig} + \omega_{ref}$. By passing the output signal through a low pass filter the AC signals are removed. In this case no signal will be left. Assuming $\omega_{sig} = \omega_{ref}$ the difference signal turns into a DC signal [Sys11]. If the signal is multiplied again with a reference signal shifted by 90° , the result after the low pass filter is:

$$V_{out} = 0.5 V_r V_{sig} \sin(\omega_{sig} - \omega_{ref}) \propto V_{sig} \sin(\theta) , \quad (5.8)$$

where $\theta = \omega_{sig} - \omega_{ref}$. Now two outputs are possible, which are called X (in-phase component) and Y (quadrature component) [Sys11]:

$$X = V_{sig} \cos(\theta) \quad Y = V_{sig} \sin(\theta) . \quad (5.9)$$

Defining both quantities in a polar coordinate system, also the length R and the phase θ can be expressed as:

$$R = \sqrt{X^2 + Y^2} \quad \theta = \tan^{-1} \left(\frac{Y}{X} \right) . \quad (5.10)$$

The Lock-in amplifier used in this thesis can measure all four quantities X , Y , R and θ . For the results presented in the following R is measured, because it is independent of the phase θ . The Lock-in amplifier allows to change the sensitivity of the detection, offsets of the signals and amplification, thus in order to get the actual input voltage the output voltage needs to be converted using Eq. 5.11 [Sys11]:

$$U_{out} [\text{V}] = \left(\frac{U_{in} [\text{V}]}{f_{sens} [\text{V}]} - U_{offset} [\text{V}] \right) \times f_{expand} \times 10 \text{ V} , \quad (5.11)$$

where U_{in} is the input signal, f_{sens} is the sensitivity, f_{offset} is the adjusted offset with a maximum of 10 V and f_{expand} is the amplification of the output which can be a factor of 1, 10 or 100. The Lock-in signal is depicted on an oscilloscope and further analyzed to obtain the metastable density out of the absorption signal.

The principle of the measurements are as follows. The oscilloscope measures the piezo voltage and laser absorption signal of the plasma measured with the photo diode. At the same time the wavemeter measures the wavelength of the laser as a function of piezo voltage as the laser wavelength cannot be detected by oscilloscope directly. The conversion process is described in detail in the following.

The laser wavelength is analyzed by the wavemeter and the result can be displayed on the computer (Fig. 5.5 (a)). The wavelength is changed by sweeping the voltage of the piezo crystal, which changes the angle of the internal grating. The voltage characteristic of the laser is measured with the oscilloscope (Fig. 5.5 (b) black curve). Unfortunately it is not possible to display the wavemeter output on the oscilloscope as well. Therefore, a relation between the voltage amplitude of the piezo signal and the wavemeter measurement has to be made (this is indicated by the red circles and

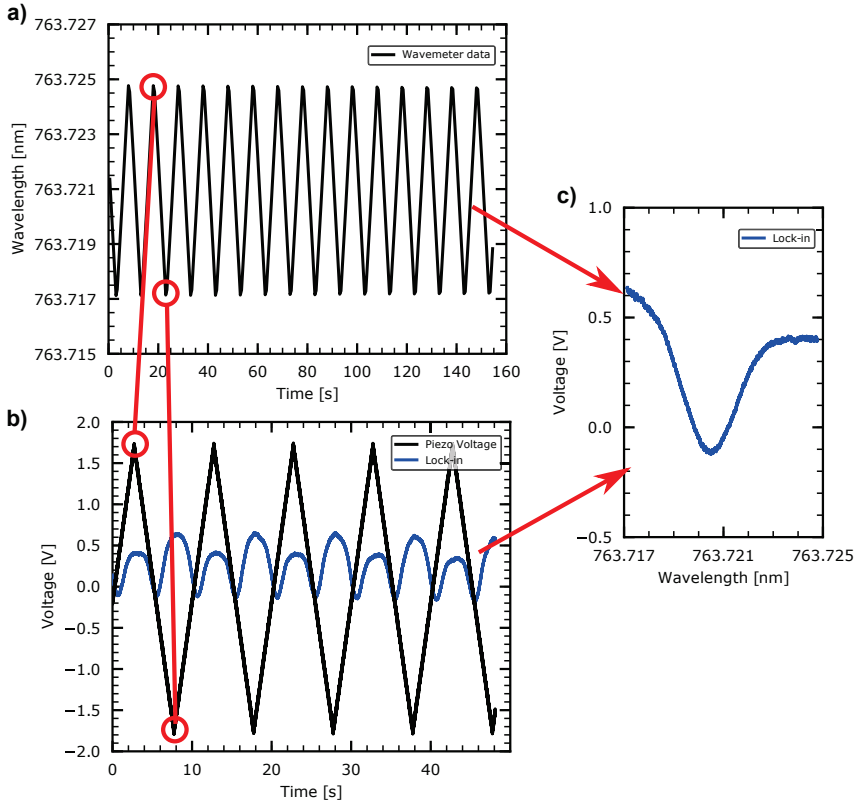


Fig. 5.5: Schematic of the x-axis conversion of the oscilloscope using the data measured by the wavemeter. The spectrum is measured in an Ar plasma with a gas flow of 40 sccm. The plasma characteristics are shown in Fig. 5.3. (a) Data obtained by the wavemeter during the voltage sweep of the piezo crystal. (b) Voltage characteristic of the piezo crystal and absorption signal measured with the photo diode and the Lock-in amplifier visualized with the oscilloscope. (c) The same absorption signal like in (b), but plotted with the converted x-axis.

lines). The maximum in the piezo voltage is also the maximal wavelength which can be achieved. Assuming a linear relation between piezo voltage and wavelength, the temporal evolution of the piezo voltage is recalculated into the wavelength or the frequency of the laser (Fig. 5.5 (c), the blue signal is the measured absorption signal of the photo diode and the Lock-in amplifier).

5.3 Impact of the Magnetic Field on the Absorption Profile of the Metastable Density

In the previous chapter the Doppler broadening dominates over all other possible broadening mechanisms in PSI-2 for the H atom. However, for the Ar atom the

situation is different as the Doppler broadening of Ar is a factor of $1/\sqrt{40}$ less, at the same gas temperature. Therefore, one has to investigate if for instance the Zeeman effect could be neglected as in case of H. Thus, the theoretical Zeeman pattern for the transition from $J = 2 \rightarrow J = 2$ is calculated using Eq. 2.34 and is shown in Fig. 5.6. For the $1s_5$ level a Landé factor of $g = 1.506$ and for the $2p_6$ level $g = 1.305$ is used (taken from the NIST database [Kra18]). The x-axis is the energy shift of the lines with respect to the unshifted line in units of $\mu_B B$ and the y-axis is the relative intensity of the lines. The theoretical profile demonstrates the following: the π -components are in the center of the transition line, whereas σ^+ or σ^- lines are at the blue or red-shifted wavelengths of the spectral line.

Before the experimental data can be fitted, the linear background of the measured data is removed. After this step the data is fitted using eight Gaussian functions (Eq. 5.12), one for each Zeeman component [Dic19b].

$$I(\nu) = \sum_i A_i \exp\left(-\left(\frac{\nu - \nu_{0,i}}{\sqrt{2}\sigma_i}\right)^2\right), \quad (5.12)$$

where A_i is the amplitude, ν_i is the center position and σ_i is the width of component i . The first component (which is always the left one in Fig. 5.7 (c)) is fitted freely. For the other components different constrains are defined and the magnetic field B is added as an additional fitting parameter:

1. For the intensity of the components A_i : $A_{i,i \neq 0} = \sum_{i=1}^8 \frac{I_{r,i}}{I_{r,0}} \cdot A_0$, where I_r is the theoretical relative intensity of each component.
2. For the center position $\nu_{0,i}$: $\nu_{0,i} = \nu_{0,0} + |E_{r,0} - E_{r,i}| \cdot \frac{\mu_B}{h \cdot 10^{12}} \cdot B$, where $E_{r,i}$ is the theoretical relative energy shift and B a fitting parameter for the magnetic field.
3. For the width σ_i : $\sigma_i = \sigma_0$

The constrains for the intensity A_i and the center position $\nu_{0,i}$ follow directly from the theoretical Zeeman pattern for the observed transition according to Eq. 2.34. With the last constrain for the width σ_i the same temperature for all components is set. As a consequence, the number of free fitting parameters reduces to four, namely A_0 , $\nu_{0,0}$, σ_0 and B . The other parameters are bound by the constraints to these four. In order to measure the Zeeman splitting experimentally, a polarization filter was installed between the photo diode and the chopper wheel [Dic19b]. The results of the TDLAS measurements and the fit of the σ -components are shown in Fig. 5.7. The variation of the magnetic field in the PSI-2 plasmas is achieved by a variation of the coil current. The standard current I_0 for the six magnetic coils are shown in Tab. 5.2. In Fig. 5.7 the fitted Zeeman spectrum on the experimental data is presented. Note that in the model the hyperfine structure of Ar is neglected [Wil11]. The coil current is adjusted to $I_{coil,i} = 0.25I_{0,i}$ (Fig. 5.7 (a)) and $I_{coil,i} = 0.35I_{0,i}$ (Fig. 5.7 (b)), where i is the coil number. The theoretical lines are the solid black lines, the single fitted components are the dashed black lines and the total fit is depicted by the red solid line. The fitting model is in good agreement with the experimental data. The small asymmetry in the experimental spectrum in Fig. 5.7 (b) cannot be reproduced because a symmetrical distribution of the σ -components around the unshifted component is demanded. The asymmetry regarding the unshifted component in the experimental data could still

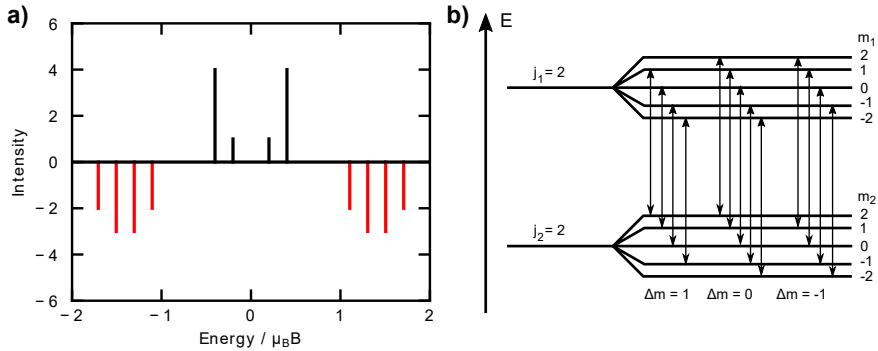


Fig. 5.6: (a) Zeeman pattern for the Ar I transition $1s_5 \rightarrow 2p_6$ for the upper level $j_1 = 2$ and lower level $j_2 = 2$ with $g_1 = 1.305$ and $g_2 = 1.506$ [Kra18]. (b) Possible transitions from the upper to the lower level. (Images taken from [Dic19b])

Coil Number	Current I_0 [A]
1	90
2	30
3	310
4, 5	300
6	310

Table 5.2: Standard currents I_0 for the six magnetic coils at the PSI-2 device.

be caused by the linear background. For both fits the free parameter B gives the magnetic field in T and the obtained values are presented in Tab. 5.3. The error is taken from the fitting routine (lmfit package [New14]). The expected values are calculated under the assumption of a linear correlation between coil current I_i and the maximal magnetic field of 100 mT in the PSI-2 device at $I_i = I_0$ [Kre15]. The linear correlation between magnetic field B and current I is defined by the Biot-Savart law. The obtained data is in a reasonable agreement with the expected values, though the measured values are systematically lower by 15 – 20% compared to the expectations from the Biot-Savart law. First of all, the total magnetic field in PSI-2 plasma is a linear superposition of the magnetic field produced by six coils and certain variation of field strength along the magnetic field is expected. On the one hand, the plasma current could modify the magnetic field so that the resulting field is less than the measurements in the vacuum. On the other hand, other broadening mechanisms ($\mathbf{E} \times \mathbf{B}$ field) could only increase the observed width. Therefore, one expects that the measured field provides the upper limit. Nevertheless, more detailed calculations of Zeeman effect for this line could provide new insights on the remaining discrepancy.

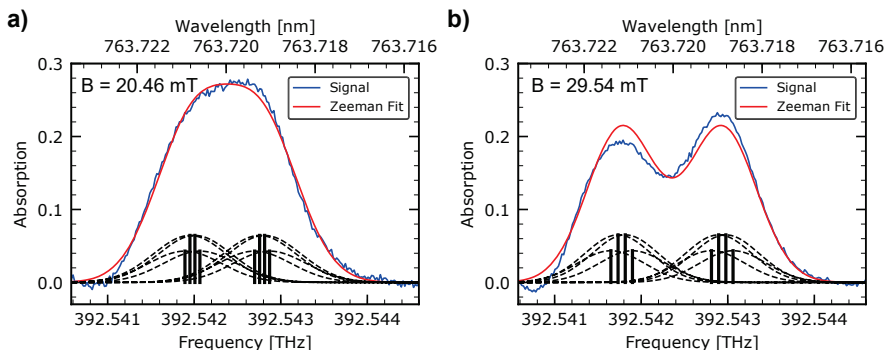


Fig. 5.7: Fit of the eight σ -components of the transition $1s_5 \rightarrow 2p_6$ for two different magnetic field configurations. In (a) $I_{coil,i} = 0.25I_{0,i}$ is shown and in (b) $I_{coil,i} = 0.35I_{0,i}$. On the upper x-axis the vacuum wavelength is used. Note, that the hyperfine structure of Ar is neglected [Wil11].

Zeeman splitting [mT]	Expected [mT]	Coil Current
29.54 ± 1.65	35	$0.35I_0$
20.46 ± 1.03	25	$0.25I_0$

Table 5.3: Comparison between measured magnetic field using the Zeeman splitting and the expected values.

5.4 Determination of the Metastable Density

Beside the determination of the applied magnetic field these spectra could also be used to measure the metastable density of the $1s_5$ level. In order to obtain the metastable density four different measurements were made as described in Sec. 5.1. With these measurements the intensities $I(\nu)$ and $I_0(\nu)$ (Eq. 5.3) and the logarithm $\ln\left(\frac{I_0(\nu)}{I(\nu)}\right)$ are calculated. The background of the absorption signal is not constant but has a linear dependency (Fig. 5.8). The absorption spectrum is fitted (red curve Fig. 5.8 (a)) by only a single Gaussian function described by Eq. 5.13:

$$F(\nu) = m\nu + n + A \exp\left(-\left(\frac{\nu - \nu_{center}}{\sqrt{2}\sigma}\right)^2\right), \quad (5.13)$$

where m is the slope and n is the constant of the background, A is the amplitude, ν_{center} is the center and σ is the width of the Gaussian function (FWHM = $2\sqrt{2\ln(2)}\sigma$). For a magnetic field of 25 mT this approach does not lead to significant errors as the separation induced by magnetic field is relatively small. (Fig. 5.7 (a)). The linear background is subtracted from the fitting function to achieve a background cleaned absorption signal (Fig. 5.8 (b)). The obtained curve is used for integration with the trapezoidal rule [CN03] and the metastable density is calculated using Eq. 5.6. For the calculation the oscillator strength f_{if} of 0.214 is used [Kra18], the absorption length L is assumed to be 40 cm, which is the diameter of the vacuum chamber. The temperature is calculated by the width of the absorption profile (Eq.

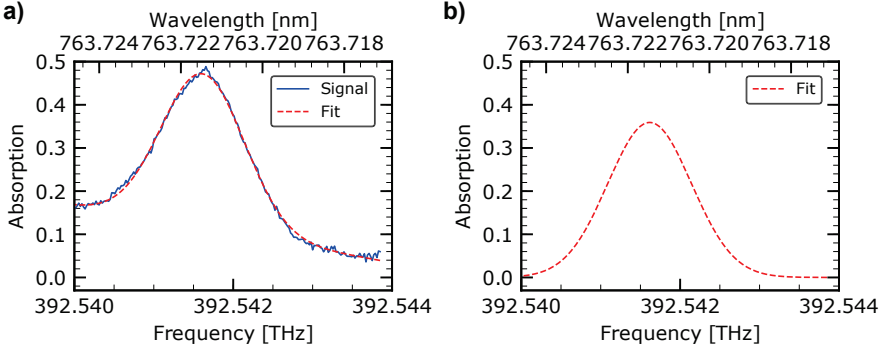


Fig. 5.8: Calculation technique of the metastable density. (a) Fit of a Gaussian function with a linear background $F(\nu) = m\nu + n + A \exp(-((\nu - \nu_{center})/\text{sqrt}2\sigma)^2)$. The signal is obtained with a reduced magnetic field with a coils current of $I_{coil,i} = 0.25I_{0,i}$ and a neutral gas pressure of $p = 3.4 \times 10^{-2}$ Pa. (b) Background cleaned absorption signal for integration to calculate the metastable density.

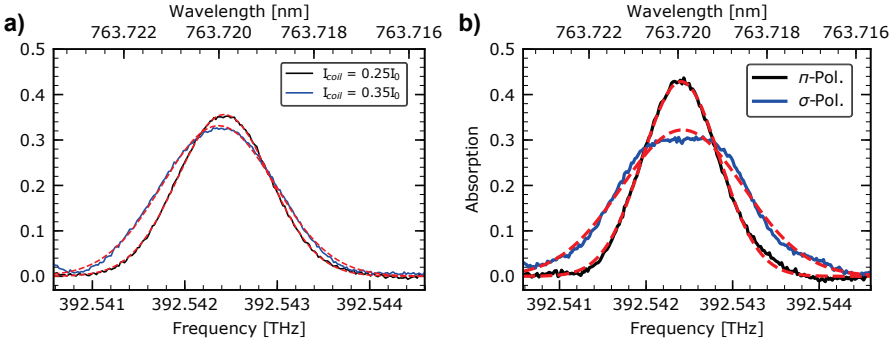


Fig. 5.9: (a) Magnetic field dependence of the absorption spectrum for two configuration of the magnetic field $I_{coil,i} = 0.25I_{0,i}$ and $I_{coil,i} = 0.35I_{0,i}$. The black and blue curve are the experimental data, the red curve is the fit of the absorption spectrum. The measurements were taken in the center of the plasma and it was produced with a gas flux of 40 sccm Ar. The neutral gas pressure was $p = 3.4 \times 10^{-2}$ Pa. (b) Measurement of the polarization of the absorption signal at a magnetic field configuration of $I_{coil,i} = 0.25I_{0,i}$. The plasma was produced with a gas flux of 40 sccm and the neutral gas pressure was $p = 3.4 \times 10^{-2}$ Pa. The measurements were taken in the center of the plasma.

2.41). At a coil current of $I_{coil,i} = 0.25I_{0,i}$ the metastable density is determined to be $1.75 \times 10^9 \text{ cm}^{-3}$ and the gas temperature equals $6 \times 10^{-2} \text{ eV}$. The comparison between the absorption spectra measured at two different magnetic fields is exemplified in Fig. 5.9 (a). With a higher magnetic field ($I_{coil,i} = 0.35I_{0,i}$) the density increases by 30% to around $2.5 \times 10^9 \text{ cm}^{-3}$. The temperature increases by 37% to $9.5 \times 10^{-2} \text{ eV}$. This increase can be explained with a higher electron density (which increases from $1.4 \times 10^{11} \text{ cm}^{-3}$ to $2.4 \times 10^{11} \text{ cm}^{-3}$) due to a higher confinement of the plasma. Furthermore, a shift in the red-shifted region by 60 MHz or 1 m s^{-1} is observed. One of the probable explanations of the observed rotation could be the contribution of Ar^+ ions. Similar to the hot components of the measured Balmer lines, the charge exchange recombination between Ar^+ and Ar could lead to an increase of the rotation. More accurate measurements above and below the equatorial plane of PSI-2 are required to conclude on the observed shift of absorption line. One can conclude that the rotation of the plasma in the PSI-2 device increases with a higher magnetic field. Taking the neutral gas pressure of $p = 3.4 \times 10^{-2} \text{ Pa}$ into account, the Ar density can be calculated to $n_{Ar} = 3.6 \times 10^{12} \text{ cm}^{-3}$. As a consequence, 0.05% are in the metastable state.

The metastable density can also be calculated for the σ and π -component of the Zeeman fit. In Fig. 5.9 (b) it is observed that the π -component is sharper and the amplitude is higher compared to the σ -component. Since the polarization caused by the Zeeman effect affects the line shape but not the intensity, under assumption of statistical population of m sublevels of $J = 2$, the intensities for both components should be equal. In fact according to Fig. 5.6 the derived metastable fraction is independent on the polarization properties of radiation. The measurements remarkably confirm this: the metastable density obtained without polarizers and with polarizers are quite close ($1.75 \times 10^9 \text{ cm}^{-3}$ (without polarizer), $2 \times 10^9 \text{ cm}^{-3}$ (for π -component) and $2.5 \times 10^9 \text{ cm}^{-3}$ (for the σ -component)).

To measure the distribution of metastable atoms in the plasma, a radial profile of the metastable density is obtained by scanning the plasma from the center to edge. The measurements are performed in a pure Ar plasma with a gas flux of 40 sccm. The coil current is adjusted to $I_{coil,i} = 0.25I_{0,i}$. With a Langmuir probe the electron density at the maximum of the plasma profile is determined to be $n_e \approx 2.5 \times 10^{11} \text{ cm}^{-3}$ and the electron temperature to $T_e \approx 4 \text{ eV}$ (shown in Fig. 5.3). The neutral gas pressure in the exposition chamber is $p = 3.4 \times 10^{-2} \text{ Pa}$. The radial scan is performed in the steps of 2 mm, where 0 mm is the center of the plasma. The complete setup is adjusted in the vertical z direction above the equatorial plane of PSI-2 (see Fig. 3.1) by two moving tables (X-MCB2 from Zaber).

The results of the radial scan of the plasma profile are shown in Fig. 5.10. The metastable density is calculated out of the line integrated density assuming an absorption length of $L = 40 \text{ cm}$ is in the range of $n_{Ar^*} \approx 1.75 \times 10^9 \text{ cm}^{-3}$. The sudden decrease of the density between a radial position of 22 mm and 24 mm cannot be explained physically. Neither the electron temperature derived from the Langmuir probe nor the gas temperature measured with TDLAS show any strong variation in this region. After this rapid decrease of the metastable density, the density decreases slower. The trend of a decrease from the center to the plasma etch could be a geometrical effect, because the signal is line integrated. Therefore, the density is assumed to be constant along the complete radial plasma profile, due to a strong dissociation of the metastable atoms in the plasma. The temperature of these atoms

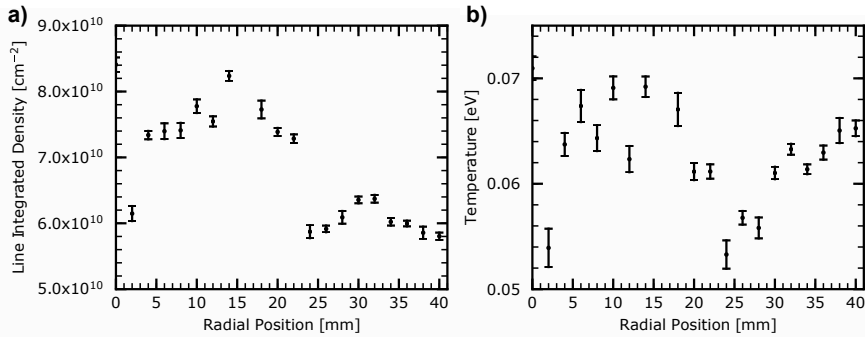


Fig. 5.10: Radial scan of an Ar plasma with a gas flux of 40 sccm using the TDLAS system. The neutral gas pressure was $p = 3.4 \times 10^{-2}$ Pa, the magnetic field is reduced with $I_{\text{coil},i} = 0.25 I_{0,i}$. Note that 0 mm is the center of the plasma. (a) Line integrated metastable density profile of the plasma. (b) Temperature profile of the metastables in the plasma.

is also constant at around $T_{Ar} = 6.4 \times 10^{-2}$ eV (Fig. 5.10). The errors in both graphs are statistical errors. Each measurement presents the mean value of nine single measurements. The statistical error is used in this case because it is greater than the error of the single measurement.

To cross check the experimentally obtained values of the metastable density, the density can also be estimated theoretically. To check if the calculations need to be done in the diffusive regime, the mean free path $\lambda_D = \frac{1}{\sqrt{2}n_{Ar}\sigma_D}$ of the Ar atoms is calculated, where n_{Ar} is the Ar density and σ_D is the cross section of the effective momentum transfer of Ar in the ground state. Using the Ar density of $3.6 \times 10^{12} \text{ cm}^{-3}$ and a cross section of $4 \times 10^{-15} \text{ cm}^2$ [Pit13] the mean free path is calculated to $\lambda_D = 50 \text{ cm}$. The calculation shows that $\lambda_D \gg R$, where $R = L/2 = 20 \text{ cm}$ is the radius of the vacuum chamber. Thus, the motion of the metastable Ar atoms is properly dominated by the thermal motion. The velocity can be calculated to $v_{th} = \sqrt{8k_B T_g / (\pi m_{Ar})}$. With a gas temperature of around 700 K the velocity is determined to $v_{th} = 6 \times 10^4 \text{ cm s}^{-1}$.

To estimate the metastable density the ansatz of Tokar is used [Tok94] where the metastable density is splitted up into two parts $n_+(r)$ (moving away from the center of the plasma) and $n_-(r)$ (moving towards the center of the plasma). The metastable density n_{Ar^*} and the flux of metastable atoms j_{Ar^*} can then be defined the following:

$$n_{Ar^*} = n_+ + n_- , \quad (5.14)$$

$$j_{Ar^*} = (n_+ - n_-)v , \quad (5.15)$$

where v is the velocity of the metastable atoms. For both parts n_+ and n_- a rate equation can be written separately. To simplify the calculation it is made in one dimension. The production of metastable Ar at the used steady-state experimental conditions is mainly caused by electron excitation processes with rate coefficient $k_{e,exc}$. The loss terms in the first approximation are due to electron-impact ionization of metastables with rate coefficient $k_{ion,met}$ and electron impact excitation in the resonant s -states $k_{exc,met}$. The different atomic processes are schematically shown in

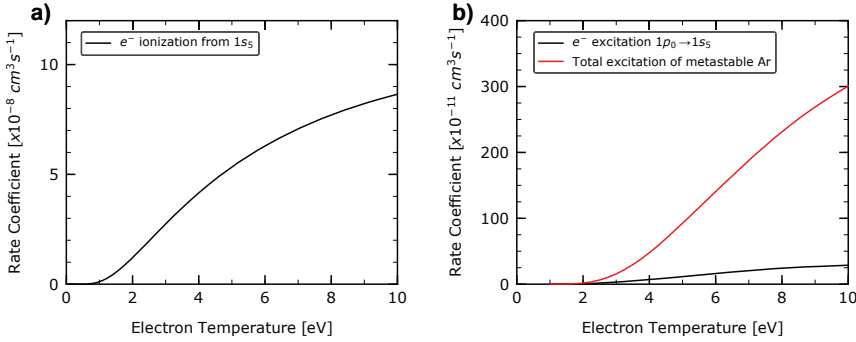


Fig. 5.11: (a) Rate coefficient of the electron impact ionization from the metastable $1s_5$ state. (b) Rate coefficient for the electron impact excitation from the ground state $1p_0$ to the metastable state $1s_5$ (black curve) and the total excitation rate coefficient for metastable Ar (red curve). Both rate coefficient (depicted in black) are calculated out of the cross sections taken from [ZWB14] assuming an Maxwell distribution for the electrons. The total excitation rate coefficient is calculated using the experimental determined cross section from [MN87].

Fig. 5.4. The continuity equations can then be written as:

$$\frac{d}{dx}(n_+v) = \frac{1}{2}n_{Ar}n_e k_{e,exc} - n_en_+(k_{ion,met} + k_{exc,met}), \quad (5.16)$$

$$\frac{d}{dx}(-n_-v) = \frac{1}{2}n_{Ar}n_e k_{e,exc} - n_en_-(k_{ion,met} + k_{exc,met}), \quad (5.17)$$

where n_{Ar} is the Ar density and n_e is the electron density. Note, that the minus sign in Eq. 5.17 is needed because the atoms with density n_- are moving in the opposite direction compared to the atoms with density n_+ . The sum (Eq. 5.18) and the difference (Eq. 5.19) of Eqs. 5.16 and 5.17 can be calculated to:

$$\frac{dj_{Ar^*}}{dx} = n_{Ar}n_e k_{e,exc} - n_en_{Ar^*}(k_{ion,met} + k_{exc,met}), \quad (5.18)$$

$$v \frac{dn_{Ar^*}}{dx} = -n_e(k_{ion,met} + k_{exc,met}) \frac{j_{Ar^*}}{v}. \quad (5.19)$$

Inserting Eq. 5.19 in Eq. 5.18 results in the diffusion equation for the metastable density n_{Ar^*} :

$$-D_m^* \frac{d^2 n_{Ar^*}}{dx^2} = n_{Ar}n_e k_{e,exc} - n_en_{Ar^*}(k_{ion,met} + k_{exc,met}), \quad (5.20)$$

where $D_m^* = v^2/(n_e(k_{ion,met} + k_{exc,met}))$ is the diffusion constant of the metastable atoms, induced by their thermal motion and suppressed by the loss mechanism of the atoms. In the general case, when the rate coefficients are the function of plasma temperature and radius the equation has to be solved numerically. For the estimation of metastable density constant values along the plasma radius are assumed. In this case the solution of Eq. 5.20 can be solved analytically. Using the two boundary conditions $\frac{dn_{Ar^*}}{dx}(x=0) = 0$ and $n_{Ar^*}(x=R=L/2) = 0$ where L is the distance in

which the density of metastable levels reduces to zero. For the calculations $R = 20$ cm is taken as the radius of the chamber. The metastable density equals to:

$$\frac{n_{Ar^*}}{n_{Ar}}(x) = \frac{k_{e,exc}}{k_{ion,met} + k_{exc,met}} \left(1 - \frac{\cosh(x/\lambda)}{\cosh(R/\lambda)} \right), \quad (5.21)$$

where $\lambda = v/(n_e(k_{ion,met} + k_{exc,met}))$ is the mean free path. The first term in Eq. 5.21 at the right hand side provides the maximal density of metastable atoms. The radial dependence of solution is represented by the second term. For the estimation of the metastable density the following values are used: electron density $n_e = 9 \times 10^{10} \text{ cm}^{-3}$, electron temperature $T_e = 2.5 \text{ eV}$ (for n_e and T_e the mean value of the Langmuir profile is taken which is shown in Fig. 5.3), $v = v_{th} = 6 \times 10^4 \text{ cm s}^{-1}$ (calculated for a temperature of 700 K), $k_{e,exc} = 6.4 \times 10^{-11} \text{ cm}^3 \text{ s}^{-1}$ (cross section taken from [MN87] (Fig. 5.11 (b))), $k_{ion,met} = 1.96 \times 10^{-8} \text{ cm}^3 \text{ s}^{-1}$ (cross section taken from [ZWB14] (Fig. 5.11 (a))), $k_{exc,met} = 1.25 \times 10^{-8} \text{ cm}^3 \text{ s}^{-1}$ (sum of all possible resonant excitations [Zhu16]). The rate coefficients are calculated by integrating over the cross section assuming a Maxwellian distribution of the electrons. The cross section given in [ZWB14] for the ionization is fitted using Eq. 5.22 and the one for the excitation given in [MN87] is fitted using the Eq. 5.23:

$$\sigma_{ion,met}(x) = a_0 \frac{\log(x)}{x} + \frac{a_1}{x} + \frac{a_2}{x^2} + \frac{a_3}{x^3}, \quad (5.22)$$

$$\sigma_{e,exc}(x) = \exp\left(-\frac{a_0}{x^{a_1}}\right) \frac{a_2}{x^{a_3}} \left(1 - \frac{1}{x}\right), \quad (5.23)$$

with $x = E/E_a$, where E is the energy of the electrons and E_a is the threshold energy. For [ZWB14] the fitting coefficients are: $a_0 = 5.72$, $a_1 = 20.47$, $a_2 = -35.63$, $a_3 = 15.08$ and for [MN87]: $a_0 = 4.50695$, $a_1 = 2.80547$, $a_2 = 12.6749$, $a_3 = 3.25468$. Beside the excitation cross section by Mason [MN87] also other cross sections for the population of metastable Ar are available in [ZWB14], where only the population of the metastable level by electron excitation from the ground state is calculated. In the work of Mason [MN87] cascade population from the higher s and p-states (with $J = 0$ or $J = 2$) are taken into account, which fits our experimental conditions better than the calculations of [ZWB14]. Therefore, the cross section of Mason is used to calculate the metastable density. The diffusive term according to Eq. 5.20 is larger than the collisional quenching rates with the following consequences for the measurements. First, the population of metastables in the plasma core is a linear function of electron density, which is confirmed by the measurements (Fig. 5.12 (b)). Second, the density of metastable levels should be a rather weak function of plasma radius, which is exemplified in Fig. 5.10. Taking all values into account, the maximum ratio $n_{Ar^*}/n_{Ar}(x = 0)$ can be calculated to 2×10^{-3} , which is 0.2%. This is only a factor of 4 larger compared to the measured metastable density and thus in good agreement with the experiment.

Some further remarks should be made. On the one hand, the collisions of metastable atoms with atoms in the ground state are neglected so that the final diffusion coefficient has to be smaller. This would lead to a reduction of the metastable density. On the other hand the considered excitation coefficient based on the experimental data of [MN87] mostly include the contribution from upper metastable levels as the time-of-flight technique was applied. It is still not clear if for instance the contribution from the resonant levels with $J = 1$ could increase the excitation rate coefficient

significantly, in comparison to the measured results of Mason. The optical (dipole) allowed transition have large excitation cross sections but could also decay faster to the ground state relative to the metastable ones. An accurate collisional radiative modeling is required, but is not done yet though the careful compilation of the data is ongoing [Pit13]. Furthermore, a more detailed comparison with the experiment is required. On the one hand, the measurements were done within the radius of 4 cm only. They have to be extended at least a few cm beyond the plasma radius. It was not possible in this work due to the technical limitations of the PSI-2 chamber. Such measurements are of principle importance for matching the zones where the metastable atoms are created and quenched compared to the zone which includes only geometrical losses, e. g. expected as $1/r$, where r is the plasma radius. Only in this case the correct boundary conditions could be applied. On the other hand, the 1D model has to be extended to a cylindrical geometry and the quenching of metastable argon with collisions with H_2 molecules and atoms have to be considered. The distance L where the population of metastable levels drop significantly is not detected in the experiment on the distance of 4 cm so that measurements have to be extended further from plasma center. The distance $L = 40$ cm could only be considered as an upper limit. Nevertheless, the agreement within a factor of four between the measurements and the estimation is surprisingly good indicating that these measurements can be further used to test the atomic data for Ar I in the low-density limit.

5.5 Absorption Measurements in a H-Ar mixed Plasma

In this section different amounts of H are added into the Ar plasma and the laser absorption is measured for each plasma condition. At the same time the electron density is measured independently with a Langmuir probe. For all measurements the magnetic field configuration was $0.25I_{0,i}$. In Fig. 5.12 (a) the raw absorption signal is plotted against the frequency. With an increasing amount of H the absorption signal decreases and thus the metastable density and the electron density decreases as well (Fig. 5.12 (b)). The electron density decreases from $1.4 \times 10^{11} \text{ cm}^{-3}$ at a H flow of 8 sccm to $6.5 \times 10^{10} \text{ cm}^{-3}$ at 60 sccm which is around a factor of 2. Simultaneously, the electron temperature remains nearly constant at $T_e \approx 3.5 \text{ eV}$ (Fig. 5.13 (b)). The dependence between absorption signal and electron density seems to be linear which is shown by the black dashed line in Fig. 5.12 (b). The fit function is $I(n) = a \cdot n_e + b$, where n_e is the electron density in units of cm^{-3} , $I(n_e)$ the absorption peak signal, $a = 0.17$ and $b = 0.28$. The linear dependency emphasizes that no H_2 molecules can penetrate into the plasma region and quench the metastable Ar atoms. Furthermore, it is observed that a higher amount of H in the plasma leads to a shifted of the minimum of the absorption peak to higher frequencies by 10 MHz for 16 sccm and by 610 MHz for 60 sccm compared 8 sccm hydrogen in the plasma. The reason of this shift is still not clear. One of the possibilities is the contribution of Ar^+ ions or molecular ions ArH^+ , which are affected by the magnetic field.

The impact of the laser beam on the Doppler-shifted signal of the H_α line is measured directly like shown in Fig. 5.14. For the measurements a W mirror is used and a negative potential of -100 V is applied. The plasma is a H-Ar mixed plasma with a

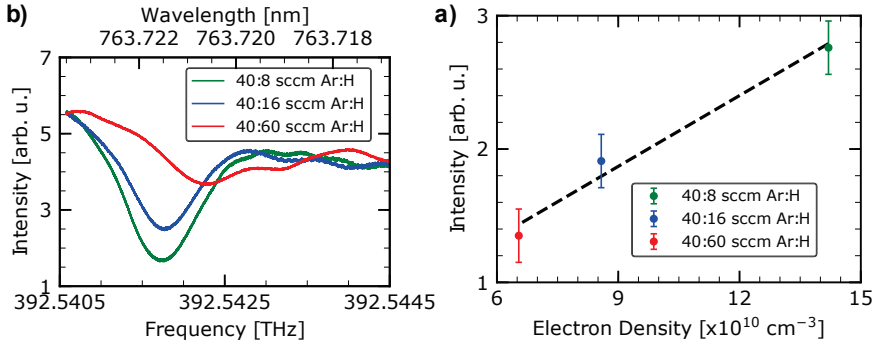


Fig. 5.12: (a) Absorption signal for different types of H-Ar mixed plasmas measured with a polarization filter adjusted for the π -component at the position $z = 0$. Different amounts of hydrogen are depicted in different colors. With increasing hydrogen amount the absorption peak decreases. (b) Electron density n_e plotted against the peak intensity of the absorption signal. The black dashed line is a linear fit of with the function $I(n) = a \cdot n + b$, with $a = 0.17$ and $b = 0.28$.

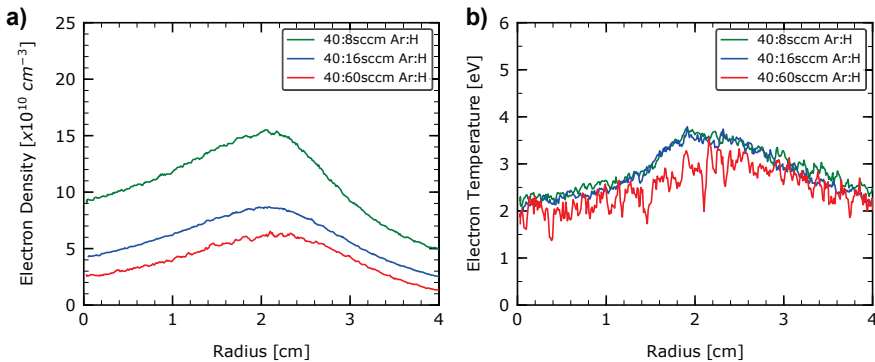


Fig. 5.13: Langmuir probe measurements of at different plasma parameters shown in Fig. 5.12. In (a) the electron density is presented and in (b) the electron temperature.

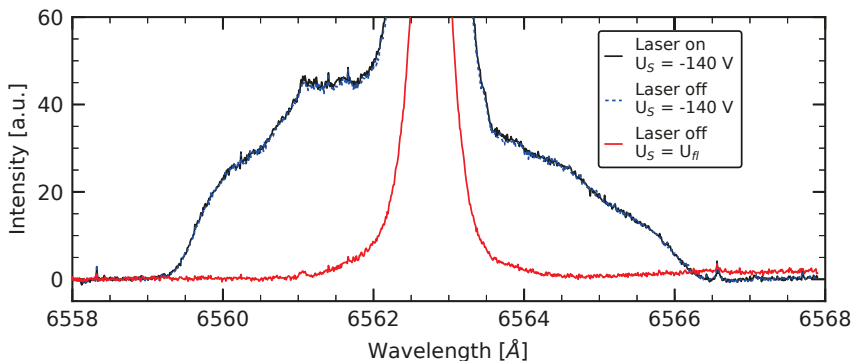


Fig. 5.14: Measurement of the H_α line with the Echelle spectrometer with activated and deactivated laser in a H-Ar mixed plasma with composition 20 : 40 sccm. For the measurements a W mirror is used and a negative potential -100 V is applied. To distinguish better between both measurements, the measurement with deactivated laser is depicted with the dashed line.

composition of 20 : 40 sccm. The laser wavelength is not varied and is hold constant at the transition wavelength of 763.5106 nm. As can be seen in Fig. 5.14 the Doppler-shifted emission can clearly be observed but no difference between both signals is detected either the laser is activated or not (black and blue curve). An influence of the laser on the detected signal is not expected, because the line width of the used laser is too narrow to quench enough metastable atoms in order to observe an impact on the Doppler-shifted signal. To solve this issue, a broadband cw laser could be used in the future, with a line width being comparable to the line width of the transition line.

Beside the impact of the laser beam on the Doppler-shifted emission also the impact of different target potential on the metastable density is investigated. In Fig. 5.15 the metastable density is measured in front of a W target. The plasma is a H-Ar mixed plasma with a composition of 16 : 40 sccm which is already characterized in Fig. 5.13. In the first case the target potential is set to -100 V (black curve) in the second case no external potential is applied to the target (red curve). No difference in the absorption spectrum and thus in the metastable density is found either the target is biased or not. Thus, the metastable density shows no dependence on the energy of the accelerated H^+ ions at the used plasma conditions although the Doppler-shifted emission can be observed.

In the following the findings of this section are concluded. The TDLAS diagnostic provides the first measurements of the density of metastable Ar in a PSI-2 plasma. First of all, the strong impact of the magnetic field on the line shape of the absorption signal was detected. It was confirmed by using polarization measurements of the absorption signal, which provides data on the values of the magnetic field and the gas temperature in the PSI-2 plasma. The density of metastable levels is linearly proportional to the electron density even in the H-Ar mixed plasma. It indicates that the H_2 molecules could not penetrate to the center of the plasma and the diffusion of metastables is the dominant loss term compared to other mechanisms. A radial scan of the absorption signal also confirms this: the profile of metastables varies only

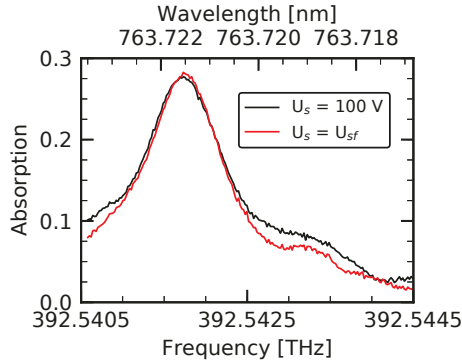


Fig. 5.15: Measurement of the metastable density in front of a W target in a H - Ar mixed plasma with a composition of 16 : 40 sccm. The black curve is the absorption spectrum at a target potential of -100 V and the red curve at floating potential (≈ -25 V).

on the order of 20% and the temperature of Ar remains on the order of 700 – 800 K. The population of metastable is on the order of 0.2 – 0.5% of the ground state. Because of the strong diffusion the Ar metastables could not be confirmed as the possible source of the strong Balmer line emission. The measurements with and without a target do not show any variation of the Balmer lines emission. Thus, the diffusion of metastable levels remains the dominant mechanism in the plasma even in the presence of a target. The metastable levels could be of importance for the $n = 3$ levels of H whereas the H atoms do not necessarily reduce their population. The results open a new way of resolving the problem on the source of Balmer lines emission. By measuring for instance the flux of H^+ ions to the target the resulting emission is proportional to the electron density in case of ground state excitation, whereas the excitation transfer results in a quadratic dependence of the emission of Balmer lines. It seems that in addition to the laser pump-probe technique this is the most promising direction to resolve this problem in the future.

CHAPTER 6

CONCLUSION AND OUTLOOK

The source of emission of fast H atoms at the plasma surface interface is subject of an extensive experimental and theoretical study in plasma discharges. Until now however the substantial difficulties existed by explaining or modeling the observed emission in Grimm type discharges [Ada03; Phe09]. The propagation of emission in front of the targets, angular distribution of incident fast atoms [Phe09] (a “diffusive” distribution instead of the “beam-like”), the strong emission of fast atoms in case of Ar relative to other noble gases [LM93] and the corresponding transition between the density of ions and molecular ions in the presence of Ar are the most prominent examples of experimental findings that could not be explained in frame of the “sheath-collisional model” [Phe09]. This is one of the reasons why in spite of the extensive studies in the past, including atomic modeling, the measurements of Stark broadening in the plasma sheath remain practically the only broad application of the Balmer lines emission. It needs to be mentioned that the emission by fast reflected atoms is also observed in fusion devices, but it has never been considered to build a plasma diagnostic which uses this effect [Sam87; Sam89].

In this thesis the origin of the broad and strong emission of fast H atoms due to plasma-surface interaction in low pressure gas discharges is studied in detail. In fact, the lack of measurements in low density gas discharges was already underlined and this work tries to fill this gap [BGC05]. The new experimental data were obtained at the linear magnetized plasma of PSI-2 (pressure 0.01 – 0.05 Pa, electron temperature 3 – 10 eV, ion temperature 1 – 5 eV, ionization degree of 10^{-3} – 10^{-2}) by exposed targets of different materials (C, W, Fe, Mo, Ti, Pd, Cu, Rh, Sn, Al and Ag) to the plasma. The experimental setup differs considerably from previous studies. In previous works the applied potential was required to ignite the discharge and modification of the bias (negative) potential leads *a priori* to modification of plasma parameters. In the PSI-2 device the situation is essentially different. The applied potential could be varied as requested (–40 . . . –300 V) without modifying the plasma parameters. This experimental setup has two advantages: First, the origin of emission could be studied much more efficiently. Second, the emission could be studied at a kinetic energy of the H atoms where the excitation cross-sections by noble gases (Ar or Kr) is the highest.

At the beginning the experimental data of the emission at a line-of-sight parallel to the target surface or the blue-shifted signal relative to the unshifted wavelength

$\Delta\lambda/\lambda = [-v/c : -v/c \sin(\theta_0)]$ at a line-of-sight at the angle θ_0 relative to the normal are discussed. Here, v is the velocity of the reflected atoms and c is the speed of light. In case of this experiment the angles were 35° , 69° and 90° . It is proven (H^+ colliding with C, Fe, Pd targets) that the Doppler-shifted emission is caused by fast H atoms backscattered from the surface and emitted outside the Debye sheath (Figs. 4.2, 4.3 and 4.4). In this part the experimental data confirm results from the “sheath-collisional” model. At the used experimental conditions the Doppler-shifted emission is the strongest one in a H-Ar mixed plasma. Other mixed plasmas like H-Kr or H-Ne are investigated as well, but with Ar the highest signal-to-noise ratio is achieved. The Doppler-shifted signal with H-Ar is a factor of 3 – 5 stronger than for the combination of H-Kr (Fig. 4.31). Different fluxes of H and Ar were tested as well. It was observed that with composition of fluxes 20 sccm : 60 sccm, 40 sccm : 40 sccm or 60 sccm : 20 sccm for H and Ar the strongest emission signal was obtained. This excludes possible H-H₂ or H-e⁻ interaction as a source of Doppler-shifted emission at given experimental condition. In contrast to the explanations of the observed emission in [Ada03], it is difficult to conclude that the presence of Ar modifies the composition of plasma (H^+ , H_2^+ , H_3^+) dramatically: the shrinking of the wings by factor of 1/2 or 1/3 adding the Ar into the plasma is not observed. After clarifying the best plasma parameters, the dependence of the Doppler-shifted spectrum on the surface potential and material is investigated. It is found that at the floating potential ($U_{sf} = -30$ V) no Doppler-shifted emission can be observed. The emission profile starts to rise at around $U_s = -60 \dots -80$ V. It is the approximate threshold to observe the Doppler-shifted emission at the used plasma parameters. By increasing (absolute values) of negative potential the Doppler-shifted wings become broader but the maximum intensity saturates at around -120 V. Approximately at the same kinetic energy E the emission of former H_2^+ ions (the reflected H atoms with half of the kinetic energy $E/2$) also starts to contribute to the emission profile at lower wavelengths. The maximum energy of the observed neutral atoms has also dependence on the used surface materials, especially at low Z materials. This dependency can be described in a first approximation with a simple binary elastic collision between the surface and the accelerated H^+ and H_2^+ ion. This dependency is tested for C, Al, Ti, Fe, Mo, Rh, Pd, Ag, Sn and W and shows a qualitatively good agreement with experimental data, though the energy loss from the excitation process with Ar is not included (Fig. 4.6). These experiments already show that the origin of the observed Doppler-shifted emission is not the charge-exchange inside the Debye sheath.

The red-shifted emission ($\Delta\lambda/\lambda = [v/c \sin(\theta_0) : v/c]$) at the line-of-sight of 35° could not be described in frame of the “sheath-collisional” model due to the following reason: If the charge-exchange signal from the sheath is missing, the profile should be strongly asymmetrical as the red-shifted emission should be zero. Actually, the asymmetry is observed, but the reduction of the intensity depends on the optical properties of the targets. The fact that in addition to the charge-exchange recombination (the signal from fast atoms approaching the cathode) the reflectance could play the role in the red-shifted emission of Balmer-lines was mentioned in [Ada03; BGC05]. Nevertheless, neither consequent interpretation of the data nor the modeling of the emission at different line-of-sight are taken into account. The resulting red-shifted signal in high density discharges is always a complex superposition between the emission of incident and reflected fast atoms, integration volume of every sort of atoms along the line-of-sight, and finally the Stark effect makes it difficult to separate and model the

contributions in general case. It is exemplified in [COK11] that for the C target the red-shifted signal is higher than the blue-shifted emission. The opposite is observed for another element such as Cu.

In the low density case the situation is extremely simple: *the optical properties of the surface could be extracted directly from the measurements at the angles below $\approx 45^\circ$ without any modeling, only the applied negative potential needs to be known.* At first glance these results seem to be trivial and on the other hand so paradox considering the mainstream of results in high density plasma discharges that the numbers of experimental and theoretical facts supporting this statement and dedicated experimental conditions had to be conducted in this thesis:

- (a) The width of the Debye sheath is a factor of 3 – 10 less than the emission length of H_α line. The Balmer lines from fast atoms could not emit in the Debye sheath, only a weak number of those atoms moving practically parallel to the target. The accurate measurements of the $H_{\alpha,\beta,\gamma}$ lines as a part of this thesis (Sec. 4.7) confirmed it. The appearance of the Balmer lines (target- H_α - H_β - H_γ) is different from high pressure discharges (target- H_γ - H_β - H_α) [VKK96; CKK05] supporting the argument on the absence of signal from atoms approaching the cathode.
- (b) The ratio of the integral for the red and blue-shifted signal for C, W, Fe, Mo, Ti, Al, Cu, Rh, Pd, Sn, Ag and Cu is in very good agreement of (15%) with the reflectance measurements in the laboratory and the theoretical values (Fig. 4.13).
- (c) In case of Cu for instance the ratio between red and blue-shifted signal for the H_α or H_β line is different, and was found in a very good agreement with the theoretical values of reflectance for both wavelengths as well 4.17.
- (d) The shrinking of the energy of fast atoms as a function of material of the target is observed for the blue and red-shifted signal (Fig. 4.5).
- (e) The measurements at the angles close to the Brewster angle for W, Mo and Sn ($\approx 70^\circ$) demonstrated the polarization by light reflectance at metallic surfaces (Figs. 4.20 and 4.21). The red-shifted signal is reduced by a factor of 2 – 3 for the W and Mo target observing the σ -component relative to the π -components of light. A change for the blue-shifted emission is only observed because of the overlap of the blue and red-shifted emission profile. A very weak reduction is observed for the angle of 35° . Such behavior is known from the polarization of light but cannot be explained using polarization mechanisms of emission produced in plasma volume [Fuj99].
- (f) By heating the surfaces of Al and Rh two different effects are observed. First, for the cold Al target the ratio stays practically constant and only reduces on the order of 1 – 2%. By heating the same target the linear drop of ratio is observed as a function of temperature. The further dramatic reduction of red-shifted signal is observed with the increase of sputtering of Al atoms (at the temperatures above 500 K) (Fig. 4.25). For the Rh target no change of the signal is observed during the same heating (Fig. 4.26). The linear dependence for the ratio of the red to the blue-shifted signal in case of Al confirms the elements of the Drude theory for the light reflection in solids [Uji72].

With the knowledge on the origin of the red-shifted component (a-f) one could say that a new kind of DSRM (Doppler-Shifted Reflectance Measurements) diagnostic is developed and tested in this thesis. It allows *in situ* measurements and monitoring of the optical properties of metallic mirrors which makes an additional calibration source or an additional diagnostic port at the plasma chamber to a certain extent unnecessary. The emitted photons can be observed either directly (blue-shifted) or reflected from the surface (red-shifted) (Fig. 4.9). The ratio of both signals determines the spectral total reflectance of the mirror. In this thesis only measurements at the H_α and H_β lines were performed. The stability of the diagnostic makes it especially attractive for ITER applications (Beam – emission spectroscopy operating at the H_α line or the Charge-Exchange Recombination Spectroscopy at the He II line (468 nm) close to the H_β line (486 nm)). The good signal was obtained within tens of seconds. An experiment performed with a Pd mirror and a potential of -100 V has shown that the reflectance of the mirror did not change during two hours of exposition (Fig. 4.14). Obviously, the diagnostic could provide a relatively large amount of spectra before any noticeable change of reflectance is induced due to H-Ar mixed plasma. On the other hand, results have also a rather weak dependence on the absolute value of applied potential as soon as the energy of reflected atoms stay on the order of $80 - 140$ eV (Fig. 4.15).

The measurements of reflectance at large observation angles above 45° already require a modeling of the emission profiles as the blue and red-shifted signal start to overlap. The spectra of W were modeled and the values of polarized reflectance were obtained. The model is tested at the line-of-sight of 35° and at polarization measurements of the same mirror at the 70° LOS (Figs. 4.27 and 4.28). The input parameters were parametrized energy and angular distributions of reflected atoms. The initial data were provided from the TRIM code [Eck91]. The result of the fit shows a quite satisfying agreement with the experimental data. One is able to determine the spectral reflectance in the range of 15 % for the LOS of 35° and for the σ -component at the 70° observation angle. For the π -component the error is larger as it is difficult to measure a very low spectral reflectance using the DSRM diagnostic because of the low signal-to-noise ratio. One of the reasons of such deviation is the absence of the fine-structure component of Balmer-line and instrumental function in the current modeling. At the same time the presented modeling was limited to the description of H^+ ions. The parameters of energy and angular distribution are obtained by fitting the blue and red-shifted components of the fast atoms emission. The distribution function of reflected atoms in the energy range of $50 - 100$ eV is of special interest in the ion-solid interaction as well. The standard ion-beam experiments could not produce ion beams in this low energy range. The available data for the energy and angular distribution starts in the range of a few keV. Instead, the modeling of edge fusion plasma relies on the Monte Carlo codes such as TRIM and these codes are only tested against the ion beam experiments in this high energy range. By modeling the Doppler-shifted emission one obtains a new possibility to evaluate their results at current plasma conditions. It needs to be mentioned that the observation at one line-of-sight provides a number of possible combinations between the energy and the angular distribution (Doppler-shift can be describe by different combinations of angle and velocity or energy of reflected atoms). However, by considering another line-of-sight the number of solutions is reduced and the unique solution can be derived. The found value of power of the angular distribution $\cos^b(\theta_0)$ for H on W at

the energy of 100 eV is $b = 0.2$ (under-cosine distribution). The TRIM code predicts much higher values of 1.5 (over-cosine distribution) for the same energy. It is not clear if such deviations are connected with the calculations itself or for instance with the penetration of H or Ar in W. One should add however that the under-cosine distribution with higher values of $b = 0.6$ ($E_0 = 2$ keV) was found for the blue-shifted reflected atoms in [Phe09] and $b = 0.6$ ($E_0 = 4.5$ keV) in [Lan84] as well. Going to even higher energies, the angular distribution of reflected atoms seems to approach the value of unity ($b = 1$) [VEB80], the current findings of a low b values at the energy of atoms on the order of 100 eV seem to provide a consistent physical picture. By applying the DSRM diagnostic to obtain the optical properties of target one relies only on the experimental evidence that in the presence of Ar the emission of reflected fast atoms is much higher relative to other gases including pure H or D. One considers the excitation of H by Ar atoms in the ground state as the leading atomic process. The increase of emission as a function of the H atoms energy seems to confirm this generally accepted statement. At the same time measurements in He, Ne or Xe confirm the weak excitation cross sections measured by van Zyl [VGN83; VGN85; VNG86]. The most conflicting result appears using the measurements with Kr. According to the data [VNG86] the excitation cross-section is of the same order of magnitude and one expected that the strong emission should appear also in H-Kr plasmas. However, it is not the case either in PSI-2 (the signal is a factor of 3 – 5 less compared to a H-Ar plasma (Fig. 4.31)) or in other experiments [LM93]. What could be other sources of excitation assuming that the measured atomic data for Kr are correct?

It was shown in this work that Ar^+ ions could be excluded. By excitation of reflected atoms by ions and not by atoms the radial dependence of emission in PSI-2 plasmas should behave as $n_e^2(r)$ as the density of reflected atoms is proportional to the density of H ions. However, it is shown in Fig. 4.18 that the emission behaves as $n_e(r)$ supporting the theory of excitation by atoms and not by ions. Also the ionization degree is too low so that the excitation by ions could be comparable with excitation by atoms. The energy diagram of excited state of H and other noble gases demonstrates one feature favoring Ar atoms relative to other noble gases: the metastable (long-living states) of Ar are lower only by about 0.5 eV lower relative to the excited $n = 3$ levels of H. At the same time the broadening of the L_α line in the afterglow plasma demonstrated that even higher energy difference between $n = 2$ levels of H atoms and the metastable levels of Ar (≈ 1.2 eV) could be efficiently transferred into the kinetic energy of H atoms [CM77; Cly80]. Thus, the measurements of metastable levels of Ar are required to exclude the impact of metastable Ar on the observed emission. This work only focuses on population measurements of the $1s_5(J = 2)$ level of Ar.

To answer this question the TDLAS (Tunable Diode Laser Absorption Spectroscopy) diagnostic was built up at the PSI-2 device to measure the Ar metastable density ($1s_5 \rightarrow 2p_6$ at 763.51 nm) and to investigate the quenching of metastable states by fast hydrogen atoms. The measurements were successful only partially. One succeeded to measure the density of metastable levels as a function of plasma radius, as function of concentration of Ar and H, the temperature of Ar atoms and also the magnetic field in the plasma of PSI-2. For instance, it was shown that the Zeeman effect provides the splitting of the levels being higher or comparable with the Doppler broadening of Ar I lines. For the first time the magnitude of magnetic

field was derived in PSI-2 during plasma operation using the σ and π polarization components. The measurements were possible only till $B = 0.05$ T due to the laser operation conditions. The results demonstrated the reduction on the order of 15 – 20 % relative to the expected values in the vacuum. At the same time the gas temperature was found on the order of 0.5 – 0.07 eV confirming the results from high resolution spectroscopy. Finally, one observes practically no or extremely weak variation within 20 % of measured density of metastable levels on the radial scan of 4 cm in the PSI-2. The density of metastable levels was estimated on the order of $1.75 \times 10^9 \text{ cm}^{-3}$ compared to the gas density of Ar of $3.6 \times 10^{12} \text{ cm}^{-3}$ (0.05 %). For the calculation an absorption length on the order of $L = 40$ cm (diameter of PSI-2 chamber) is assumed, which could not be covered by the measurements to perform the Abel inversion. The fact that practically no or weak variation of metastable levels in PSI-2 plasma as a function of radius is observed, confirms the data [Mar18] on the one hand. On the other hand, it means that the ratio of metastables to ground state remains constant so that they could contribute to the Doppler-shifted emission. Also, by inserting and biasing the target no change either in population of metastables or in emission signal was detected: the quenching of metastable by fast atoms is expected to be negligibly small relative to diffusion or other depopulation mechanisms (electron excitation to resonance levels or ionization). Nevertheless, one of the results the TDLAS measurements provided is of special interest for future studies. It is shown that the density of metastable in PSI-2 plasma depends linearly on electron density by mixing Ar with H. Obviously, the molecules of H_2 do not penetrate into the emission volume to quench the metastable levels. Unfortunately, the ions ratio (Ar^+ to H^+) is changed by any modification of the gas flows between Ar and H. By using the latter experimental fact and by measuring the relative ratio between ions in PSI-2 plasma using for instance ion-mass spectrometer and emission of reflected atoms one should be able to answer this question: emission of atoms are caused by excitation or by excitation transfer. Other approaches seem to be less promising: the line profile of Ar I metastable levels is too broad to be measured using for instance pump-probe lasers as the steady state operation has to be guaranteed. Summarizing, one should underline that the success of operation of a new DSRM diagnostic in low density plasma is the major result of this thesis because it has a rather weak dependence on any of the given problems of atomic physics. These problems could not be resolved in this thesis completely. No doubt that the DSRM diagnostic, being currently the only available technique to provide the optical properties of solids contacting the plasma in the absence of additional light sources, will find broad applications in fusion or other laboratory plasmas and stimulate the discussion on low energy (10 – 100 eV) atom-atom collisions of excitation and excitation transfer.

LIST OF FIGURES

2.1	Schematic of the potential drop in the Debye sheath. The plasma potential is denoted with U_p , the surface potential with U_s . In the sheath positive charged ions A^{Z+} are accelerated, neutralized at the surface and backscattered as fast atoms A_{fast}	5
2.2	Schematic of the different channels for fast H atom production at the surface with different types of accelerated ions.	6
2.3	TRIM calculations made by D. Reiter for H on W with an energy of $E_0 = 120$ eV. The data is fitted using the function $f(x) = A(1 - x)/(2 - x_0 - x)^\beta$, with $A = 1.02 \times 10^4$, $x_0 = 0.91$, $\beta = 2.57$ and $x = E/E_0$	8
2.4	The distribution functions of the incoming ions and the backscattered atoms are shown schematically. Note that both distribution functions differs from each other because of the backscattering process.	9
2.5	The emission profiles for two exemplary line-of-sights are schematically shown. For a line-of-sight parallel to the surface a symmetrical emission profile is expected. For every other angle the emission profile is expected to be unsymmetrical with regard to the unshifted wavelength.	10
2.6	(a) Energy scheme of the hydrogen atoms for the first five quantum numbers $n = 1..5$. (b) Scheme of the fine splitting structure and the possible transitions of the hydrogen atom at the H_α line.	10
3.1	Cross section of the PSI-2 device (with courtesy of A. Terra, FzJ). The annotations are added by the author.	19
3.2	Langmuir probe measurement of a H plasma with a gas flux of 95 sccm. In (a) the electron density n_e , in (b) the electron temperature T_e and in (c) the plasma potential U_p are depicted. Note, a negative radius means that the langmuir probe is moving into the plasma, a positive means the probe is moving out of the plasma.	19
3.3	3D model of the side manipulator. Both models are created and rendered using the software Blender 3D [Ble18].	20

3.4 3D models of the two target holders used on the axial manipulator. In (a) the cooled target holder and in (b) the heated target holder are shown. With the MACOR separators the sample is thermally decoupled from the cooled cooper basement. Both models are created and rendered using the software Blender 3D [Ble18]. 21

3.5 Scheme of the used high resolution Echelle spectrometer (HRES). The light coming from the fiber is focused on the entrance slit of the spectrometer. In front of the entrance slit a interference filter is positioned to filter out all unnecessary wavelengths of the light. In the spectrometer the light is reflected from a mirror and focused on an Echelle grating. The grating separates the light with respect to the wavelength and reflects it back through the lens on an EMCCD chip. 22

3.6 Measurement of the calibration lamp. The left peak is the D_α line and the right is the H_α line. The fine structure of both peaks can be observed in this spectrum. The colored functions are the fits of both spectral lines. 24

3.7 H_α line measured with the high resolution Echelle spectrometer at a LOS of 35° . The H flux was 85 sccm and the neutral gas pressure was $p = 4.7 \times 10^{-2}$ Pa. The electron density was $n_e = 3.5 \times 10^{11} \text{ cm}^{-3}$ and the electron temperature was $T_e = 11 \text{ eV}$. To fit the spectral line two functions are used for the hot (red curve) and the cold (blue curve) component. Each function is the sum of seven single Voigt profiles for each line of the fine structure of hydrogen. The theoretical fine structure lines are shown as thin lines in the center of the spectrum and are taken from the NIST database [Kra18]. 25

4.1 Langmuir probe measurement for two different plasma conditions with two different gas flows namely 40 : 40 sccm and 80 : 80 sccm. In (a) the electron density n_e , in (b) the electron temperature T_e and in (c) the plasma potential U_p is depicted. Note, a negative radius means that the langmuir probe is moving into the plasma, a positive means the probe is moving out of the plasma. The image is mainly taken from [Dic18a] 28

4.2 Scan of the target potential between -30 V and -220 V for a Pd sample. The different colors denote the different applied potentials. For the experiment a gas flow of 40 : 40 sccm H:Ar and the radial manipulator was used. Both spectra were measured for H_α . (a) Spectra measured at an angle of 90° between surface normal of the target and line-of-sight are shown. (b) Spectra measured at 35° 30

4.3 Scan of the target potential between -30 V and -220 V for a Fe sample. The different colors denote the different applied potentials. For the experiment a gas flow of 40 : 40 sccm H:Ar and the radial manipulator was used. Both spectra were measured for H_α . (a) Spectra measured at an angle of 90° line-of-sight are shown. (b) Spectra measured at 35° . 31

-
- 4.4 Scan of the target potential between -30 V and -220 V for a C sample. The different colors denote the different applied potentials. For the experiment a gas flow of $40 : 40\text{ sccm H:Ar}$ and the radial manipulator was used. Both spectra were measured for H_α . (a) Spectra measured at an angle of 90° line-of-sight are shown. (b) Spectra measured at 35° . 32
- 4.5 Measured spectra for different target materials. The different energy ranges are shown and the colored areas represent the areas in which the integral for the reflectance is calculated. Blue for the blue-shifted direct emission and red for the red-shifted reflected emission. The error bars are the uncertainties for determine the energy of the spectrum and are the result of the instrumental uncertainty which is $\approx 5\text{ px}$. The dashed black line represents the applied target potential of -100 V . In the upper right corner of each graph the measured element and in brackets its atomic number is given. All spectra were measured using the radial manipulator except of the measurements of Mo and W. For this spectra the axial manipulator was used. 35
- 4.6 Normalized energy E_m^p/eU_s versus the atomic mass for different target materials, where U_s is the applied target potential. The experimental data is shown in black points and the dashed black curve is the calculation using Eq. 2.4 [AFM07]. 36
- 4.7 Scheme of an ellipsometry setup. Emission from the light source is polarized with a polarizer and sent onto the sample surface. Afterwards the polarized light is reflected from the sample surface, analyzed in a second polarizer and measured with a detector. 38
- 4.8 (a) Setup to measure the spectral reflectance of a target with an Ulbricht sphere. (b) Spectra measured with (black dashed curve) and without target (black curve). The difference between both spectra is defined as the spectral reflectance of the sample. 38
- 4.9 (a) Top: Scheme of the Doppler-shifted emission of a mono-energetic atom with velocity v moving in the detector direction. Bottom: Measured Doppler-shifted spectrum (blue and red peak). The black dashed line is the emission at a velocity $v = 0$. (b). Top: Geometrical conditions at an observation angle of Θ_0 . Bottom: Emission profile of the Doppler-shifted emission. The blue-shifted emission profile is in the interval of $[\lambda_{b,min}, \lambda_{b,max}]$ and the red-shifted emission $[\lambda_{r,min}, \lambda_{r,max}]$. The two emission profiles are overlapping depending on the observation angle Θ_0 . The shape is determined by the angular and energy distribution function of the fast atoms [EB83]. (Image taken from [Dic18a]) 39
- 4.10 Scheme of the reflection and transmission of an incoming wave with wave vector \mathbf{k}_e , the reflected wave has the wave vector \mathbf{k}_r and the transmitted wave \mathbf{k}_f . The angles are measured from the surface normal \mathbf{N} . The incoming angle is named α , the reflectance angle α' and the transmittance angle β . The refractive index of first material is n_1 and of the second material $n_2 > n_1$ 41
- 4.11 Geometrical condition to derive the Fresnel formulas to calculate the reflectance of the surfaces. 41
-

- 4.12 Schematic picture of the polarization of reflected light at an ideal mirror (a) and a completely diffusive mirror (b). (a) If the surface is an ideal mirror, the light is polarized if the angle of incidence is the Brewster angle α_B . The theory of polarization by reflectance assumes only one plain of incidence and thus only one direction of dipole radiation. (b) The assumption of only one plain of incidence is not applied for a diffusive surface. In this picture the surface consists of many plains of incidence. As a result no preferable direction of polarization exists anymore and thus the reflected light is unpolarized. 43
- 4.13 Experimental reflectance compared to values taken from the literature. The values for Ag, Fe, Pd, W, Mo, Ti and Cu are taken from [WGA09], C data taken from [Que85], Al data taken from [Rak98], Rh data from [WOL77] and Sn data taken from [GM64]. It should be noted that there is no literature value for Sn available at the wavelength of 656 nm. The value given in this plot is taken for 730 nm. The error bars for the reflectance data is calculated using Eq. 4.4. For the red points the spectral reflectance of the mirror is measured in the lab with an Ulbricht sphere before plasma exposure. 44
- 4.14 Temporal evolution of the experimental determined reflectance of a Pd mirror during 2 h. The gas flux was adjusted to 80 : 80 sccm, the surface potential was -100 V and the radial manipulator was used to make this experiment. The red data points at the beginning and the end are reflectance measurements before and after plasma exposure outside the vacuum chamber using an Ulbricht sphere. The dashed line is the reflectance taking from *Werner et al.* [WGA09]. 45
- 4.15 Measurement of the spectral reflectance for a Pd, Fe and C mirror at different surface potentials. The measurements started at $U_s = -80$ V and the potential was increased to $U_s = -220$ V. The dashed line are the reflectance values taken from literature. For Pd and Fe the values where taken from *Werner et al.* [WGA09] and for C from *Querry* [Que85]. (Image taken from [Dic18a]) 46
- 4.16 Integral I_b of the blue-shifted component is plotted versus the applied potential. For this experiment Pd, Fe, and a C mirror was used and the target potential was started at -80 V and then increased in steps of -20 V to -220 V. The dashed line is the fitted function $I_b = a + b\sqrt{eU_s}$ to the data, where a and b are fitting coefficients, e the elementary charge and U_s the applied surface potential. The fitting function assumes the relation of Eq. 4.22. (Image taken from [Dic18a]) 47
- 4.17 Measured spectra of a Cu mirror in H-Ar mixed plasma with a gas flux of 40 : 40 sccm. The surface potential for both measurements was $U_s = -120$ V. Both spectra are normalized to the maximum of the passive Balmer line. (a) Spectra measured for the H_β line at 486 nm. The reflectance is calculated in the colored areas. Blue for the blue-shifted component and red for the red-shifted component. (b) Spectra measured using the same Cu mirror at the position of the H_α line at 656 nm. The literature values of the reflectance of Cu are taken from *Werner et al* [WGA09]. 48

-
- 4.18 Radial profile scan of a standard H-Ar mixed plasma with a gas flux of 40 : 40 sccm combined with a Langmuir probe measurement of the same plasma. A Pd mirror with an applied potential of $U_s = -100$ V was used. The black dots show the measured electron density n_e using a Langmuir probe. The red data points are the measured integral of the blue-shifted component. The measured profiles of the DSRM diagnostic and the Langmuir probe are aligned at their maxima. . . . 49
- 4.19 Schematic how the light emitted by fast atoms is polarized at the metallic surface. The two polarization directions s and p are depicted in different colors, blue for s-polarization and red for p-polarization. The light emitted by the excited H atom (yellow sphere) moving with a velocity \mathbf{v} away from the mirror surface consists of both polarization directions. At the surface the light is interacting with the mirror surface (this can be calculated using the Fresnel equations Eqs. 4.18 and 4.19). At the Brewster angle only s-polarized light is reflected back from the surface. Image is created and rendered using the software Blender 3D [Ble18]. 51
- 4.20 Polarization measurement of a Mo mirror. The applied potential was -100 V for (a) and -120 V for (b). The gas flux was 80 : 80 sccm for the H-Ar mixed plasma and the axial manipulator was used for this experiments. For both experiments a polarization filter was used before the light, emitted in the plasma, is coupled into the fiber to the spectrometer. (a) Measured spectra at an angle of 35° . (b) Measured spectra at an angle of 75° . (c) Theoretical curve calculated using the Fresnel equations (Eqs. 4.18 and 4.19) with the data from *Werner et al.* [WGA09]. The color code is similar to (a) and (b) and the black curve is the total reflectance $R = (R_s + R_p)/2$ 52
- 4.21 Polarization measurement of a W mirror. The applied target potential was -120 V. The gas flux was adjusted to 40 : 40 sccm for the H-Ar mixed plasma. The axial manipulator was used for the measurements. For both experiments a polarization filter was used before the light, emitted in the plasma, is coupled into the fiber to the spectrometer. (a) Measured spectra at an angle of 70° . S-polarization is depicted in red and p-polarization in blue. (b) Theoretical curve calculated using the Fresnel equations (Eqs. 4.18 and 4.19) with the data from *Werner et al.* [WGA09]. The color code is similar to (a) and (b) and the black curve is the total reflectance $R = (R_s + R_p)/2$ 53
- 4.22 Polarization measurement of a Sn mirror. The applied potential was -120 V for (a) and -100 V for (b). The gas flux was 80 : 80 sccm for the H-Ar mixed plasma and the axial manipulator was used for both experiments. For both experiments a polarization filter was placed in the optical path before the light, emitted in the plasma, is coupled into the fiber. (a) Measured spectra at an angle of 75° of a polished Sn mirror. In the upper left corner a picture of the measured mirror is shown. (b) Measured spectra at an angle of 75° of the same Sn mirror after heating up and sputtering the surface. In the left upper corner the investigated mirror with the degenerated surface is shown. 55
-

4.23	Theoretical calculated temperature dependence of the reflectance of the metals Ag, Al, Au and Cu at a wavelength of 690 nm. The data is digitized and replotted from [Uji72].	56
4.24	Measured spectra of an Al mirror. For both experiments the gas flux was adjusted to 40 : 40 sccm and the applied surface potential was $U_s = -100$ V. In both experiments the Al mirror was exposed for 1 h to the plasma. (a) For this experiment the radial manipulator was used and the mirror temperature was hold constant at about 300 K during the exposition. (b) For this experiment the axial manipulator was used and the mirror was heated up to about 600 K during the exposition.	57
4.25	(a) Comparing the temperature dependence of the reflectance of a cooled (blue data points) and a heated mirror (red data points) with the theoretical calculations of Ujihara [Uji72]. (b) Comparing the reflectance dependence of the heated mirror (red data points) with the measured temperature curve (black data points) and the calculated integral of two spectral lines of Al at 394.40 nm and 396.15 nm (green data points). (Images taken from [Dic18b])	58
4.26	Temperature stability measurement of a polycrystalline Rh mirror. The mirror was heated up to around 650 K in 27 min by plasma heating. The surface potential was -100 V and the gas flux was adjusted to 40 : 40 sccm. The exposure time was set to 30 s. For this experiment the axial manipulator was used.	60
4.27	Experimental spectrum of H_α using a W mirror (black dots) measured under an observation angle of 35° and fitted with the developed model (red curve). For the experiment the target potential was set to -120 V. The gas flux was adjusted to 40 : 40 sccm and the neutral gas pressure was 4.4×10^{-2} Pa.	62
4.28	Experimental data of a W mirror (black dots) measured under an observation angle of 69° and fitted with the developed model (red curve). For the experiment the surface potential was set to -120 V. The gas flux was adjusted to 40 : 40 sccm and the neutral gas pressure was 4.4×10^{-2} Pa. (a) Spectrum of the measurement of R_S . (b) Spectrum of the measurement of R_P	63
4.29	H_α spectrum obtained in different mixed plasmas of H-Ar (a), H-Kr (b) and H-Ne (c). For all measurements a Pd mirror was used with a negative target potential of -100 V. The gas flux was varied under the condition that the neutral gas pressure in the exposition chamber stays constant. To make the spectra comparable the measured signal of each spectrum is divided by the exposure time of the camera.	65
4.30	Langmuir probe measurement of the H-Ar (40 : 40 sccm) and H-Kr (55 : 15 sccm) mixed plasmas. The neutral gas pressure was $p = 3.9 \times 10^{-2}$ Pa and $p = 4.1 \times 10^{-2}$ Pa, respectively. In (a) the electron density and in (b) the electron temperature is shown.	66

4.31	Comparison of the H_{α} emission spectra of three different gas mixtures, namely H-Ar, H-Kr and H-Kr. The used composition and gas flow of the measurement is given in the graphs legend (the unit is sccm). For all measurements a Pd mirror was used and the target potential was -100 V neutral gas pressure in the exposition chamber was $3.9 \times 10^{-2}\text{ Pa}$ for Ar, $4.1 \times 10^{-2}\text{ Pa}$ for Kr and $2.6 \times 10^{-2}\text{ Pa}$ for the measurement with Ne.	66
4.32	Cross sections for the ground state excitation of H to the state $n = 3$ for He, Ar, Ne, Kr, Xe. The data is digitalized and taken from [Van80] for Ar, from [VGN83] for He, from [VGN85] for Ne and from [VNG86] for Kr and Xe.	67
4.33	Potential curve for H and Ar. The data is digitalized and taken from [VG80].	67
4.34	Grotian diagram of H, Ar and Kr. The first three excited levels of H and the metastable states of Ar and Kr are shown. The data is taken from the NIST database [Kra18].	67
5.1	Schematic picture of a TDLAS system to measure the density of a species.	70
5.2	Schematic of the TDLAS setup at PSI-2.	71
5.3	Langmuir probe measurements of the Ar plasma used for the TDLAS measurements at PSI-2. The neutral gas pressure was $p = 3.4 \times 10^{-2}\text{ Pa}$. In (a) the electron density is presented and in (b) the electron temperature.	72
5.4	Grotian diagram of Ar showing the ground state, the first 14 excited levels in Paschen notation and the ionization limit taken from NIST database [Kra18]. The transition from $1s_5$ to $2p_5$ is pumped by the laser to measure the metastable Ar density (shown with the red arrow). The black arrows represent the production channel (electron excitation) and the dashed arrows the considered loss channels (electron excitation in resonant states, electron impact ionization and not shown here diffusion) for the $1s_5$ state.	73
5.5	Schematic of the x-axis conversion of the oscilloscope using the data measured by the wavemeter. The spectrum is measured in an Ar plasma with a gas flow of 40 sccm. The plasma characteristics are shown in Fig. 5.3. (a) Data obtained by the wavemeter during the voltage sweep of the piezo crystal. (b) Voltage characteristic of the piezo crystal and absorption signal measured with the photo diode and the Lock-in amplifier visualized with the oscilloscope. (c) The same absorption signal like in (b), but plotted with the converted x-axis.	75
5.6	(a) Zeeman pattern for the Ar I transition $1s_5 \rightarrow 2p_6$ for the upper level $j_1 = 2$ and lower level $j_2 = 2$ with $g_1 = 1.305$ and $g_2 = 1.506$ [Kra18]. (b) Possible transitions from the upper to the lower level. (Images taken from [Dic19b])	77

5.7 Fit of the eight σ -components of the transition $1s_5 \rightarrow 2p_6$ for two different magnetic field configurations. In (a) $I_{coil,i} = 0.25I_{0,i}$ is shown and in (b) $I_{coil,i} = 0.35I_{0,i}$. On the upper x-axis the vacuum wavelength is used. Note, that the hyperfine structure of Ar is neglected [Wil11]. 78

5.8 Calculation technique of the metastable density. (a) Fit of a Gaussian function with a linear background $F(\nu) = m\nu+n+A \exp(-((\nu - \nu_{center})/\sqrt{2}\sigma)^2)$. The signal is obtained with a reduced magnetic field with a coils current of $I_{coil,i} = 0.25I_{0,i}$ and a neutral gas pressure of $p = 3.4 \times 10^{-2}$ Pa. (b) Background cleaned absorption signal for integration to calculate the metastable density. 79

5.9 (a) Magnetic field dependence of the absorption spectrum for two configuration of the magnetic field $I_{coil,i} = 0.25I_{0,i}$ and $I_{coil,i} = 0.35I_{0,i}$. The black and blue curve are the experimental data, the red curve is the fit of the absorption spectrum. The measurements were taken in the center of the plasma and it was produced with a gas flux of 40 sccm Ar. The neutral gas pressure was $p = 3.4 \times 10^{-2}$ Pa. (b) Measurement of the polarization of the absorption signal at a magnetic field configuration of $I_{coil,i} = 0.25I_{0,i}$. The plasma was produced with a gas flux of 40 sccm and the neutral gas pressure was $p = 3.4 \times 10^{-2}$ Pa. The measurements were taken in the center of the plasma. 79

5.10 Radial scan of an Ar plasma with a gas flux of 40 sccm using the TDLAS system. The neutral gas pressure was $p = 3.4 \times 10^{-2}$ Pa, the magnetic field is reduced with $I_{coil,i} = 0.25I_{0,i}$. Note that 0 mm is the center of the plasma. (a) Line integrated metastable density profile of the plasma. (b) Temperature profile of the metastables in the plasma. 81

5.11 (a) Rate coefficient of the electron impact ionization from the metastable $1s_5$ state. (b) Rate coefficient for the electron impact excitation from the ground state $1p_0$ to the metastable state $1s_5$ (black curve) and the total excitation rate coefficient for metastable Ar (red curve). Both rate coefficient (depicted in black) are calculated out of the cross sections taken from [ZWB14] assuming an Maxwell distribution for the electrons. The total excitation rate coefficient is calculated using the experimental determined cross section from [MN87]. 82

5.12 (a) Absorption signal for different types of H-Ar mixed plasmas measured with a polarization filter adjusted for the π -component at the position $z = 0$. Different amounts of hydrogen are depicted in different colors. With increasing hydrogen amount the absorption peak decreases. (b) Electron density n_e plotted against the peak intensity of the absorption signal. The black dashed line is a linear fit of with the function $I(n) = a \cdot n + b$, with $a = 0.17$ and $b = 0.28$ 85

5.13 Langmuir probe measurements of at different plasma parameters shown in Fig. 5.12. In (a) the electron density is presented and in (b) the electron temperature. 85

5.14	Measurement of the H_{α} line with the Echelle spectrometer with activated and deactivated laser in a H-Ar mixed plasma with composition 20 : 40 sccm. For the measurements a W mirror is used and a negative potential -100 V is applied. To distinguish better between both measurements, the measurement with deactivated laser is depicted with the dashed line.	86
5.15	Measurement of the metastable density in front of a W target in a H-Ar mixed plasma with a composition of 16 : 40 sccm. The black curve is the absorption spectrum at a target potential of -100 V and the red curve at floating potential (≈ -25 V).	87

LIST OF TABLES

3.1	Typical plasma parameters of the PSI-2 device taken from [Kre15]. . .	19
3.2	Characteristics of the HRES.	23
4.1	Comparison of fitted reflectance values and data taken from [WGA09] and [Min17].	62
4.2	Fit parameters of the different fitted spectra.	62
4.3	Plasma parameters of the different gas configurations in Fig. 4.31. . .	66
5.1	Electronic configuration and Paschen notation shown for the lowest excited levels of Ar [Kra18].	72
5.2	Standard currents I_0 for the six magnetic coils at the PSI-2 device. . .	77
5.3	Comparison between measured magnetic field using the Zeeman split- ting and the expected values.	78

BIBLIOGRAPHY

- [AB72] H. Ahmed and A. N. Broers. “Lanthanum Hexaboride Electron Emitter”. In: *Journal of Applied Physics* 43.5 (1972), pp. 2185–2192. DOI: 10.1063/1.1661472. eprint: <https://doi.org/10.1063/1.1661472>. URL: <https://doi.org/10.1063/1.1661472>.
- [Ada03] M. R. G. Adamov, B. M. Obradovic, M. M. Kuraica, and N. Konjevic. “Doppler spectroscopy of hydrogen and deuterium Balmer alpha line in an abnormal glow discharge”. In: *Plasma Science, IEEE Transactions on* 31.3 (2003), pp. 444–454. ISSN: 0093-3813.
- [AFM07] T. L. Alford, L. C. Feldman, and J. W. Mayer. *Fundamentals of Nanoscale Film Analysis*. Springer Verlag, 2007.
- [AKA95] J. M. Ajello, I. Kanik, and S. M. Ahmed. “Line Profile of H Lyman α from dissociative excitation of H_2 with application to Jupiter”. In: *J. Geophys. Res.* 100 (1995), pp. 26, 411. DOI: 10.1029/95JE02360.
- [AKK04] M. G. Adamov, M. M. Kuraica, and N. Konjević. “Intensity dependence of hydrogen Lyman alpha and Balmer alpha lines upon cathode material of an abnormal glow discharge”. In: *The European Physical Journal D - Atomic, Molecular, Optical and Plasma Physics* 28.3 (May 2004), pp. 393–398. ISSN: 1434-6079. DOI: 10.1140/epjd/e2003-00324-1.
- [BA08] J. N. Brooks and J.P. Allain. “Particle deposition and optical response of ITER motional Stark effect diagnostic first mirrors”. In: *Nuclear Fusion* 48.4 (2008), p. 045003. URL: <http://stacks.iop.org/0029-5515/48/i=4/a=045003>.
- [Bal17] M. Balden, S. Elgeti, M. Zibrov, K. Bystrov, and T. W. Morgan. “Effect of the surface temperature on surface morphology, deuterium retention and erosion of EUROFER steel exposed to low-energy, high-flux deuterium plasma”. In: *Nuclear Materials and Energy* 12 (Aug. 2017), pp. 289–296. DOI: 10.1016/j.nme.2017.01.001.
- [Bal85] J. J. Balmer. “Notiz über die Spectrallinien des Wasserstoffs”. In: *Wiedemann’s Annalen der Physik und Chemie* 25 (1885), pp. 80–87.

- [BE93] R. Behrisch and W. Eckstein. “Sputtering yield increase with target temperature for Ag”. In: *Nuclear Instruments and Methods in Physics Research Section B: Beam Interactions with Materials and Atoms* 82.2 (1993), pp. 255–258. ISSN: 0168-583X. DOI: [https://doi.org/10.1016/0168-583X\(93\)96027-A](https://doi.org/10.1016/0168-583X(93)96027-A). URL: <http://www.sciencedirect.com/science/article/pii/0168583X9396027A>.
- [Bea00] B. de Beauvoir, C. Schwob, O. Acef, L. Jozefowski, L. Hilico, F. Nez, L. Julien, A. Clairon, and F. Biraben. “Metrology of the hydrogen and deuterium atoms: Determination of the Rydberg constant and Lamb shifts”. In: *The European Physical Journal D - Atomic, Molecular, Optical and Plasma Physics* 12.1 (Sept. 2000), pp. 61–93. ISSN: 1434-6079. DOI: [10.1007/s100530070043](https://doi.org/10.1007/s100530070043). URL: <https://doi.org/10.1007/s100530070043>.
- [Ben09] M. S. Benilov. “The Child–Langmuir law and analytical theory of collisionless to collision-dominated sheaths”. In: *Plasma Sources Science and Technology* 18.1 (2009), p. 014005. URL: <http://stacks.iop.org/0963-0252/18/i=1/a=014005>.
- [BEV80] R. S. Bhattacharya, W. Eckstein, and H. Verbeek. “Positive charge fractions of H, D, and He backscattered from solid surfaces”. In: *Surface Science* 93.2 (1980), pp. 563–581. ISSN: 0039-6028. DOI: [https://doi.org/10.1016/0039-6028\(80\)90283-6](https://doi.org/10.1016/0039-6028(80)90283-6). URL: <http://www.sciencedirect.com/science/article/pii/0039602880902836>.
- [BGC05] T. Babkina, T. Gans, and U. Czarnetzki. “Energy analysis of hyperthermal hydrogen atoms generated through surface neutralisation of ions”. In: *Europhys. Lett.* 72.2 (2005), pp. 235–. ISSN: 0295-5075. DOI: [10.1209/epl/i2005-10220-2](https://doi.org/10.1209/epl/i2005-10220-2).
- [Ble18] Blender Online Community. *Blender - a 3D modelling and rendering package*. Blender Foundation. Blender Institute, Amsterdam, 2018. URL: <http://www.blender.org>.
- [Boh86] J. Bohdansky, H. Lindner, E. Hechtel, A.P. Martinelli, and J. Roth. “Sputtering yield of Cu and Ag at target temperatures close to the melting point”. In: *Nuclear Instruments and Methods in Physics Research Section B: Beam Interactions with Materials and Atoms* 18.1 (1986), pp. 509–514. ISSN: 0168-583X. DOI: [https://doi.org/10.1016/S0168-583X\(86\)80078-7](https://doi.org/10.1016/S0168-583X(86)80078-7). URL: <http://www.sciencedirect.com/science/article/pii/S0168583X86800787>.
- [Bra17] C. Brandt, O. Marchuk, A. Pospieszczyk, and S. Dickheuer. “Emission of fast non-Maxwellian hydrogen atoms in low-density laboratory plasma”. In: *AIP Conference Proceedings* 1811.1 (2017), p. 130001. DOI: [10.1063/1.4975736](https://doi.org/10.1063/1.4975736). eprint: <http://aip.scitation.org/doi/pdf/10.1063/1.4975736>.
- [BS77] H. A. Bethe and E. E. Salpeter. *Quantum mechanics of one- and two-electron atoms*. Plenum Publishing Corporation, New York, 1977. DOI: [10.1007/978-1-4613-4104-8](https://doi.org/10.1007/978-1-4613-4104-8).

- [CCN77] P. W. Chan, Y. W. Chan, and H. S. Ng. “Reflectivity of metals at high temperatures heated by pulsed laser”. In: *Physics Letters A* 61.3 (1977), pp. 151–153. ISSN: 0375-9601. DOI: [https://doi.org/10.1016/0375-9601\(77\)90275-4](https://doi.org/10.1016/0375-9601(77)90275-4). URL: <http://www.sciencedirect.com/science/article/pii/0375960177902754>.
- [CKK05] N. Cvetanović, M. M. Kuraica, and N. Konjević. “Excessive Balmer line broadening in a plane cathode abnormal glow discharge in hydrogen”. In: *Journal of Applied Physics* 97.3 (2005), p. 033302. DOI: 10.1063/1.1846139. eprint: <https://doi.org/10.1063/1.1846139>. URL: <https://doi.org/10.1063/1.1846139>.
- [Cly80] M. A. A. Clyne, M. C. Heaven, K. D. Bayes, and P. B. Monkhouse. “Energy transfer in collisions of excited Ar(3P_{0,2}) metastable atoms with H(2S) atoms. II. Lyman- $\hat{I}\pm$ emission profile”. In: *Chemical Physics* 47.2 (Apr. 1980), pp. 179–188. ISSN: 0301-0104. DOI: 10.1016/0301-0104(80)85005-1.
- [CM77] M. A. A. Clyne and P. B. Monkhouse. “Energy Transfer in Collision of Ar3P₀₂ metastable atoms with H₂S atoms. I. Total Rate constant and mechanism”. In: *Chemical Physics* 28 (1977), pp. 447–454. DOI: 10.1016/0301-0104(78)80023-8.
- [CN03] D. Cruz-Uribe and C. J. Neugebauer. “An Elementary Proof of Error Estimates for the Trapezoidal Rule”. In: *Mathematics Magazine* 76.4 (2003), pp. 303–306. DOI: 10.2307/3219088.
- [COK09] N. Cvetanović, B. M. Obradović, and M. M. Kuraica. “Monte Carlo simulation for excessive Balmer line broadening generated by transport of fast H Atoms in an abnormal glow discharge”. In: *Journal of Applied Physics* 105.4 (Feb. 2009), p. 043306. DOI: 10.1063/1.3079513.
- [COK11] N. Cvetanović, B. M. Obradović, and M. M. Kuraica. “Influence of cathode material on generation of energetic hydrogen atoms in a glow discharge”. In: *Journal of Applied Physics* 109.1 (2011), p. 013311. DOI: 10.1063/1.3530869. eprint: <https://doi.org/10.1063/1.3530869>. URL: <https://doi.org/10.1063/1.3530869>.
- [Coo66] J. Cooper. “Plasma spectroscopy”. In: *Reports on Progress in Physics* 29.1 (1966), p. 35. DOI: 10.1088/0034-4885/29/1/302.
- [Cow81] R. D. Cowan. *The Theory of Atomic Structure and Spectra*. University of California Press, 1981.
- [CTW89] J. T. Clarke, J. Trauger, and J. H. Waite. “Doppler shifted H Ly alpha Emission from Jupiter’s aurora”. In: *Geophysical Research Letter* 16.6 (1989), pp. 587–590. ISSN: 1944-8007. DOI: 10.1029/GL016i006p00587.
- [Del10] E. Delabie, M. Brix, C. Giroud, R. J. E. Jaspers, O. Marchuk, M. G. O’Mullane, Yu. Ralchenko, E. Surrey, M. G. von Hellermann, K. D. Zastrow, and JET-EFDA Contributors. “Consistency of atomic data for the interpretation of beam emission spectra”. In: *Plasma Physics and Controlled Fusion* 52.12 (2010), p. 125008. URL: <http://stacks.iop.org/0741-3335/52/i=12/a=125008>.

- [Dem06] W. Demtröder. *Experimentalphysik 2: Elektrizität und Optik*. Experimentalphysik / Wolfgang Demtröder. Springer Berlin Heidelberg, 2006. ISBN: 3-540-33794-6.
- [Dem10] W. Demtröder. *Experimentalphysik 3: Atome, Moleküle und Festkörper*. Experimentalphysik / Wolfgang Demtröder. Springer, 2010. ISBN: 978-3-642-03910-2.
- [Dic18a] S. Dickheuer, O. Marchuk, C. Brandt, A. Pospieszczyk, A. Gorjaev, M. Ialovega, B. Göths, Y. Krasikov, A. Krimmer, Ph. Mertens, and A. Kreter. “In situ measurements of the spectral reflectance of metallic mirrors at the H α line in a low density Ar–H plasma”. In: *Review of Scientific Instruments* 89.6 (2018), p. 063112. DOI: 10.1063/1.5024995. eprint: <https://doi.org/10.1063/1.5024995>. URL: <https://doi.org/10.1063/1.5024995>.
- [Dic18b] S. Dickheuer, O. Marchuk, S. Ertmer, A. Gorjaev, M. Ialovega, B. Göths, Y. Krasikov, Ph. Mertens, and A. Kreter. “In situ measurement of the spectral reflectance of mirror-like metallic surfaces during plasma exposition”. In: *Nuclear Materials and Energy* 17 (Dec. 2018), pp. 302–306. DOI: 10.1016/j.nme.2018.11.012.
- [Dic19a] S. Dickheuer, O. Marchuk, Y. Krasikov, Ph. Mertens, C. Brandt, S. Ertmer, P. Börner, D. Reiter, B. Göths, K. von Bovert, and A. Kreter. “Polarization by light reflection at metallic surfaces observed in the shape of the Balmer- α line of low density plasmas”. In: *Physics of Plasmas* 26.7 (July 2019), p. 073513. DOI: 10.1063/1.5088931.
- [Dic19b] S. Dickheuer, O. Marchuk, T. V. Tsankov, D. Luggenhölscher, U. Czarnetzki, W. Gromelski, S. Ertmer, and A. Kreter. “Measurement of the Magnetic Field in a Linear Magnetized Plasma by Tunable Diode Laser Absorption Spectroscopy”. In: *Atoms* 7.2 (May 2019), p. 48. DOI: 10.3390/atoms7020048.
- [DM08] D. Depla and S. Mahieu, eds. *Reactive Sputter Deposition*. Springer Berlin Heidelberg, 2008. DOI: 10.1007/978-3-540-76664-3.
- [Doe05] R.P. Doerner, M.J. Baldwin, S.I. Krashennnikov, and K. Schmid. “High temperature erosion of beryllium”. In: *Journal of Nuclear Materials* 337-339 (Mar. 2005), pp. 877–881. DOI: 10.1016/j.jnucmat.2004.09.025.
- [Doi18] K. Doi, H. Yamaoka, T. Kenmotsu, and M. Wada. “Spectroscopy Study of Hydrogen Atoms Reflected From Tungsten Surface in a Magnetized Plasma”. In: *IEEE Transactions on Plasma Science* 46.3 (Mar. 2018), pp. 482–488. ISSN: 0093-3813. DOI: 10.1109/TPS.2018.2803753.
- [Dop42] C. Doppler. “Ueber das farbige Licht der Dopplsterne und einiger anderer Gestirne des Himmels”. In: *Abhandlung der k. böhm. Gesellschaft der Wissenschaften* 2.5 (1842).
- [EB83] W. Eckstein and J. P. Biersack. “The reflection of light swift particles from heavy solid targets”. In: *Zeitschrift für Physik A Atoms and Nuclei* 310.1 (1983), pp. 1–8. ISSN: 0939-7922. DOI: 10.1007/BF01433604.

- [EB85] W. Eckstein and J. P. Biersack. “Reflection of low-energy hydrogen from solids”. In: *Applied Physics A* 38.2 (1985), pp. 123–129. ISSN: 1432-0630. DOI: 10.1007/BF00620463.
- [EB86] W. Eckstein and J. P. Biersack. “Reflection of heavy ions”. In: *Zeitschrift für Physik B Condensed Matter* 63.4 (Dec. 1986), pp. 471–478. DOI: 10.1007/bf01726195.
- [Eck02] W. Eckstein. *Calculated Sputtering, Reflection and Range Values*. Tech. rep. IPP 9/132. Max-Planck-Institut für Plasmaphysik, 2002.
- [Eck07] W. Eckstein. *Sputtering Yield*. Springer Verlag, 2007.
- [Eck09] W. Eckstein. *Reflection (Backscattering)*. Tech. rep. IPP 17/12. Max-Planck-Institut für Plasmaphysik, 2009.
- [Eck91] W. Eckstein. *Computer Simulation of Ion-Solid Interactions*. Springer Berlin Heidelberg, 1991. DOI: 10.1007/978-3-642-73513-4.
- [EMV76] W. Eckstein, F.E.P. Matschke, and H. Verbeek. “Reflection of hydrogen from stainless steel and Nb”. In: *Journal of Nuclear Materials* 63 (1976), pp. 199–204. ISSN: 0022-3115. DOI: [https://doi.org/10.1016/0022-3115\(76\)90326-3](https://doi.org/10.1016/0022-3115(76)90326-3). URL: <http://www.sciencedirect.com/science/article/pii/0022311576903263>.
- [EV79] W. Eckstein and H. Verbeek. *Data on Light Ion Reflection*. Tech. rep. IPP 9/32. Max-Planck-Institut für Plasmaphysik, 1979.
- [Fra09] G. Franz. *Low Pressure Plasmas and Microstructuring Technology*. Springer Berlin Heidelberg, 2009. DOI: 10.1007/978-3-540-85849-2.
- [Fuj99] T. Fujimoto. “Plasma polarization spectroscopy”. In: *Plasma Physics and Controlled Fusion* 41.3A (1999), A625. URL: <http://stacks.iop.org/0741-3335/41/i=3A/a=056>.
- [GM64] A. I. Golovashkin and G. P. Montulevich. “Optical and electrical properties of tin”. In: *Sov. Phys. JETP* 19.2 (1964), p. 3.
- [Gri97] H. R. Griem. *Principles of Plasma Spectroscopy*. Cambridge University Press, 1997.
- [Gus03] M. I. Guseva, V. M. Gureev, B. N. Kolbasov, S. N. Korshunov, Yu. V. Martynenko, V. B. Petrov, and B. I. Khripunov. “Subthreshold sputtering at high temperatures”. In: *Journal of Experimental and Theoretical Physics Letters* 77.7 (Apr. 2003), pp. 362–365. DOI: 10.1134/1.1581961.
- [Hag54] H. D. Hagstrum. “Theory of Auger Ejection of Electrons from Metals by Ions”. In: *Physical Review* 96 (2 Oct. 1954), pp. 336–365. DOI: 10.1103/PhysRev.96.336. URL: <https://link.aps.org/doi/10.1103/PhysRev.96.336>.
- [Hel05] M. G. von Hellermann, G. Bertschinger, W. Biel, C. Giroud, R. Jaspers, C. Jupen, O. Marchuk, M. O’Mullane, H. P. Summers, A. Whiteford, and K-D. Zastrow. “Complex Spectra in Fusion Plasmas”. In: *Physica Scripta* 2005.T120 (2005), p. 19. URL: <http://stacks.iop.org/1402-4896/2005/i=T120/a=003>.

- [Her03] Z. Herman. “Collisions of slow polyatomic ions with surfaces: The scattering method and results”. In: *Journal of the American Society for Mass Spectrometry* 14.12 (Dec. 2003), pp. 1360–1372. DOI: 10.1016/j.jasms.2003.09.002.
- [Hey96] J. D. Hey, M. Korten, Y. T. Lie, A. Pospieszczyk, D. Rusbüldt, B. Schweer, B. Unterberg, J. Wienbeck, and E. Hintz. “Doppler Broadening and Magnetic Field Effects on the Balmer Lines Emitted at the Edge of a Tokamak Plasma”. In: *Contributions to Plasma Physics* 36.5 (1996), pp. 583–604. DOI: 10.1002/ctpp.2150360505. eprint: <https://onlinelibrary.wiley.com/doi/pdf/10.1002/ctpp.2150360505>. URL: <https://onlinelibrary.wiley.com/doi/abs/10.1002/ctpp.2150360505>.
- [HQ73] G. M. Hale and M. R. Query. “Optical Constants of Water in the 200-nm to 200- μ m Wavelength Region”. In: *Applied Optics* 12.3 (Mar. 1973), p. 555. DOI: 10.1364/ao.12.000555.
- [HST73] W. Heiland, H. G. Schäffler, and E. Taglauer. “Energy distributions of low-energy noble gas ions backscattered from a single-crystal nickel surface”. In: *Surface Science* 35 (Mar. 1973), pp. 381–392. DOI: 10.1016/0039-6028(73)90227-6.
- [Hub17] M. Hubeny, B. Schweer, D. Luggenhölscher, U. Czarnetzki, and B. Unterberg. “Thomson scattering of plasma turbulence on PSI-2”. In: *Nuclear Materials and Energy* 12 (Aug. 2017), pp. 1253–1258. DOI: 10.1016/j.nme.2016.12.006.
- [Hut02] I. H. Hutchinson. *Principles of Plasma Diagnostics*. Cambridge University Press, 2002.
- [Jas08] R. J. E. Jaspers, M. G. von Hellermann, E. Delabie, W. Biel, O. Marchuk, and L. Yao. “Validation of the ITER CXRS design by tests on TEXTOR”. In: *Review of Scientific Instruments* 79.10 (2008), 10F526. DOI: 10.1063/1.2979874. eprint: <https://doi.org/10.1063/1.2979874>. URL: <https://doi.org/10.1063/1.2979874>.
- [Jas12] R. J. E. Jaspers, M. Scheffer, A. Kappatou, N. C. J. van der Valk, M. Durkut, B. Snijders, O. Marchuk, W. Biel, G. I. Pokol, G. Erdei, S. Zoletnik, and D. Dunai. “A high etendue spectrometer suitable for core charge eXchange recombination spectroscopy on ITER”. In: *Review of Scientific Instruments* 83.10 (2012), p. 10D515. DOI: 10.1063/1.4732058. eprint: <https://doi.org/10.1063/1.4732058>. URL: <https://doi.org/10.1063/1.4732058>.
- [JRS03] R. K. Janev, D. Reiter, and U. Samm. *Collision processes in low-temperature hydrogen plasmas*. Vol. 4105. Berichte des Forschungszentrums Jülich. Record converted from VDB: 12.11.2012. Jülich: Forschungszentrum, Zentralbibliothek, 2003.
- [Kau13] M. Kaufmann. *Plasmaphysik und Fusionsforschung*. Springer Spektrum, 2013.

- [KF04] H. Kastelewicz and G. Fussmann. “Plasma Modelling for the PSI Linear Plasma Device”. In: *Contrib. Plasma Phys.* 44.4 (2004), pp. 352–360. ISSN: 1521-3986. DOI: <http://dx.doi.org/10.1002/ctpp.200410053>.
- [KHV08] S. Kajita, T. Hatae, and V. S. Voitsenya. “Assessment of Laser Transmission Mirror Materials for ITER Edge Thomson Scattering Diagnostics”. In: *Plasma and Fusion Research* 3 (2008), pp. 032–032. DOI: 10.1585/pfr.3.032.
- [Kra15] Y. Krasikov, A. Panin, W. Biel, A. Krimmer, A. Litnovsky, Ph. Mertens, O. Neubauer, and M. Schrader. “Major aspects of the design of a first mirror for the ITER core CXRS diagnostics”. In: *Fusion Engineering and Design* 96-97. Supplement C (2015). Proceedings of the 28th Symposium On Fusion Technology (SOFT-28), pp. 812–816. ISSN: 0920-3796. DOI: <https://doi.org/10.1016/j.fusengdes.2015.05.031>.
- [Kra18] A. Kramida, Yu. Ralchenko, J. Reader, and NIST ASD Team. NIST Atomic Spectra Database (ver. 5.5.6), National Institute of Standards and Technology. Gaithersburg, MD, 2018. URL: <https://physics.nist.gov/asd> (visited on 08/01/2018).
- [Kre15] A. Kreter, C. Brandt, A. Huber, S. Kraus, S. Möller, M. Reinhart, B. Schweer, G. Sergienko, and B. Unterberg. “Linear Plasma Device PSI-2 For Plasma-Material Interaction Studies”. In: *Fusion Science and Technology* 68.1 (2015), pp. 8–14. DOI: 10.13182/fst14-906.
- [Kri15] A. Krimmer, E. Rosenthal, E. Andreenko, I. Orlovskiy, H. J. Allelein, Ph. Mertens, and O. Neubauer. “Testing of a SiO₂/TiO₂ mirror coating on a stainless steel substrate under ITER in-port conditions”. In: *Fusion Engineering and Design* 96-97 (2015). Proceedings of the 28th Symposium On Fusion Technology (SOFT-28), pp. 817–820. ISSN: 0920-3796. DOI: <https://doi.org/10.1016/j.fusengdes.2015.06.061>. URL: <http://www.sciencedirect.com/science/article/pii/S0920379615300934>.
- [Kri18] A. Krimmer, I. Balboa, N. J. Conway, M. De Bock, S. Friese, F. Le Guern, N. C. Hawkes, D. Kampf, Y. Krasikov, Ph. Mertens, M. Mittwollen, K. Mlynczak, J. Oellerich, G. Szarvas, B. Weinhorst, and Ch. Linsmeier. “Design Status of the ITER Core CXRS Diagnostic Setup”. In: *[shall be] submitted to Fusion Eng. Des. (Proc. 30th SOFT, 2018)* (2018).
- [Kun02] J. Kunsch. “Diodenlaser-Absorptionsspektroskopie auf dem Weg zu kommerzieller Bedeutung”. In: *Photonik* 3 (2002).
- [Kun09] Hans-Joachim Kunze. *Introduction to Plasma Spectroscopy*. Springer Berlin Heidelberg, 2009. DOI: 10.1007/978-3-642-02233-3.
- [Lan84] R. A. Langley, J. Bohdansky, W. Eckstein, P. Mioduszewski, J. Roth, E. Taglauer, E. W. Thomas, H. Verbeek, and K. L. Wilson. “Data Compendium for Plasma-Surface Interactions”. In: *Nuclear Fusion* 24.S1 (1984), S9. URL: <http://stacks.iop.org/0029-5515/24/i=S1/a=001>.

- [Lay95] N. Layadi, P. Roca i Cabarrocas, B. Drévillon, and I. Solomon. “Real-time spectroscopic ellipsometry study of the growth of amorphous and microcrystalline silicon thin films prepared by alternating silicon deposition and hydrogen plasma treatment”. In: *Physical Review B* 52 (7 Aug. 1995), pp. 5136–5143. DOI: 10.1103/PhysRevB.52.5136. URL: <https://link.aps.org/doi/10.1103/PhysRevB.52.5136>.
- [Lid05] D. R. Lide. *CRC Handbook of Chemistry and Physics, Internet Version*. Ed. by David R. Lide. CRC Press, Boca Raton, FL, 2005.
- [Lit07a] A. Litnovsky, V.S. Voitsenya, A. Costley, A.J.H. Donné, and for the SWG on First Mirrors of the ITPA Topical Group on Diagnostics. “First mirrors for diagnostic systems of ITER”. In: *Nuclear Fusion* 47.8 (2007), p. 833. URL: <http://stacks.iop.org/0029-5515/47/i=8/a=014>.
- [Lit07b] A. Litnovsky, P. Wienhold, V. Philipps, G. Sergienko, O. Schmitz, A. Kirschner, A. Kreter, S. Droste, U. Samm, Ph. Mertens, A. H. Donné, D. Rudakov, S. Allen, R. Boivin, A. McLean, P. Stangeby, W. West, C. Wong, M. Lipa, B. Schunke, G. De Temmerman, R. Pitts, A. Costley, V. Voitsenya, K. Vukolov, P. Oelhafen, M. Rubel, and A. Romanyuk. “Diagnostic mirrors for ITER: A material choice and the impact of erosion and deposition on their performance”. In: *Journal of Nuclear Materials* 363–365 (2007). Plasma-Surface Interactions-17, pp. 1395–1402. ISSN: 0022-3115. DOI: <http://dx.doi.org/10.1016/j.jnucmat.2007.01.281>.
- [LL05] M. A. Lieberman and A. J. Lichtenberg. *Principles of Plasma Discharges and Materials Processing*. 2nd ed. Wiley-Interscience, 2005.
- [LM93] B. P. Lavrov and A. S. Mel’nikov. “Observation of charge-exchange effects in Doppler profiles of Balmer lines in H₂ + Ne, Ar and Kr hollow cathode discharges”. In: *Optika i Spektroskopiya* 75.6 (1993), pp. 1152–1163.
- [LR47] W. E. Lamb and R. C. Retherford. “Fine Structure of the Hydrogen Atom by a Microwave Method”. In: *Physical Review* 72 (3 Aug. 1947), pp. 241–243. DOI: 10.1103/PhysRev.72.241. URL: <https://link.aps.org/doi/10.1103/PhysRev.72.241>.
- [LW61] N. Laegreid and G. K. Wehner. “Sputtering Yields of Metals for Ar⁺ and Ne⁺ Ions with Energies from 50 to 600 eV”. In: *Journal of Applied Physics* 32.3 (1961), pp. 365–369. DOI: 10.1063/1.1736012. eprint: <https://doi.org/10.1063/1.1736012>. URL: <https://doi.org/10.1063/1.1736012>.
- [Mar18] O. Marchuk, C. Brandt, A. Pospieszczyk, M. Reinhart, S. Brezinsek, B. Unterberg, and S. Dickheuer. “Emission of fast hydrogen atoms at a plasma–solid interface in a low density plasma containing noble gases”. In: *Journal of Physics B: Atomic, Molecular and Optical Physics* 51.2 (2018), p. 025702. URL: <http://stacks.iop.org/0953-4075/51/i=2/a=025702>.

- [Mas05] F. Massines, N. Gherardi, A. Fornelli, and S. Martin. “Atmospheric pressure plasma deposition of thin films by Townsend dielectric barrier discharge”. In: *Surface and Coatings Technology* 200.5 (2005). ICMCTF 2005, pp. 1855–1861. ISSN: 0257-8972. DOI: <https://doi.org/10.1016/j.surfcoat.2005.08.010>. URL: <http://www.sciencedirect.com/science/article/pii/S0257897205008169>.
- [McP15] K. M. McPeak, S. V. Jayanti, St. J. P. Kress, St. Meyer, St. Iotti, A. Rossinelli, and D. J. Norris. “Plasmonic Films Can Easily Be Better: Rules and Recipes”. In: *ACS Photonics* 2.3 (2015). PMID: 25950012, pp. 326–333. DOI: 10.1021/ph5004237. eprint: <https://doi.org/10.1021/ph5004237>. URL: <https://doi.org/10.1021/ph5004237>.
- [Mer01] Ph. Mertens, S. Brezinsek, P. T. Greenland, J. D. Hey, A. Pospieszczyk, D. Reiter, U. Samm, B. Schweer, G. Sergienko, and E. Vietzke. “Hydrogen release from plasma-facing components into fusion plasmas - recent results from a spectroscopic approach”. In: *Plasma Physics and Controlled Fusion* 43.12A (2001), A349. URL: <http://stacks.iop.org/0741-3335/43/i=12A/a=327>.
- [Mer15] Ph. Mertens, D. A. Castaño Bardawil, T. Baross, W. Biel, S. Friese, N. Hawkes, R. J. E. Jaspers, V. Kotov, Y. Krasikov, A. Krimmer, A. Litnovsky, O. Marchuk, O. Neubauer, G. Offermanns, A. Panin, G. Pokol, M. Schrader, and U. Samm. “Status of the R&D activities to the design of an ITER core CXRS diagnostic system”. In: *Fusion Engineering and Design* 96-97 (2015). Proceedings of the 28th Symposium On Fusion Technology (SOFT-28), pp. 129–135. ISSN: 0920-3796. DOI: <https://doi.org/10.1016/j.fusengdes.2015.05.039>. URL: <http://www.sciencedirect.com/science/article/pii/S0920379615300028>.
- [Mer19] Ph. Mertens, R. Boman, S. Dickheuer, Y. Krasikov, A. Krimmer, D. Leichtle, K. Liegeois, Ch. Linsmeier, A. Litnovsky, O. Marchuk, M. Rasinski, and M. De Bock. “On the use of rhodium mirrors for optical diagnostics in ITER”. In: *Fusion Engineering and Design* (Apr. 2019). DOI: 10.1016/j.fusengdes.2019.04.031.
- [Mey99] H. Meyer. “Analyse der Plasmarotation in einer linearen Magnetfeldkonfiguration”. PhD thesis. Humboldt-Universität zu Berlin, 1999.
- [Min17] M. Minissale, C. Pardanaud, R. Bisson, and L. Gallais. “The temperature dependence of optical properties of tungsten in the visible and near-infrared domains: an experimental and theoretical study”. In: *Journal of Physics D: Applied Physics* 50.45 (2017), p. 455601. URL: <http://stacks.iop.org/0022-3727/50/i=45/a=455601>.
- [Miy16] M. Miyamoto, M. Yamamoto, T. Akiyama, N. Yoshida, M. Tokitani, and A. Sagara. “Application of optical reflectivity measurements to diagnostics for plasma facing materials”. In: *Nuclear Materials and Energy* 9 (2016), pp. 132–136. ISSN: 2352-1791. DOI: <http://dx.doi.org/10.1016/j.nme.2016.08.012>.

- [MN87] N. J. Mason and W. R. Newell. “Total cross sections for metastable excitation in the rare gases”. In: *Journal of Physics B: Atomic and Molecular Physics* 20.6 (Mar. 1987), pp. 1357–1377. DOI: 10.1088/0022-3700/20/6/020.
- [Mos17a] L. Moser, R.P. Doerner, M.J. Baldwin, C.P. Lungu, C. Porosnicu, M. Newman, A. Widdowson, E. Alves, G. Pintsuk, J. Likonen, A. Hakola, R. Steiner, L. Marot, E. Meyer, and JET Contributors. “Investigation and plasma cleaning of first mirrors coated with relevant ITER contaminants: beryllium and tungsten”. In: *Nuclear Fusion* 57.8 (2017), p. 086019. DOI: 10.1088/1741-4326/aa73e2.
- [Mos17b] L. Moser, L. Marot, R. Steiner, R. Reichle, F. Leipold, C. Vorpahl, F. Le Guern, U. Walach, S. Alberti, I. Furno, R. Yan, J. Peng, M. Ben Yaala, and E. Meyer. “Plasma cleaning of ITER first mirrors”. In: *Physica Scripta* 2017.T170 (2017), p. 014047. URL: <http://stacks.iop.org/1402-4896/2017/i=T170/a=014047>.
- [MS79] G. M. McCracken and P. E. Stott. “Plasma-surface interactions in tokamaks”. In: *Nuclear Fusion* 19.7 (1979), p. 889. URL: <http://stacks.iop.org/0029-5515/19/i=7/a=004>.
- [New14] M. Newville, T. Stensitzki, D. B. Allen, and A. Ingargiola. “LMFIT: Non-Linear Least-Square Minimization and Curve-Fitting for Python”. In: (Sept. 2014). DOI: 10.5281/zenodo.11813.
- [Nie10] B. Niermann, M. Böke, N. Sadeghi, and J. Winter. “Space resolved density measurements of argon and helium metastable atoms in radio-frequency generated He-Ar micro-plasmas”. In: *The European Physical Journal D* 60.3 (Dec. 2010), pp. 489–495. ISSN: 1434-6079. DOI: 10.1140/epjd/e2010-00166-8. URL: <https://doi.org/10.1140/epjd/e2010-00166-8>.
- [Nie12] B. Niermann, R. Reuter, T. Kuschel, J. Benedikt, M. Böke, and J. Winter. “Argon metastable dynamics in a filamentary jet micro-discharge at atmospheric pressure”. In: *Plasma Sources Science and Technology* 21.3 (2012), p. 034002. DOI: 10.1088/0963-0252/21/3/034002.
- [Ors01] F. P. Orsitto, D. Del Bugaro, M. DiFino, A. Maiolo, M. Montecchi, E. Nichelatti, C. Gowers, and P. Nielsen. “Optical characterization of plasma facing mirrors for a Thomson scattering system of a burning plasma experiment”. In: *Review of Scientific Instruments* 72.1 (2001), pp. 540–544. DOI: 10.1063/1.1316759. eprint: <https://doi.org/10.1063/1.1316759>.
- [Pal02] C. Palmer. *Diffraction Grating Handbook*. Thermo RGL, 2002.
- [Pal98] E. D. Palik. *Handbook of optical constants of solids / [E-Book]*. englisch. San Diego: Academic Press, 1998, xvi, 804 pages : illustrations. URL: <https://ebookcentral.proquest.com/lib/fz/detail.action?docID=635397>.

- [Phe05] A. V. Phelps. “Comment on “Water bath calorimetric study of excess heat generation in resonant transfer plasmas” [J. Appl. Phys. 96, 3095 (2004)]”. In: *Journal of Applied Physics* 98.6 (2005), p. 066108. DOI: 10.1063/1.2010616. eprint: <https://doi.org/10.1063/1.2010616>. URL: <https://doi.org/10.1063/1.2010616>.
- [Phe09] A. V. Phelps. “Energetic ion, atom, and molecule reactions and excitation in low-current H₂ discharges: Model”. In: *Phys. Rev. E* 79 (6 June 2009), p. 066401. DOI: 10.1103/PhysRevE.79.066401.
- [Phe11] A. V. Phelps. “Collisional kinetics of non-uniform electric field, low-pressure, direct-current discharges in H²”. In: *Plasma Sources Science and Technology* 20.4 (2011), p. 043001. URL: <http://stacks.iop.org/0963-0252/20/i=4/a=043001>.
- [Phe90] A. V. Phelps. “Cross Sections and Swarm Coefficients for H⁺, H₂⁺, H₃⁺, H, H₂, and H⁻ in H₂ for Energies from 0.1 eV to 10 keV”. In: *Journal of Physical and Chemical Reference Data* 19.653 (1990). DOI: 10.1063/1.555858.
- [Phe92] A. V. Phelps. “Collisions of H⁺, H₂⁺, H₃⁺, ArH⁺, H⁻, H, and H₂ with Ar and of Ar⁺ and ArH⁺ with H₂ for Energies from 0.1 eV to 10 keV”. In: *J. Phys. Chem. Ref. Data* 21.4 (1992), pp. 883–897. DOI: 10.1063/1.555917.
- [Pit13] L. C. Pitchford, L. L. Alves, K. Bartschat, S. F. Biagi, M. C. Bordage, A. V. Phelps, C. M. Ferreira, G. J. M. Hagelaar, W. L. Morgan, S. Pancheshnyi, V. Puech, A. Stauffer, and O. Zatsarinny. “Comparisons of sets of electron–neutral scattering cross sections and swarm parameters in noble gases: I. Argon”. In: *Journal of Physics D: Applied Physics* 46.33 (Aug. 2013), p. 334001. DOI: 10.1088/0022-3727/46/33/334001.
- [Que85] M. R. Querry. *Optical Constants of Minerals and Other Materials from the Millimeter to the Ultraviolet*. Tech. rep. CRDC-CR-85034. University of Missouri, 1985.
- [Rak98] A. D. Rakić, A. B. Djurišić, J. M. Elazar, and M. L. Majewski. “Optical properties of metallic films for vertical-cavity optoelectronic devices”. In: *Applied Optics* 37.22 (Aug. 1998), pp. 5271–5283. DOI: 10.1364/AO.37.005271. URL: <http://ao.osa.org/abstract.cfm?URI=ao-37-22-5271>.
- [Rei15] M. Reinhart, A. Kreter, L. Buzi, M. Rasinski, A. Pospieszczyk, B. Unterberg, and Ch. Linsmeier. “Influence of plasma impurities on the deuterium retention in tungsten exposed in the linear plasma generator PSI-2”. In: *Journal of Nuclear Materials* 463 (Aug. 2015), pp. 1021–1024. DOI: 10.1016/j.jnucmat.2014.11.045.
- [Rei17] R. Reimer, O. Marchuk, B. Geiger, P. J. Mc Carthy, M. Dunne, J. Hobirk, and R. Wolf. “Influence of non-local thermodynamic equilibrium and Zeeman effects on magnetic equilibrium reconstruction using spectral motional Stark effect diagnostic”. In: *Review of Scientific Instruments* 88.8 (2017), p. 083509. DOI: 10.1063/1.4994889. eprint: <https://doi.org/10.1063/1.4994889>. URL: <https://doi.org/10.1063/1.4994889>.

- [Sad04] N. Sadeghi. “Practical Aspects of Molecular Spectroscopy in Plasmas 6. Molecular Spectroscopy Techniques Applied for Processing Plasma Diagnostics”. In: *Journal of Plasma and Fusion Research* 80.9 (2004), pp. 767–776. DOI: 10.1585/jspf.80.767.
- [Sam87] U. Samm, H. L. Bay, P. Bogen, H. Hartwig, E. Hintz, K. Höthker, Y. T. Lie, A. Pospieszczyk, G. G. Ross, D. Rusbüldt, and B. Schweer. “Plasma edge research on TEXTOR”. In: *Plasma Phys. Control. Fusion* 29.10A (1987), pp. 1321–. ISSN: 0741-3335. DOI: 10.1088/0741-3335/29/10a/313.
- [Sam89] U. Samm, P. Bogen, H. Hartwig, E. Hintz, K. Höthker, Y. T. Lie, A. Pospieszczyk, D. Rusbüldt, B. Schweer, and Y. J. Yu. “Plasma edge physics in the textor tokamak with poloidal and toroidal limiters”. In: *Journal of Nuclear Materials* 162-164 (Apr. 1989), pp. 24–37. DOI: 10.1016/0022-3115(89)90255-9.
- [Sig69] P. Sigmund. “Theory of Sputtering. I. Sputtering Yield of Amorphous and Polycrystalline Targets”. In: *Physical Review* 184 (2 Aug. 1969), pp. 383–416. DOI: 10.1103/PhysRev.184.383. URL: <https://link.aps.org/doi/10.1103/PhysRev.184.383>.
- [ŠMK05] N. M. Šišović, G. Lj. Majstorović, and N. Konjević. “Excessive hydrogen and deuterium Balmer lines broadening in a hollow cathode glow discharges”. In: *Eur. Phys. J. D* 32.3 (2005), pp. 347–354. ISSN: 1434-6060. DOI: <http://dx.doi.org/10.1140/epjd/e2004-00192-1>.
- [ŠMK07] N.M. Šišović, G. Lj. Majstorović, and N. Konjević. “Excessive Doppler broadening of the H α line in a hollow cathode glow discharge”. In: *Eur. Phys. J. D* 41.1 (2007), pp. 143–150. ISSN: 1434-6060. DOI: <http://dx.doi.org/10.1140/epjd/e2006-00187-x>.
- [Sta00] P. C. Stangeby. *The Plasma Boundary of Magnetic Fusion Devices*. Institute of Physics Publishing (London), 2000.
- [Sys11] Stanford Research Systems. *Model SR830 DSP Lock-in Amplifier Manual*. 2011. URL: <https://www.thinksrs.com/downloads/pdfs/manuals/SR830m.pdf>.
- [Tho68] M. W. Thompson. “II. The energy spectrum of ejected atoms during the high energy sputtering of gold”. In: *The Philosophical Magazine: A Journal of Theoretical Experimental and Applied Physics* 18.152 (1968), pp. 377–414. DOI: 10.1080/14786436808227358. eprint: <https://doi.org/10.1080/14786436808227358>. URL: <https://doi.org/10.1080/14786436808227358>.
- [TI06] H. Tompkins and E. A. Irene. *Handbook of Ellipsometry*. WILLIAM ANDREW INC, Jan. 11, 2006. 886 pp. ISBN: 0815514999. URL: https://www.ebook.de/de/product/3449847/harland_tompkins_eugene_a_irene_handbook_of_ellipsometry.html.
- [Tok94] M. Z. Tokar. “Modelling of detachment in a limiter tokamak as a nonlinear phenomenon caused by impurity radiation”. In: *Plasma Physics and Controlled Fusion* 36.11 (Nov. 1994), pp. 1819–1843. DOI: 10.1088/0741-3335/36/11/009.

- [Uji72] K. Ujihara. “Reflectivity of Metals at High Temperatures”. In: *Journal of Applied Physics* 43.5 (1972), pp. 2376–2383. DOI: 10.1063/1.1661506.
- [Van80] B. Van Zyl, H. Neumann, H. L. Rothwell, and R. C. Amme. “Balmer- α and Balmer- β emission cross sections for H+Ar collisions”. In: *Physical Review A* 21.3 (May 1980), pp. 716–729. DOI: 10.1103/physreva.21.716.
- [VEB80] H. Verbeek, W. Eckstein, and R. S. Bhattacharya. “Angular and energy distributions of H and He atoms backscattered from gold”. In: *Journal of Applied Physics* 51.3 (Mar. 1980), pp. 1783–1789. DOI: 10.1063/1.327740.
- [Ver75] H. Verbeek. “Total backscattering yields of 3–15-keV protons from polycrystalline Nb”. In: *Journal of Applied Physics* 46.7 (July 1975), pp. 2981–2985. DOI: 10.1063/1.322038.
- [VG80] R. L. Vance and G. A. Gallup. “Theoretical potential curves for excited states of ArH and the rate of collisional quenching of metastable Ar by H”. In: *J. Chem. Phys.* 73.2 (1980), pp. 894–901. DOI: 10.1063/1.440757.
- [VGN83] B. Van Zyl, M. W. Gealy, and H. Neumann. “Balmer- α and Balmer- β emission cross sections for low-energy H collisions with He and H₂”. In: *Physical Review A* 28.1 (July 1983), pp. 176–180. DOI: 10.1103/PhysRevA.28.176.
- [VGN85] B. Van Zyl, M. W. Gealy, and H. Neumann. “Excitation of low-energy H atoms in H+Ne collisions”. In: *Physical Review A* 31.5 (May 1985), pp. 2922–2931. DOI: 10.1103/physreva.31.2922.
- [VKK96] I.R. Videnović, N. Konjević, and M.M. Kuraica. “Spectroscopic investigations of a cathode fall region of the Grimm-type glow discharge”. In: *Spectrochimica Acta Part B: Atomic Spectroscopy* 51.13 (1996), pp. 1707–1731. ISSN: 0584-8547. DOI: [https://doi.org/10.1016/S0584-8547\(96\)01533-9](https://doi.org/10.1016/S0584-8547(96)01533-9). URL: <http://www.sciencedirect.com/science/article/pii/S0584854796015339>.
- [VNG86] B. Van Zyl, H. Neumann, and M. W. Gealy. “Balmer-line emission from low-energy H impact on Kr and Xe”. In: *Physical Review A* 33.3 (May 1986), pp. 2093–2095. DOI: 10.1103/physreva.33.2093.
- [Wei94] M. Weitz, A. Huber, F. Schmidt-Kaler, D. Leibfried, and T. W. Hänsch. “Precision measurement of the hydrogen and deuterium 1 S ground state Lamb shift”. In: *Physical Review Letters* 72 (3 Jan. 1994), pp. 328–331. DOI: 10.1103/PhysRevLett.72.328. URL: <https://link.aps.org/doi/10.1103/PhysRevLett.72.328>.
- [WGA09] W. S. M. Werner, K. Glantschnig, and C. Ambrosch-Draxl. “Optical Constants and Inelastic Electron-Scattering Data for 17 Elemental Metals”. In: *Journal of Physical and Chemical Reference Data* 38.4 (2009), pp. 1013–1092. DOI: 10.1063/1.3243762. eprint: <http://dx.doi.org/10.1063/1.3243762>.

- [Wil11] W. Williams, Z.-T. Lu, K. Rudinger, C.-Y. Xu, R. Yokochi, and P. Mueller. “Spectroscopic study of the cycling transition $4s[3/2]2-4p[5/2]3at$ 811.8 nm in Ar39: Hyperfine structure and isotope shift”. In: *Physical Review A* 83.1 (Jan. 2011). DOI: 10.1103/physreva.83.012512.
- [WMF07] O. Waldmann, H. Meyer, and G. Fussmann. “Anomalous Diffusion in a Linear Plasma Generator”. In: *Contributions to Plasma Physics* 47.10 (2007), pp. 691–702. ISSN: 1521-3986. DOI: 10.1002/ctpp.200710079.
- [WOL77] J. H. Weaver, C. G. Olson, and D. W. Lynch. “Optical investigation of the electronic structure of bulk Rh and Ir”. In: *Phys. Rev. B* 15 (8 Apr. 1977), pp. 4115–4118. DOI: 10.1103/PhysRevB.15.4115. URL: <https://link.aps.org/doi/10.1103/PhysRevB.15.4115>.
- [Xia91] Y. Xia, X. Xu, C. Tan, L. Mei, H. Yang, and X. Sun. “Reflection of light ion from solid surfaces studied by Monte Carlo simulation and transport theory”. In: *Journal of Applied Physics* 69.1 (1991), pp. 439–446. DOI: 10.1063/1.347681. eprint: <https://doi.org/10.1063/1.347681>. URL: <https://doi.org/10.1063/1.347681>.
- [Zee97a] P. Zeeman. “The Effect of Magnetisation on the Nature of Light Emitted by a Substance”. In: *Nature* 55 (Feb. 1897), p. 347. URL: <http://dx.doi.org/10.1038/055347a0>.
- [Zee97b] P. Zeeman. “XXXII. On the influence of magnetism on the nature of the light emitted by a substance”. In: *The London, Edinburgh, and Dublin Philosophical Magazine and Journal of Science* 43.262 (1897), pp. 226–239. DOI: 10.1080/14786449708620985. eprint: <https://doi.org/10.1080/14786449708620985>. URL: <https://doi.org/10.1080/14786449708620985>.
- [Zee97c] P. Zeeman. “XXXIII. Doublets and triplets in the spectrum produced by external magnetic forces.—(II.)” In: *The London, Edinburgh, and Dublin Philosophical Magazine and Journal of Science* 44.268 (1897), pp. 255–259. DOI: 10.1080/14786449708621060. eprint: <https://doi.org/10.1080/14786449708621060>. URL: <https://doi.org/10.1080/14786449708621060>.
- [Zhu16] X. M. Zhu, Z. W. Cheng, E. Carbone, Y. K. Pu, and U. Czarnetzki. “Determination of state-to-state electron-impact rate coefficients between Ar excited states: a review of combined diagnostic experiments in afterglow plasmas”. In: *Plasma Sources Science and Technology* 25.4 (July 2016), p. 043003. DOI: 10.1088/0963-0252/25/4/043003.
- [ZWB14] O. Zatsarinny, Y. Wang, and K. Bartschat. “Electron-impact excitation of argon at intermediate energies”. In: *Physical Review A* 89.2 (Feb. 2014). DOI: 10.1103/physreva.89.022706.

LIST OF PUBLICATIONS

Reviewed Publications

1. C. Brandt, O. Marchuk, A. Pospieszczyk and **S. Dickheuer**, AIP Conference Proceedings 1811, 130001 (2017) Reference [Bra17]
2. O. Marchuk , C. Brandt, A. Pospieszczyk, M. Reinhart, S. Brezinsek ,B. Unterberg and **S. Dickheuer**, J. Phys. B: At. Mol. Opt. Phys. 51 (2018) Reference [Mar18]
3. **S. Dickheuer** *et al*, Review of Scientific Instruments Reference 89, 063112 (2018) [Dic18a]
4. **S. Dickheuer** *et al*, Nuclear Materials and Energy 17, 302-306 (2018) [Dic18b]
5. Ph. Mertens, **S. Dickheuer**, Y. Krasikov, A. Krimmer, A. Litnovsky, Ch. Linsmeier, O. Marchuk, M. De Bock, F. Le Guern , Submitted to Fusion Engineering and Design, [Mer19]
6. **S. Dickheuer** *et al*, Physics of Plasmas 26, 073513 (2019) [Dic19a]
7. **S. Dickheuer** *et al*, Atoms 7, 48 (2019) [Dic19b]

Conferences

1. **S. Dickheuer**, O. Marchuk, C. Brandt and A. Pospieszczyk, 2016 DPG-Verhandlung P 11.2, Hannover, Germany
2. **S. Dickheuer**, O. Marchuk, C. Brandt and A. Pospieszczyk, 2016 69th Annual Gaseous Electronics Conference QR2.005, Bochum, Germany
3. **S. Dickheuer**, O. Marchuk, C. Brandt and A. Pospieszczyk, 2017 DPG-Verhandlung P 24.3, Bremen, Germany
4. O. Marchuk, **S. Dickheuer**, C. Brandt and A. Gorjaev and M. Ialovega, 2017 44th EPS Conference on Plasma Physics O2.304, Belfast, Ireland

5. **S. Dickheuer**, O. Marchuk, C. Brandt, A. Goriaev, M. Ialovega, and PSI-2 Team , 2018 DPG-Verhandlung P 2.7, Erlangen, Germany
6. **S. Dickheuer**, C. Brandt, A. Pospieszczyk, A. Goriaev, M. Ialovega, 23rd International Conference on Plasma Surface Interactions in Controlled Fusion Devices (PSI-23), Poster 223, Princeton, USA
7. Ph. Mertens, **S. Dickheuer**, Y. Krasikov, A. Krimmer, A. Litnovsky, Ch. Linsmeier, O. Marchuk, M. De Bock, F. Le Guern, 30th edition of the Symposium on Fusion Technology (SOFT-2018), P2.056, Giardini Naxos, Italy

ACKNOWLEDGEMENT

I would like to warmly thank all the people from the IEK-4 institute and from the Ruhr University Bochum who helped in a variety of ways to make this thesis possible. I had a great time at the institute working with so many friendly and motivated people. I had a lot of fun working at the PSI-2 and learned a lot about spectroscopy and plasma physics.

First of all, I would like to thank PD Dr. Oleksandr Marchuk for giving me the opportunity to make my PhD thesis in his research group under his supervision. I enjoyed our discussions about our research and physics in general. I really learned a lot and got a deep insight in atomic spectroscopy and plasma-surface interaction during these three years. You were a great supervisor and I could contact you every time I had questions and this really helped to successfully finish this thesis.

I'm also grateful to Prof. Dr. Uwe Czarnetzki to be the second advisor of my thesis and for the help and discussions about the TDLAS system.

I'm not less grateful to Prof. Dr. Christian Linsmeier for giving me the opportunity to write my thesis in his institute and for the helpful discussions about my topic during our meetings.

I would like to thank Christian Brandt for helping me at the start of my thesis with the PSI-2 device and for answering all the questions I had about the theory of fast atoms and Langmuir probes. Furthermore, I would like to thank Dr. Dirk Luggenhölscher and Dr. Tsanko Tsankov for the construction of the TDLAS system and for the fruitful discussions about absorption spectroscopy and plasma physics in general.

My thanks also go to my two master students Andrey Goriav and Mykola Ialovega and my trainee Wojciech Gromelski for the help and the great time we had together. I would also like to thank Dr. Mikhail Tokar for the great discussion and explanation about the estimation of the metastable density in the PSI-2 plasma.

I'm thankful for the PSI-2 team, especially Michael Vogel, Sebastian Kraus, Fabian Stoffels and Dr. Arkadi Kreter for keeping the PSI-2 running and helping whenever needed during the experimental campaigns.

Furthermore, I thank Dr. Philippe Mertens for the fruitful discussions about mirrors and polarization measurements in the plasma.

I thank all the other PhD students, especially Jörg Cosfeld, Stephan Ertmer, Jannis Oelmann, Michael Hubeny, Simon Heuer, Felix Klein, Janina Schmitz and Rahul Rayaprolu for the great time working together. The work was much easier having

you around.

Last but not least, I would like to thank my family and above all Farah and my daughter Mina for all the love and endless support during this time.

Band / Volume 475

Reversible wasserstoffbetriebene Festoxidzellensysteme

M. H. Frank (2019), 187 pp

ISBN: 978-3-95806-430-0

Band / Volume 476

**Partitioning of carbon dioxide exchange
in rapidly and slowly changing ecosystems**

P. Ney (2019), xvi, 95 pp

ISBN: 978-3-95806-431-7

Band / Volume 477

Massentransportphänomene in Schichtsystemen eines Elektrolyseurs

U. Panchenko (2019), 107 pp

ISBN: 978-3-95806-433-1

Band / Volume 478

**Mechanische Eigenschaften von Polymer-Elektrolyt-Membran-
Brennstoffzellen**

P. Irmischer (2019), vii, 177 pp

ISBN: 978-3-95806-435-5

Band / Volume 479

**Morphology and Degradation of High Temperature
Polymer Electrolyte Fuel Cell Electrodes**

S. Liu (2019), III, 162 pp

ISBN: 978-3-95806-436-2

Band / Volume 480

**Structural uptake and retention of safety relevant radionuclides by
cementitious materials**

S. Lange (2019), 133 pp

ISBN: 978-3-95806-437-9

Band / Volume 481

**Quantifying the Impact of Inhomogeneity, Transport and
Recombination in Emerging Thin-Film Solar Cells**

P. Kaienburg (2019), vii, 258 pp

ISBN: 978-3-95806-440-9

Band / Volume 482

**Studies of oxidation resistant tungsten alloys
at temperatures of 1100K to 1475K**

F. Klein (2019), 158 pp

ISBN: 978-3-95806-444-7

Band / Volume 483

Impact Assessment of Land-Use Change and Agricultural Treatments on Greenhouse Gas Emissions from Wetlands of Uganda and Tanzania

K. X. X. Wagner (2019), 144 pp

ISBN: 978-3-95806-447-8

Band / Volume 484

IEK-3 Report 2019

Tailor-Made Energy Conversion for Sustainable Fuels

D. Stolten, B. Emonts (Eds.) (2020), 162 pp

ISBN: 978-3-95806-451-5

Band / Volume 485

Multiskalare Modellierung integrierter Energie- und Elektrizitätssysteme

T. C. Pesch (2019), XXV, 384 pp

ISBN: 978-3-95806-452-2

Band / Volume 486

Quantitative Untersuchung des Laserablationsprozesses mittels Kombination von optischer Spektroskopie und Massenspektrometrie

J. Oelmann (2020), vii, 141 pp

ISBN: 978-3-95806-453-9

Band / Volume 487

Leistungssteigerung metallgestützter Festelektrolyt-Brennstoffzellen (MSCs) durch gezielte Optimierungen des Anoden/Elektrolytverbunds

C. Bischof (2020), X, 176 pp

ISBN: 978-3-95806-455-3

Band / Volume 488

Aluminiumoxiddispersionsverstärkte Haftvermittlermaterialien in Wärmedämmschichtsystemen

C. Vorkötter (2020), VIII, 99, XXXIII pp

ISBN: 978-3-95806-457-7

Band / Volume 489

The Balmer lines emission of fast hydrogen atoms at the plasma-solid interface in a low density plasma: challenges and applications

S. O. Dickheuer (2020), 117 pp

ISBN: 978-3-95806-458-4

Energie & Umwelt / Energy & Environment
Band / Volume 489
ISBN 978-3-95806-458-4